

https://dspace.org/

The sound of ink

Carlson, Craig Stuart

2021
https://hdl.handle.net/10539/31881

Downloaded from a DSpace repository. https://dspace.org/

The Sound of Ink

Craig Stuart Carlson

A thesis submitted to the Faculty of Engineering and the Built Environment, University of the Witwatersrand, Johannesburg, in fulfilment of the requirements for the degree of Doctor of Philosophy.

Johannesburg, 2021

Declaration

I declare that this thesis is my own, unaided work, except where otherwise acknowledged. It is being submitted for the degree of Doctor of Philosophy to the University of the Witwatersrand, Johannesburg. It has not been submitted before for any degree or examination to any other university.

Signed this 2nd day of June 2021



Craig Stuart Carlson

Preface

Dear reader,

It is with great pleasure that I share this body of work with you. What follows is the culmination of my research performed during my time as a registered PhD student at the University of the Witwatersrand, Johannesburg, South Africa.

I have a vested interest in tattoos, with the photos of tattoos shown in this thesis being from my personal collection of body art. This made my research into tattoos and ultrasound all the more fascinating. Sometimes it is challenging to find that field where your interests and research direction overlap so significantly – so I count myself particularly fortunate!

This thesis is borne out of many experiments; analysis; writing; more experiments; more analysis; and rewriting. And many many milkshakes with my trusted supervisor, Professor Michiel Postema. There were times in the development of this research where the best ideas and ways forward came from these sugar-fuelled discussions!

It is important to note that a bulk of the work presented has been previously presented at conferences and/or published in a variety of journals. The relevant references have been included at the start of the relevant chapters.

Without further ado, I trust you will enjoy consuming the presented work as much as I did while putting it together.

Craig S. Carlson

Abstract

Despite tattooing and tattoos having been around for thousands of years, scientific research on the topic is surprisingly limited. The role that ultrasound might play in the understanding of tattoos and tattoo inks is the topic of this thesis. This is of interest since ultrasound interacts with hydrophobic particles and therefore must interact with tattoo ink. This research is important because people want to detect, modify and remove tattoos. In this theoretical and experimental research, the size distribution, speed of sound, attenuation, and nucleation threshold of black tattoo ink was determined. Additionally, the effect that black tattoo ink has on tissues and brightness-mode ultrasound images was described. Finally potential sharpening effects of ultrasound on skin-cutting devices were demonstrated using a fixed blade as a representative device.

In the research presented it was found that black tattoo ink has a mode particle diameter of 0.29 μm and the largest particle diameter of 1.14 μm. The associated resonance frequency of the largest particles was 15 MHz, with the smaller particles even higher. The speed of sound and attenuation coefficient were determined to be 1639 $\mathrm{m\,s^{-1}}$ and 0.15±0.01 $\mathrm{dB\,cm^{-1}\,MHz^{-1}}$, respectively. The theoretical nucleation threshold was calculated to be 1.3× the resting radius and confirmed to be lower than the Blake cavitation threshold of 2× the resting radius. The change of the speed of sound and the attenuation coefficient was negligible due to *in situ* black tattoo ink. Critical refraction highlighting was introduced to describe the artefacts observed on brightness-mode ultrasound images. The sharpening effect of ultrasound on a fixed blade cutting device was demonstrated.

While the objectives were met and a greater understanding of tattoos and tattoo inks was demonstrated, the implications of the results show that ultrasound, together with the methods introduced in this work, would be better used to determine some of the acoustic properties of other materials.

Acknowledgements

This research was performed under the auspices of the Biomedical Engineering Research Group at the University of the Witwatersrand, Johannesburg.

The work presented in this thesis has been based on research supported in part by the National Research Foundation of South Africa, Grant Number 127102. Laser scanning confocal microscopy was performed at the Life Sciences Imaging Facility of the University of the Witwatersrand, Johannesburg. The sonography equipment used in this research was kindly supplied by High Tech Medical, Randburg, South Africa. High-speed photography was performed at the University of Hokkaido and was supported in part by JSPS KAKENHI, Grant Numbers JP17H00864 and JP20H04542. Ethical clearance was obtained from the Human Research Ethics Committee (Medical) of the University of the Witwatersrand, Johannesburg, under Clearance Certificate No. M190808 MED19-08-006.

With the formalities out of the way, there are many people who have helped me reach this point that I need to acknowledge and thank.

First and foremost, to Professor Michiel Postema – Your constant support and guidance through my PhD journey has allowed me to become the researcher I am today. It has been an honour to have you as my supervisor and I sincerely hope we have many more opportunities to collaborate in the future.

To my co-authors – Without you and your valuable contributions, the path I walked would have been a lot longer and a lot lonelier.

To my friends and colleagues in the School of Electrical and Information Engineering – You voluntarily discussed my challenges over coffee, allowing me to discover the next way forward. I won't question why you entertained my randomness, but I thank you.

To Professor Cheng; Professor Hofsajer; Professor Aharonson; and Doctor Hunt – You ensured that I was on the right track when defending my research proposal. It is not a task taken lightly, and your time and effort is much appreciated.

To Mr Riaan Visagie – It was by chance that we met, but your interest in my work and the time that you voluntarily donated to bring the sonography equipment to me, and allow me to scan your tattoos multiple times helped guide the direction my work.

To Mrs Dee Rudram-Ellis, the artists and staff at Steamed Rabbit Tattoos – Thank you for putting up with my pestering and arbitrary questioning during my research. Your patience, kindness and passion for the art helped me to develop my understanding of the field. And your skills ensured I was able to continue my "ink therapy" during the course of my work!

To Ms Caitlin Sanders – You may have only (officially) come into my life while I was pulling my first draft together, but I am truly thankful to you for all you have done. Without your unwavering support I am certain I would still be fluffing around trying to finalise that first draft.

To my family – You have put up with my periods of absences when the work beckoned and still welcome me with open arms. I am eternally grateful for your understanding and I will never forget the love you have shown me through this journey.

Last but certainly not least, to my internal and external examiners – You have given of your valuable time to critique my work. While your involvement only began when there was a "finished" product, your input has been the most valuable of all. For this I wish to extend a special vote of thanks.

Contents

Declaration i

Preface ii

Abstract iii

Acknowledgements iv

Contents vi

List of Figures ix

List of Tables xiv

List of Symbols and Abbreviations xv

1 Introduction 1

1.1 What is a tattoo? 1

1.2 What are tattoo inks? 2

1.3 How are tattoos created? 3

1.4 How are tattoos removed? 4

1.5 Dynamics of ultrasound 6

1.6 Research question 6

1.7 Research objectives 7

1.8 Rationale 7

1.9 Outline 9

2 Ink Attenuation of Ultrasound 11

2.1 Introduction 12

2.2 Theory 14

2.3 Materials and methods 15

2.4 Results and discussion 18

2.5 Conclusions 23

3 Transient Ink Nucleation 25

3.1 Introduction 25

3.2 Materials and methods 26

3.3 Results and discussion 28

3.4 Conclusions 29

4 Nucleation Threshold of Ink 30

4.1 Introduction 31

4.2 Theory 32

4.3 Materials and methods 33

4.4 Results and discussion 35

4.5 Conclusions 37

5 Acoustic Analysis of Inked Tissues **39**

5.1 Introduction 40

5.2 Theory 41

5.3 Materials and methods 47

5.4 Results and discussion 51

5.5 Conclusions 56

6 Sharp Sonic Cutting **57**

6.1 Introduction 57

6.2 Materials and methods 58

6.3 Results and discussion 61

6.4 Conclusions 64

7 Discussion **65**

References **68**

A Supplementary Material **83**

A.1 Transient ink nucleation 83

A.2 Acoustic analysis of inked tissues 84

About the Author **91**

List of Figures

1.1 Example of a tattoo on a calf (left) and graphical representation of a tattoo in the skin (right). The epidermis layer (0.1–1.5 mm thickness) (a), *in situ* tattoo ink layer (b), dermis layer (1.5–4.0 mm thickness) (c), and the start of the subcutaneous tissue layer (d) are shown to indicate the relative position of the tattoo in the skin. . . . 2

2.1 Size distribution of Zuper Black pigment dispersion (histogram) and particle resonance frequency as a function of the diameter (curve), with an inlay of a bright-field microscopy image of a 0.01% dilution of Zuper Black at 63× magnification. 16

2.2 Line drawing of the experimental setup, consisting of a burette clamp and stand (a), water, whose level is indicated by a blue dashed line (b), a £1 coin for scale (c), a tissue-mimicking phantom receptacle (d), an ultrasound probe (e), and a Perspex container (f). 17

2.3 Top view of the tissue-mimicking phantom receptacle with two cylindrical wells. Dimensions are in mm. 17

2.4 Brightness-mode scans at a 13-MHz ultrasound frequency of a phantom receptacle well filled with black ink (a–d), phantom material (e), and distilled water (f); and corresponding axial backscattering profiles [8-bit grey scale] as a function of perceived distance [cm]. Time stamps are relative to (a). The green dot corresponds to the right-hand side of the probe. 19

2.5 Brightness-mode scans at a 5-MHz ultrasound frequency of a phantom receptacle well filled with black ink (a–d), phantom material (e), and saline (f); and corresponding axial backscattering profiles [8-bit grey scale] as a function of perceived distance [cm]. Time stamps are relative to (a). The green dot corresponds to the right-hand side of the probe. 22

2.6 Brightness-mode scans of capillaries filled with black ink (a), degassed water (b), and air (c); and their respective axial backscattering profiles on an 8-bit grey scale. The green dot corresponds to the right-hand side of the probe. 23

3.1 Top view of the tissue-mimicking phantom with three cylindrical wells. The probe is visible on the South face. A £1 coin is included for scale. Dimensions have been stated in mm. 27

3.2 Phantom wells filled with black ink (left) and saline (right), directly after filling (a) and 9 minutes later (b). The green dot corresponds to the left-hand side of the probe. Each tick corresponds to 1.1 cm. . . 28

3.3 Zuper Black ink particles before (a), during (b), and after (c) sonication. Each frame corresponds to a $36\times36\,(\mu\mathrm{m})^2$ area. Time stamps, in nanoseconds, are in the lower right corners. 29

4.1 Quasi-isostatic liquid pressure change Δp as a function of $\left(R\,R_0^{-1}\right)$, computed for the mode particle diameter (—) and the largest particle diameter (—) of carbon black pigment dispersion. A red dashed line is drawn through the minima, for which $R_\theta\,R_0^{-1}=1.3$ holds (– –). . 35

4.2 Curves of the radii R of three nucleating Zuper Black dispersion particles normalised by their respective resting radii R_0 as a function of time t normalised by period T, during a 20-cycle burst with a 2-V amplitude, with 36-μm-diameter inlays of high-speed video footage. Particles 1–3 are represented by bold (—), thin (—), and dashed (– –) lines, respectively. Particle 3 is not shown in the inlays. The stationary situation $R_{\max}R_0^{-1}=1$ is indicated by a blue dotted line (···). 36

4.3 Histogram of maximum Zuper Black expansion normalised by particle resting radii. White bins represent particles that underwent explosive growth, black bins represent particles that did not undergo explosive growth. 37

5.1 Dorsal tattoo comprising carbon black and titanium white pigments (a); the areas of the two rectangular half-inked regions of interest have been marked in white. Brightness-mode image of the region of interest on the left shoulder (b); the separation between inked and uninked skin is indicated by a yellow line and a zone of increased scattering amplitudes is indicated by an opaque blue trapezoid (c). Brightness-mode image of the region of interest on the lower back (d); the separation between inked and uninked skin is indicated by a yellow line and a zone of increased scattering amplitudes is indicated by an opaque blue trapezoid (e). Frames b–e have been horizontally flipped such that the left-hand-side of the scan corresponds to the inked left-hand-side of the region of interest. The probe was held by the same sonographer during scanning. 42

5.2 Graphical representation of the parameters in equation (5.1). The physical situation (a) results in an axial trace recording (b). 44

5.3 Graphical representation of the parameters in equation (5.5). The physical situations (a, c) result in axial trace recordings (b, d). . . . 45

5.4 Graphical representation of the parameters in equations (5.6) and (5.7). The physical situation (a) results in axial trace recordings (b). 46

5.5 Experimental setup of the probe sonicating tattooed pork embedded in a tissue-mimicking phantom. According to practice [140], a St Helena £1 coin with a diameter of 23.44-mm and thickness of 2.80-mm, has been added for scale and for three-dimensional perspective. The dimensions of the phantom were $112\times79\times40\,\mathrm{mm}^3$. 49

5.6 Brightness-mode scans of artificial skin, unaltered (a) and altered by tattooing (b), positioned proximal to phantom material and their respective axial greyscale profiles (c). 52

5.7 Unmarked (a,c,e,g) and marked (b,d,f,h) brightness-mode scans of pork belly (PB) adjacent to phantom material (PH). The separation between pork and phantom material is indicated by a yellow line and zones of increased scattering amplitudes by opaque blue lines. . . . 54

5.8 Unmarked (a,c,e,g) and marked (b,d,f,h) brightness-mode scans of inked pork belly (IN) and unaltered pork belly (UA). The separation between inked and uninked skin is indicated by a yellow line and zones of increased scattering amplitudes by opaque blue lines. 55

6.1 A schematic (a) and photograph (b) of the experimental set-up. . . . 59

6.2 Ultrasonic cutting device with a single element ultrasound transducer and a scalpel blade attached with screws to a 55-mm Perspex rod. . 60

6.3 Position of the temperature probes on the ultrasonic knife on the blade (T1) and over the ultrasound transducer (T2). 60

6.4 A6-sized experimental sheet with marks indicating the industrially cut edge (E1-E8) and along the incisions (F1-F8). 61

6.5 Temperature difference over a 15 minute period with the ultrasonic knife under sonication. The red dots indicate the temperature difference at the blade (T1) and blue diamonds indicate the temperature difference over the ultrasound transducer (T2). 62

6.6 Back-lit bright-field 10× microscopy images of incisions in paper from an unsonicated blunt blade (a) and a sonicated blunt blade (b), compared to the paper edge from sharp industrial cutting (c). The darks areas represent the paper. Each frame corresponds to a 416 × 416 (μm^2) area. 63

A.1 Zuper Black ink particles during cycles 1 – 5 of sonication (left to right), where each cycle comprises 10 frames (top to bottom). Each frame corresponds to a 36×36 (μm)^2 area. Time stamps, in nanoseconds, are in the lower right corners. 85

A.2 Zuper Black ink particles during cycles 6 – 10 of sonication (left to right), where each cycle comprises 10 frames (top to bottom). Each frame corresponds to a 36×36 (μm)^2 area. Time stamps, in nanoseconds, are in the lower right corners. 86

A.3 Zuper Black ink particles during cycles 11 – 15 of sonication (left to right), where each cycle comprises 10 frames (top to bottom). Each frame corresponds to a $36 \times 36\,(\mu\mathrm{m})^2$ area. Time stamps, in nanoseconds, are in the lower right corners. 87

A.4 Zuper Black ink particles during cycles 16 – 20 of sonication (left to right), where each cycle comprises 10 frames (top to bottom). Each frame corresponds to a $36 \times 36\,(\mu\mathrm{m})^2$ area. Time stamps, in nanoseconds, are in the lower right corners. 88

A.5 Experimental setup of the probe sonicating a tissue-mimicking phantom with a cuboid well filled with distilled water. A St Helena £1 coin has been added for scale and three-dimensional perspective. 89

A.6 Unmarked (a) and marked (b) brightness-mode scan of a cuboid well filled with distilled water (DW) surrounded by phantom material (PH). The vertical separations between phantom and distilled water are indicated by yellow lines and zones of increased scattering amplitudes by opaque blue lines. 89

A.7 Additional experimental setup of the probe sonicating a tissue-mimicking phantom with a cylindrical well filled with distilled water. A St Helena £1 coin has been added for scale and three-dimensional perspective. 90

List of Tables

1.1 Common pigments used in tattoo inks, adapted from [28]. 3

5.1 Measured values of the speed of sound compared with literature values. 51

List of Symbols and Abbreviations

The principal symbols and abbreviations used in this thesis are summarised below.

2D	two dimensional
3D	three dimensional
A_{ij}	area of particle i in frame j
A_j	amplitude of scatterer j in altered medium
Ar_0	source function
B_1	peak pressure at proximal interface
B_2	peak pressure at distal interface
$\frac{B_{1,n+1}(t)}{B_{1,n}}$	ratio of scattered amplitudes from the proximal interface
B_i	peak signal recorded at proximal interface
B_{i+1}	peak signal recorded at distal interface
BCE	before the common era
c_n	speed of sound in medium n
c_t	speed of sound in tissue
c_ϕ	speed of sound in phantom material
CAS	chemical abstract service
C.I.	colour index

d_i	thickness of medium i between proximal and distal interfaces
f	frequency
f_c	centre frequency
f_r	resonance frequency
HIFU	high-intensity focussed ultrasound
IMT	intima-media thickness
IN	inked
MSK	musculoskeletal
Nrv	nerve
p_0	ambient pressure
p_a	pressure amplitude
p_g	gas pressure
p_L	Laplace pressure
p_s	surface pressure
p_v	vapour pressure
p_θ	threshold pressure
$\Delta p(t)$	pressure change
PB	pork belly
PH	phantom
r_1	axial distance from origin to proximal interface
r_2	axial distance from origin to distal interface
r_1'	perceived distance from origin to proximal interface

r_2'	perceived distance from origin to distal interface
r_i'	perceived distance from origin to proximal interface
r_{i+1}'	perceived distance from origin to distal interface
R_0	resting radius
R_c	core radius
R_i	instantaneous radius
R_i	reflection coefficient of the proximal interface
R_{ij}	radius of particle i in frame j
$R_{i,\mathrm{A}}$	reflection coefficient of the proximal interface in altered medium
$R_{i,\mathrm{U}}$	reflection coefficient of the proximal interface in unaltered medium
R_{i+1}	reflection coefficient of the distal interface
$R_{i+1,\mathrm{A}}$	reflection coefficient of the distal interface in altered medium
$R_{i+1,\mathrm{U}}$	reflection coefficient of the distal interface in unaltered medium
R_max	maximum radius
R_n	reflection coefficient at the proximal interface of medium n
R_θ	threshold radius
t	time
t_j	time in frame j
U_j	amplitude of scatterer j in unaltered medium
UA	unaltered
UCA	ultrasound contrast agent
V	volume

V_0	resting volume
Z_n	acoustic impedance of medium n
α_{A}	attenuation coefficient of altered medium
α_i	attenuation coefficient of medium i between proximal and distal interfaces
α_n	attenuation coefficient of medium n
α_{t}	average attenuation coefficient of tissue
α_{U}	attenuation coefficient of unaltered medium
γ	ratio of specific heats
θ_{c}	critical angle
θ_{r}	re-refracted angle
ρ_n	density of medium n
ρ_ϕ	density of phantom material
σ	surface tension
ϕ_{c}	perceived angle
ϕ_{r}	perceived re-refracted angle

Chapter 1

Introduction

Tattooing has been around for thousands of years. While the true origin of tattooing is not well known, there are records of tattooing dating to at least the 5^{th} century before the common era (BCE). Radiocarbon dating has ascertained that the oldest discovered human remains with visible tattoos were those of the Tyrolean iceman known as Ötzi, dating to 3370–3100 BCE [1].

From these ancient starts, presently there is an increasing prevalence of tattoos across the globe. This increase in prevalence has been reported in the United States of America, where the prevalence in 2006 was 24 % [2], increasing to 31 % in 2019 [3]. This increasing prevalence of tattoos has also been reported in Australia, from 10 % in 1998 to 15 % in 2004–2005 [4]. As it stands, there is no comprehensive data on tattoo prevalence world-wide. However, the prevalence of tattoos appears to be in the range of 8 % – 38 % [2–6].

Of the tattooed population, it is estimated that between 7 % – 37 % of these tattoo wearers regret their decision to be tattooed [7–9]. The most common reasons for this regret is noted to be getting the tattoo at a young age, the inexperience of the tattoo artist as well as dissatisfaction or embarrassment with the tattoo [7–11].

1.1 What is a tattoo?

The term “tattoo” originates from the Tahitian word “tattau”, which roughly translates as “to mark” [12–15]. A tattoo, depicted in Figure 1.1, is the creation of permanent physical markings of the skin by inserting pigments approximately 1–2 mm into the skin [15, 16]. These pigments remain in the dermis layer of the skin.

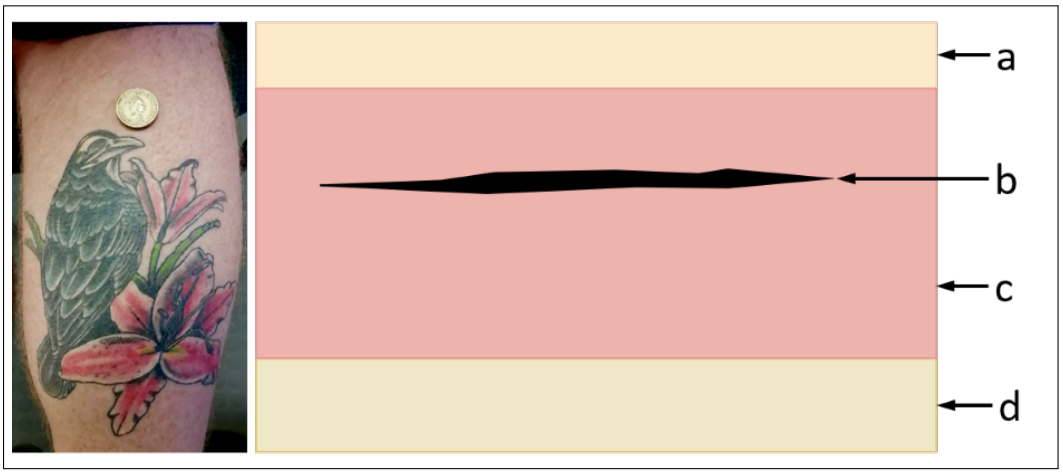


Figure 1.1: Example of a tattoo on a calf (left) and graphical representation of a tattoo in the skin (right). The epidermis layer (0.1–1.5 mm thickness) (a), *in situ* tattoo ink layer (b), dermis layer (1.5–4.0 mm thickness) (c), and the start of the subcutaneous tissue layer (d) are shown to indicate the relative position of the tattoo in the skin.

Tattoos are created intentionally for cosmetic or therapeutic purposes, or unintentionally as a result of pigment entrapment during trauma [15, 17, 18]. Cosmetic tattoos are requested for a variety of personal reasons. These typically include establishing personal identity and displaying uniqueness [12, 16, 19]; an expression of individuality [20, 21]; and as means of representing memories [6, 22]. Therapeutic tattoos find uses as markers in chemo-radiation; correction of corneal pathologies; and as a complement to breast reconstruction [23–27].

1.2 What are tattoo inks?

The inks used to create these permanent dermal markings consist of non-soluble nanoparticles that are most commonly suspended in an aqueous solvent [28,29]. These nanoparticle-based inks comprise predominantly organic pigments [30]. Table 1.1 details some of the common pigments that are used in tattoo inks [28].

Concerns have been raised around these naturally occurring and industrially developed pigments regarding their safety for use in the body [31]. This has been partially addressed through the approval of chemical safety guidelines as well as other regulations [28, 32, 33]. However, these guidelines and regulations still do not make provision for the use-specific applications in tattooing, particularly around the safety of the inks for use in the body.

Table 1.1: Common pigments used in tattoo inks, adapted from [28].

Colour	Pigment Name	CAS No.[1]	C.I.[2]
Red	Pigment Red 210	61932-63-6	C.I.12477
Yellow	Pigment Yellow 74	6358-31-2	C.I.11741
Blue	Pigment Blue 15	147-14-8	C.I.74160
Green	Phthalocyanine Green G	1328-53-6	C.I.74260
Black	Carbon Black 6	1333-86-4	C.I.77266
White	Titanium Dioxide	13463-67-7	C.I.77891

[1] CAS No. refers to the Chemical Abstract Service of the American Chemical Society (CAS) registry number.

[2] Colour Index (C.I.) pigment name prepared by the Society of Dyers and Colourists.

The concern around the safety of tattoos inks appears to be well-founded since many potential health complications may arise as a result of getting a tattoo. The most common health complications evidenced in literature are infections; allergic reactions; skin elevation; itching; photosensitivity; granulomas; and tumours [7, 15, 34]. It should be noted that, based on an extensive review, there have only been 50 reported cases of skin cancer on a tattoo, so this observation may be coincidental [34, 35]. Patients that experience persistent skin irritations as a result of their tattoos have been noted to experience a lower quality of life due to the constant discomfort, which warrants correct diagnosis and treatment with the same intent as other skin diseases receive [36].

It is important to note that the most common colour of tattoos are black [31, 37]. It is also important to note that the vast majority of tattoo-related medical complaints result from black tattoo ink [7, 31].

1.3 How are tattoos created?

Considering how long tattooing has been in existence, one would expect the technologies to have changed quite significantly. Fundamentally the mechanism of inserting the pigments into the skin has not changed, but the tools to assist with the administration process is where technologies have advanced.

Tattoos were originally introduced by making an incision or burning the skin followed by rubbing the pigments into the wounds [18, 38]. The next advancement was the

placement of the ink directly on the skin and a needle was used to poke the ink into the skin [38]. A method that is still used today is the process of hand poking [18]. This is where a needle (or group of needles) is fixed to a handle, dipped in the ink and then poked into the skin. This can either be hand-held or resting against a bar and hit into the skin in a controlled manner.

The most significant advancement in modern tattoo machines can be traced back to 1890 when the first electrical tattoo machine was patented [39]. Intriguingly, this tattoo machine was based on the patent awarded to Thomas Edison in 1876 for a device to make painting and embroidery patterns, using a rotary motor to drive the needles [13, 39]. Dissatisfied with this mechanism, in 1877 Thomas Edison received another patent for a similar device, but using electromagnetic coils instead. This serves as the fundamental design for the most common "coil" machines that are used to this day, while the "rotary" machines are growing in preference due to lower vibrations and overall lighter machine [38, 39].

Other advancements in the area of tattoo administration did not change the mechanism of operation, but rather around the disposable utilities such as grips and needles [39]. These advancements allow for a greater level of safety and sterility to be maintained during the tattoo administration process.

1.4 How are tattoos removed?

As with any industry, where there is a way to administer, there will need to be a way to remove for various reasons. In the case of tattoos, when the option of covering them up (by adding more ink over the existing tattoo) is not desired, the only other option is to have it removed. Several options exist for the removal of tattoos, some of which have fallen out of favour due to associated risks and advancements in removal technologies. The known methods of tattoo removal can be grouped into three fundamental mechanisms of action – mechanical; chemical; or thermal [16, 37, 40–43].

Mechanical methods of removal include salabrasion; dermabrasion; as well as surgical excision. Salabrasion is the process of abrading the skin with coarse granules of salt with a moist gauze pad, followed by applying salt to the wound and leaving it under a sterile dressing for 24 hours before cleaning the wound. Dermabrasion is a similar tissue destruction method where the skin is chilled and abraded using a wire brush. Surgical excision is the most controlled mechanical method, where the tattooed skin is surgically cut out. All of these mechanical methods have a high risk of scarring

due to the destructive nature of the skin during removal.

Chemical methods of tattoo removal involve the puncturing of the skin and the insertion of chemical compounds, such as tannic acid and silver nitrate, into the punctured area. These chemicals react with the skin causing the tattoo to be removed during the healing process.

The current gold standard for tattoo removal is laser treatment, relying on thermolysis of the pigments as the mechanism of removal. Lasers have been used since the 1970s, and rely on a wide variety of different wavelengths and pulse lengths to achieve the desired thermal heating of the targeted area to cause fractionation of the pigment particles such that they can be absorbed by the body. The most common devices currently utlise Q-switched Nd:YAG lasers. Some lasers may cause skin ablation, and there is a risk that the laser treatment will result in incomplete tattoo eradication, pigmentation changes of the exposed area and even scarring. Recent advancements in laser treatments for the removal of tattoos focus on the improvement of the efficiency and safety of the laser by reducing the pulse length to the picosecond range to achieve quicker heating of the targeted area [42, 44]. Another area of improvement that has been considered is the microencapsulation of the pigments such that the ink particles are more responsive to the laser treatments [18, 45].

A modified method of ablative laser treatment has been presented, incorporating high-intensity focussed ultrasound (HIFU) [46]. The inclusion of HIFU as part of the treatment allowed for the removal of tattoos at a lower radiant laser exposure which reduced treatment times. HIFU may be a possible mechanism to remove tattoos by fracturing particles, demonstrated using a proof-of-concept mechanical model [47]. It was found that the particles used to simulate tattoo inks were fractured, with a dependency on the ultrasound pulse length and intensity. The flaw in this study is that the particles chosen to represent tattoo pigments were selected based on the available ultrasound transducer, resulting in a particle size significantly larger than reality. This brings doubt to the results since the true resonant frequency of tattoo pigments would be unreasonably high. Instead of focussing on the fractionation of particles, HIFU has been demonstrated to be an effective mechanism of removal when ablating the tattoo and surrounding skin [48]. This ablative process resulted in longer healing times when compared to laser treatment. However, there was minimal scarring and post-treatment irritation.

1.5 Dynamics of ultrasound

Knowing that HIFU can play a role in the manipulation of tattoos, one might wonder if low-intensity ultrasound may play a similar role. Although ultrasound is most commonly used for medical imaging [49], it is also known to cause a dynamic behaviour of various particles, tissues and bubbles [50–55]. It is regularly applied to manipulate [56], deform [57], and disrupt microscopic particles [58]. Ultrasound can also disperse particles by means of inertial cavitation or acoustic streaming [59]. It has previously been shown that C65 carbon black is hydrophobic and is acoustically active at diagnostic ultrasound pressures [60]. Since carbon black is the pigment in black tattoo ink, it is hypothesised that black tattoo ink would exhibit the same behaviour. As such, carbon black could be considered an antibubble. Antibubbles exhibit symmetric oscillations at low acoustic amplitudes, and asymmetric oscillations at high acoustic amplitudes [61, 62]. This dynamic behaviour is of particular interest for ultrasound contrast agents (UCAs) to improve image quality [53, 63, 64]

1.6 Research question

What is interesting to note, while tattoos are so old and there is a lot of research presented in certain areas of the field, there are significant gaps in the knowledge base. This is particularly evident regarding the properties of the ink. Additionally, aside from the use of ultrasound to either facilitate tattoo removal or as the mechanism of ablative removal, there has been no further research on the effects of ultrasound on tattoos and tattoo inks.

Considering the limited areas of research on tattoos, this thesis seeks to answer the following research question:

To what extent can ultrasound be used to further the understanding of tattoos and tattoo inks?

This research is important because people want to detect, modify and remove tattoos.

1.7 Research objectives

To answer the research question and begin to address some of the gaps in the knowledge base, the following objectives will be addressed in this thesis:

Objective 1
To determine the size distribution and resonance frequency of the pigment particles in black tattoo ink.

Objective 2
To quantify the speed of sound and attenuation coefficient of pure black tattoo ink using ultrasound.

Objective 3
To determine the nucleation threshold of black tattoo ink.

Objective 4
To quantify the change of the speed of sound and attenuation coefficient in tissues due to *in situ* black tattoo ink using ultrasound.

Objective 5
To describe the artefacts that tattoos introduce on ultrasound images.

Objective 6
To demonstrate the sharpening effect of ultrasound on fixed blade cutting devices.

1.8 Rationale

To Objective 1
As has already been highlighted, black tattoos are most common and account for a majority of medical complications. Hence, this research was restricted to consider black tattoo ink only rather than dilute the focus across multiple different pigments. With this limitation in mind, the outcome of Objective 1 is the crucial first step to determine the ultrasound acoustic regime that the black pigment responds to. This is achieved by measuring the size distribution of the pigment particles, and relating their size to a corresponding resonance frequency.

To Objective 2

The next step to develop the understanding of tattoo ink is to determine the speed of sound and attenuation coefficient, considering undiluted black ink. For the purposes of this research, the pigment particles are modelled as antibubbles. It is acknowledged that non-linear oscillations of antibubbles contribute to non-linear forward scattering phenomena. This can contribute to a non-linear attenuation due to an energy shift to higher harmonics. However, to compare the attenuation with other biomaterials, the analysis considers linear attenuation only.

To Objective 3

Considering the common desire to have a tattoo removed, it is beneficial to understand what conditions are required to manipulate the pigment particles. Due to the hydrophobic nature of carbon black, it is hypothesised that black tattoo ink will exhibit similar nucleation events as has previously been observed. The nucleation threshold of the pigment particles gives insight to the possibility of manipulation at diagnostic pressures. This could indicate other potential uses of the pigment particles. These experiments are performed using diluted black ink such that the behaviour of individual pigment particles could be observed.

To Objective 4

The extreme cases of undiluted and diluted black ink have been considered in Objectives 2 and 3, respectively. However, neither case is representative of an *in situ* tattoo. Therefore it is necessary to consider the case of a thin ink layer in tissue. The change in acoustic properties of the tissue due to the presence of ink is quantified. The process of tattooing is traumatic to the tissue. Artificial and pork skin maintain a visually smooth surface after tattooing and are included as tissue-like materials. Tissue-mimicking phantom is not considered due to a visually inconsistent surface after tattooing.

To Objective 5

Tattoos are essentially thin layers of pigment particles which should locally alter the acoustic properties of the tissue, as demonstrated in Objective 4. This begs the question – would this change cause visible artefacts on ultrasound images? This is treated by considering the vertical transitions between tissues with different acoustic properties of the resulting brightness-mode images.

To Objective 6

Understanding the effect ultrasound has on black tattoo ink for potential manipulation is one side of the equation. The effect of ultrasound should also be considered for

the introduction of tattoos. Tattoos are introduced using a set of rapidly oscillating needles. The trauma of these needles on tissue is not trivial to observe under a microscope. Even considering the effect the needles have on a simple sheet of paper is not easily visualised. Consequently, the effect of applying ultrasound to the needle would not be easily visualised either. Therefore a fixed-blade cutting device is regarded representative for the tattoo needle to observe the sharpening effect of ultrasound.

1.9 Outline

Chapter 2 presents the particle size distribution of black tattoo ink, as well as a method to characterise materials using the received brightness-mode image from a medical ultrasound device. Using this method, the speed of sound and attenuation coefficient were determined for black tattoo ink, saline and distilled water. From this, it was noted that black tattoo ink attenuates ultrasound. This chapter serves to address Objective 1 and Objective 2.

This chapter is based on the following article:
C. S. Carlson, A. Deroubaix, C. Penny, and M. Postema, "On the attenuation of ultrasound by pure black tattoo ink," *SAIEE Africa Research Journal*, vol. 112, no. 1, pp. 24–31, 2021.

Chapter 3 extends on the study of attenuation of ultrasound by black tattoo ink noted in Chapter 2. It was observed under high-speed photography that the carbon black pigment demonstrates transient nucleation characteristics. This chapter serves to partially address Objective 3.

This chapter is based on the following conference proceeding:
C. S. Carlson, R. Matsumoto, K. Fushino, M. Shinzato, N. Kudo, and M. Postema, "Transient ink nucleation: the proof is in the pudding," in *Proceedings of the 41st Symposium on Ultrasonic Electronics*, no. 2E5–1, 2020.

Chapter 4 presents the derived theory and evaluates the nucleation threshold of carbon black pigment used in black tattoo inks. The nucleation threshold was found to be lower than the Blake cavitation threshold of 2.0× the resting radius of free, unencapsulated microbubbles. This chapter serves to partially address Objective 3.

This chapter is based on the following article:
C. S. Carlson, R. Matsumoto, K. Fushino, M. Shinzato, N. Kudo, and M. Postema, "Nucleation threshold of carbon black ultrasound contrast agent," *Japanese Journal of Applied Physics*, vol. 60, no. SDDA06, 2021.

Chapter 5 presents a method for computing the acoustic response from horizontally and vertically layered media containing a thin inked layer, introducing the concept of critical refraction highlighting. The speed of sound and attenuation coefficient of the tissues investigated were determined, using this method together with brightness-mode images from controlled *in vitro* experiments. The artefacts observed at the separation point between media with different speeds of sound on brightness-mode ultrasound images can be explained by the concept of critical angle highlighting. This chapter serves to address Objective 4 and Objective 5.

This chapter is based on the following article:
C. S. Carlson, and M. Postema, "Deep impact of superficial skin inking: acoustic analysis of underlying tissue," *BIO Integration*, vol. 2, 2021.

Chapter 6 describes a fixed blade ultrasound cutting device that has minimal heating effects over the blade. Microscope images of the edges of the sonified cuts are presented and compared to unsonified cuts with the same device to demonstrate the effect that ultrasound has on the cutting efficiency. This chapter serves to address Objective 6.

This chapter is based on the following article:
C. S. Carlson, A. Pohl, D. G. Keir, and M. Postema, "Cutting edge technology: sound sharpens the blade," *Applied Acoustics*, vol. 166, no. 107336, 2020.

Chapter 7 discusses the key findings of this thesis, identifying to what extent the research objectives were met and the limitations of the findings.

Appendix A provides supplementary material, where publications were restricted in the number of pages and figures.

Chapter 2

Ink Attenuation of Ultrasound

This chapter is based on: C. S. Carlson, A. Deroubaix, C. Penny, and M. Postema, "On the attenuation of ultrasound by pure black tattoo ink," *SAIEE Africa Research Journal*, vol. 112, no. 1, pp. 24–31, 2021.

The author conceptualised the work; performed the experiments; analysed the data; and wrote the majority of the article.

Abstract

Black tattoo ink comprises hydrophobic carbon black nanoparticles. We hypothesised that black tattoo ink demonstrates transient dynamic activity in an ultrasound field. Brightness-mode sonography was performed on cylindrical receptacles of different bore diameters, filled with black tattoo ink, water, saline, or air, using pulsed ultrasound with centre frequencies of 13 MHz and 5 MHz. The scattering from black ink itself lasted less than ten minutes. At 13-MHz sonication, a transient drop in sound speed was observed, as well as a transient lessening of scattering from distal phantom tissue. The linear acoustic attenuation coefficient of pure black ink was measured to be $0.15 \pm 0.01\,\mathrm{dB\,cm^{-1}\,MHz^{-1}}$, equal to whole blood. Low-intensity ultrasonic tattoo removal would be of interest as an alternative to techniques that damage surrounding tissue.

2.1 Introduction

Tattoos have been under investigation for their role in society [20, 65], in physical health [34–36, 38], and even in mental health [12, 66]. Ultrasonic imaging has been used to monitor dermatological tattoo complications [67, 68]. In addition to laser ablation [43], ultrasound has also been experimentally applied for tattoo removal [46, 48]. The high-intensity focussed ultrasound used for this purpose ablates the tissue in or near the transducer focus, irrespective of the presence of ink. To date, no studies have investigated the acoustic properties of tattoo ink particles themselves and their response to an incident low-amplitude sound field.

The most common tattoo colour is black [31, 37]. As the vast majority of tattoo-related medical complaints result from black tattoo ink [7, 31], this type of ink is the primary focus in tattoo modification and removal. Black tattoo ink comprises carbon black nanoparticles [28, 69]. As carbon black nanoparticles demonstrate transient dynamic activity in an ultrasound field [60], we hypothesise that black tattoo ink exhibits similar behaviour. The purpose of this study is to investigate transient and steady-state behaviour of black tattoo ink under sonication.

Although an early study on the interaction of ultrasound and carbon black was applied to the identification of components for smart battery recycling [70], our primary long-term purpose with the present study is to deposit acoustic energy into particles suitable for superficial human injection, thereby directly heating the particles and indirectly the surrounding tissue. This might facilitate sonic tattoo removal at low, nondestructive acoustic intensities.

Numerous studies have been dedicated to the experimental determination of the sound-absorbing properties of biological tissue [71–75], tissue-mimicking phantoms [76, 77], salty water [78, 79], and combinations thereof [80]. Although their structures may appear solid, from a physics point of view, most tissues studied in medical ultrasonography are considered fluids [81].

Sound absorption in fluids can be mainly attributed to viscous and thermal damping. The viscous damping corresponds to the friction associated with the relative motion of the particles. The viscous damping coefficient in fluids is proportional to the squared transmission frequency. Thermal damping is the mechanism whereby a fraction of the energy carried by the propagating wave is converted into heat by thermoelasticity. In most liquids and solids, the thermal damping coefficient can be neglected, but in gases it accounts for roughly a third of the total damping [81].

Consequently, bulk fluid absorbs sound better if there is gas presence. If the gas presence is transient, so must the absorption. Hydrophobic particles in suspension have a gaseous surrounding layer, referred to as a void [82]. This void is compressible. Just like all other compressible entities, hydrophobic particles in suspension can oscillate, move, attract, and repel each other under the influence of sound, owing to so-called Bjerknes forces [83].

Hydrophobic carbon black nanoparticles are only transiently acoustically active [84]. Some of these particles have been observed to lose their surrounding voids whilst oscillating. Once dehydrophobised, they appeared to remain inactive in an ultrasound field [60]. Consequently, we speculate, that the state of hydrophobicity must influence the thermal damping of ultrasound propagating through the fluid. The voids, once released, become free gas microbubbles. These must dissolve within milliseconds [81]. The presence of freely oscillating microbubbles must influence the speed of sound in the medium [83].

The ultrasonic transmission frequencies used in [60, 84] were 45 kHz and 1 MHz. These frequencies were much lower than the resonance frequencies of the particles under sonication. To exploit Bjerknes forces for actual physical manipulation of nanoparticles, one would need to sonicate at a frequency much closer to the resonance frequencies of the particles [81].

The resonance frequency of a hydrophobic particle can be estimated from [61], where the optically observed radius of a particle in suspension, which includes the void, is taken for the outer radius, and the dry particle radius is taken for the inner radius. It is noted that the derivation of the oscillating and translating dynamics of a spherically symmetric hydrophobic particle is identical to that of an antibubble [85]. It is also noted that the largest particles in a population contribute most to the acoustic response of that population [83].

In a preliminary study, the acoustic conditions for tattoo removal were modelled assuming ink particle sizes greater than 50 μm [47]. This assumption is, for some inks, a factor of 1000 off, as black ink particles may be as small as 40 nm in diameter [28,29]. Using atomic force microscopy, the diameters of black ink particles were measured to have a mode of 0.24 μm [29]. The largest black ink particle had a diameter of 0.97 μm [29].

To determine which ultrasonic frequency to use in our experiments, we needed to measure the size distribution of the black ink particles in solution and to compute the corresponding resonance frequencies.

In this study, ultrasound images from a diagnostic scanner were recorded from black tattoo ink contained in various receptacles, with a focus on the variation of backscattering over time from the ink and from distal scatterers.

2.2 Theory

The linear acoustic attenuation coefficients of the media under investigation were computed, correcting for tissue attenuation compensation of the device [86] and taking into account the geometric spreading of a point scatterer and a dual interface system with opposing reflection coefficients [87]:

$$e^{2f_c[\alpha_n(r_2-r_1)-\alpha_t(r_2'-r_1')]}=\frac{B_1}{B_2}\frac{r_1}{r_2}(1+R_n)(1-R_n), \tag{2.1}$$

where f_c is the centre frequency of the ultrasound pulse, B_1 is the proximal peak, B_2 is the distal peak, r_1 is the axial distance to the proximal interface, r_1' is the perceived distance to the proximal interface, r_2 is the axial distance to the distal interface, r_2' is the perceived distance to the distal interface, α_n is the acoustic attenuation coefficient of medium n, α_t is the average attenuation coefficient in soft tissue [72], and R_n is the pressure reflection coefficient at the proximal interface, given by

$$R_n = \frac{\rho_n c_n - \rho_\phi c_\phi}{\rho_n c_n + \rho_\phi c_\phi}, \tag{2.2}$$

in which c_n is the speed of sound in medium n, c_ϕ is the speed of sound in the phantom material, ρ_n is the density of medium n, and ρ_ϕ is the density of the phantom material. The units of the attenuation coefficients computed were converted from [$\mathrm{Np\,m^{-1}\,MHz^{-1}}$] to [$\mathrm{dB\,cm^{-1}\,MHz^{-1}}$] by multiplication by a factor $2000\log_{10}e$.

A change in the speed of sound in the well medium must result in a change in the perceived distance to the distal interface. The time-dependent speed of sound of medium n was computed using

$$c_n(t) = \frac{r_2 - r_1}{r_2'(t) - r_1'}\,c_t. \tag{2.3}$$

The speed of sound directly measured from (2.3) was evaluated, knowing that, at a given distance r_1, for a probe with source function $A\,r_0$, the ratio of scattered amplitudes from the proximal interface

$$\frac{B_{1,n+1}(t)}{B_{1,n}}=\frac{\frac{Ar_0}{r_1}e^{2f_c(\alpha_t r_1'-\alpha_\phi r_1)}\,|R_{n+1}(t)|}{\frac{Ar_0}{r_1}e^{2f_c(\alpha_t r_1'-\alpha_\phi r_1)}\,|R_n|}=\left|\frac{R_{n+1}(t)}{R_n}\right| \tag{2.4}$$

must equal the ratio of reflection coefficients for different well media, yielding

$$\frac{B_{1,n+1}(t)}{B_{1,n}} = \left| \frac{\rho_{n+1}c_{n+1}(t) - \rho_\phi c_\phi}{\rho_n c_n - \rho_\phi c_\phi} \right|. \tag{2.5}$$

The influence of nucleation on the attenuation coefficient was estimated by substituting the mean grey level distal of the distal interface for B_2 in (2.1) and multiplying the right-hand side by $(1 + R_n)(1 - R_n)$ once more, adding an extra transmission interface. Note that r_2 is not changed, as the size of the well has not changed.

2.3 Materials and methods

Zuper Black pigment dispersion (INTENZE Products, Inc., Rochelle Park, NJ, USA) was used for black ink. Undiluted black ink was measured to have a density of $1313\,\mathrm{kg\,m^{-3}}$.

For size distribution estimation, bright-field microscopy images were captured of a 0.01% dilution of Zuper Black using the bright-field component of a ZEISS LSM 780 confocal laser scanning microscope with an alpha Plan-Apochromat 63×/1.40 NA Oil CorrM27 objective lens (Carl Zeiss AG, Oberkochen, Germany) [88].

Figure 2.1 shows the size distribution histogram and a graph of the particle resonance frequency as a function of its diameter. The mode of the diameters measured was $0.29\,\mu\mathrm{m}$ and the largest diameter was $1.14\,\mu\mathrm{m}$. Dividing the dry particle mode from [29] by the mode measured from our wet ink particles, and dividing the largest particle diameter from [29] by our largest wet particle diameter yielded $\frac{0.24\,\mu\mathrm{m}}{0.29\,\mu\mathrm{m}} \approx \frac{0.97\,\mu\mathrm{m}}{1.14\,\mu\mathrm{m}} \approx 0.8$. Thus, the resonance frequencies were computed from [61, eq. 1], approximating the inner-to-outer diameter ratio by 0.8. Our largest particle had a resonance frequency of 15 MHz. All other ink particles had greater resonance frequencies than 15 MHz. To be certain that all particles oscillated in anti-phase with respect to the incident sound field [81], we chose operating frequencies slightly less, at 13 MHz, and substantially less, at 5 MHz.

Our ultrasonic experiments were carried out in a Perspex container of 580×235×65 $(\mathrm{mm})^3$ internal dimensions, which was filled with degassed water. A line drawing of the experimental setup is shown in Figure 2.2. The setup had been designed for optically observing microscopic biomaterials under sonication [89, 90].

Either an HFL38x 13–6 MHz linear probe or a C60x 5–2 MHz curvilinear probe of a

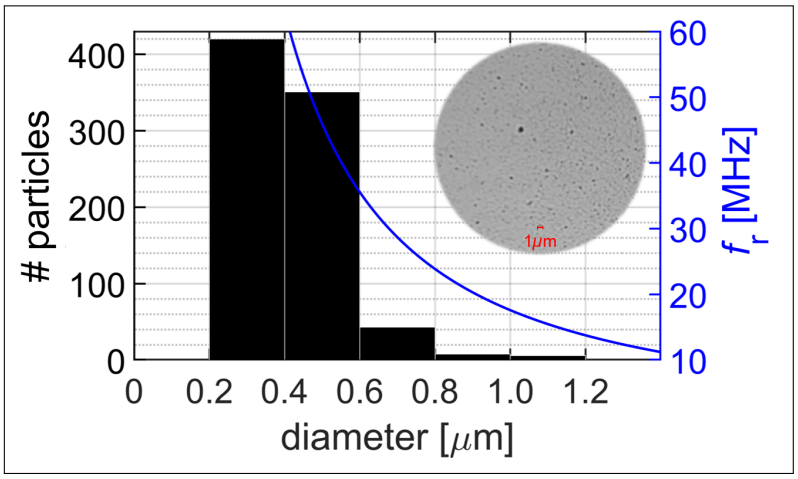


Figure 2.1: Size distribution of Zuper Black pigment dispersion (histogram) and particle resonance frequency as a function of the diameter (curve), with an inlay of a bright-field microscopy image of a 0.01% dilution of Zuper Black at 63× magnification.

SonoSite® M-Turbo® sonography device (FUJIFILM SonoSite, Inc., Bothell, WA, USA) was clamped in the length direction of the container. The sonography device was operating in either intima-media thickness (IMT) or nerve (Nrv) brightness mode. IMT was the default operating mode for the 13–6 MHz probe; Nrv was the default operating mode for the 5–2 MHz probe. The ultrasound penetration depths of the 13–6 MHz probe and the 5–2 MHz probe were set to 6.0 cm and 6.6 cm, respectively.

The sonography device converted two-way travel times to one-way radial distances assuming c_t=1540 m s^{-1} for the speed of sound in tissue. It compensated for tissue attenuation by amplifying the backscattered signal by 0.3 dB cm^{-1}MHz^{-1} by default [72, 86]. In both operating modes, the mechanical and thermal indices had fixed values of 0.6 and 0.1, respectively. Automatic image adjustments had been switched off.

Two tissue-mimicking phantom receptacles with empty cylindrical wells were manufactured according to the method in [91]. A picture of one of the phantom receptacles and its dimensions is shown in Figure 2.3.

The phantom material was measured to have a density of 1025 kg m^{-3}, a speed of sound of approximately 1500 m s^{-1}, and a linear attenuation coefficient of 0.35 dB cm^{-1} MHz^{-1}. A phantom receptacle was placed in the container such that one of its sides touched the probe surface.

Other receptacles used in this study were CUPROPHAN® RC55 cellulose capillaries (Membrana GmbH, Wuppertal, Germany) with a 200-μm bore diameter and an 8-μm

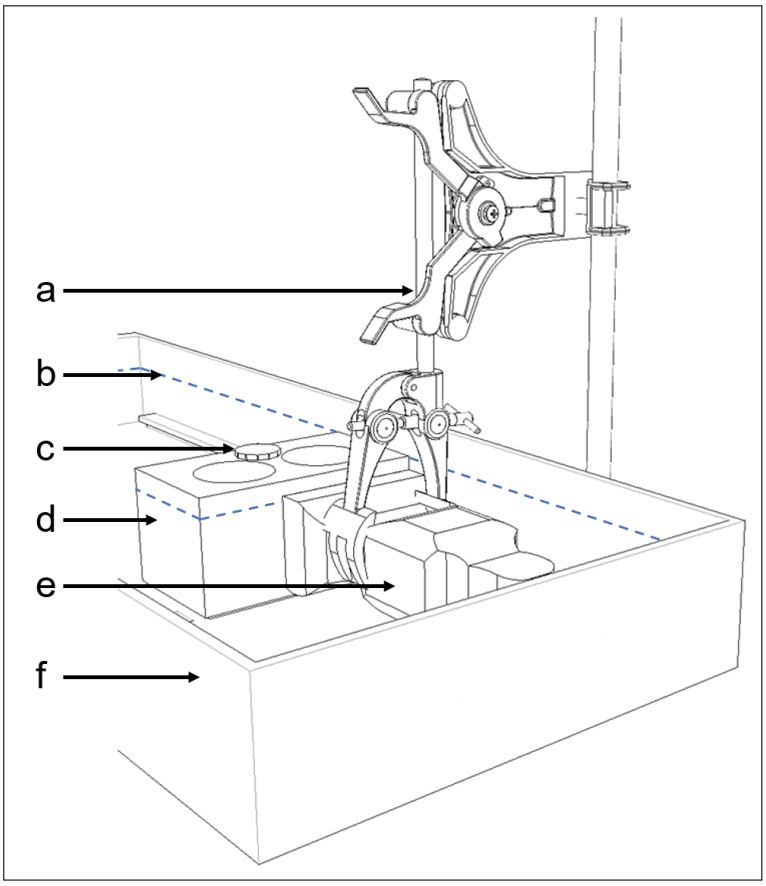


Figure 2.2: Line drawing of the experimental setup, consisting of a burette clamp and stand (a), water, whose level is indicated by a blue dashed line (b), a £1 coin for scale (c), a tissue-mimicking phantom receptacle (d), an ultrasound probe (e), and a Perspex container (f).

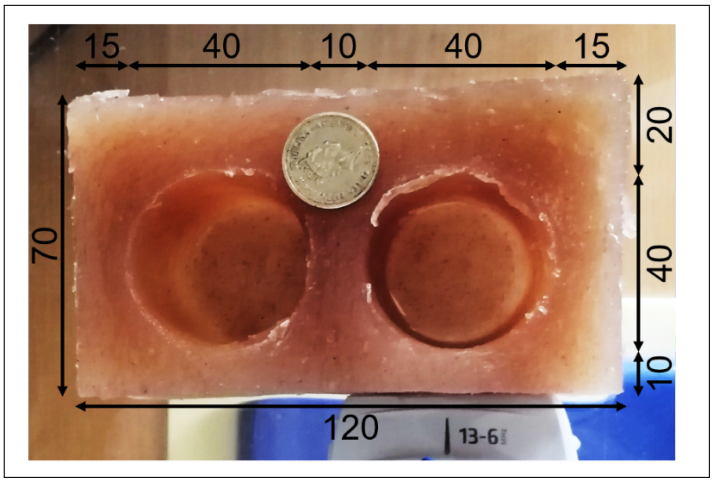


Figure 2.3: Top view of the tissue-mimicking phantom receptacle with two cylindrical wells. Dimensions are in mm.

wall thickness, and RS PRO silicone transparent Silicone Tubing (RS Components (SA), Midrand, South Africa) with a 0.50-mm bore diameter.

Whilst the phantom receptacles were at a fixed position in the container, our most modest receptacles were manually held between 0.6 cm and 1.3 cm in front of the 13–6 MHz probe. For these receptacles, the ultrasound penetration depth was adjusted to 1.8 cm.

The phantom receptacle wells were filled with pure (undiluted) ink using a syringe. The silicone tubes were filled with a 25% dilution using a syringe and the capillaries were filled with a 25% dilution using capillary action. These receptacles were used for calibration and illustration purposes. As the ink had been diluted, these experiments were not used for quantification. For control experiments, receptacles filled with degassed Braamfontein tap water, Reitzer's Distilled Water (Reitzer Pharmaceuticals, Kempton Park, South Africa), SABAX Pour Saline 0,9% (Adcock Ingram Critical Care (Pty) Ltd, Midrand, South Africa), phantom tissue, and air were used.

Sonication continued for ten minutes after each filling, during which images were recorded.

The experiments with the phantom receptacles took place over two consecutive days, the experiments with the other receptacles took place on two separate days. A total of 553 brightness-mode still-frames were recorded using the ultrasound scanner internal storage.

Image processing was done using MATLAB® (The MathWorks, Inc., Natick, MA, USA). In all images recorded, the axial backscattering profiles were extracted on an 8-bit grey scale, after which the absolute peak scatter amplitudes, corresponding to the proximal and distal receptacle interfaces, were measured. In selected images, the mean of the axial scattering from the far field, distal to the last interface, was measured.

To confirm the receptacle parameters, distilled water was used in control experiments in the wells.

2.4 Results and discussion

Figure 2.4 shows 13-MHz brightness-mode scans of a phantom receptacle well with a 40-mm bore diameter and their respective axial profiles. The bright spots inside the

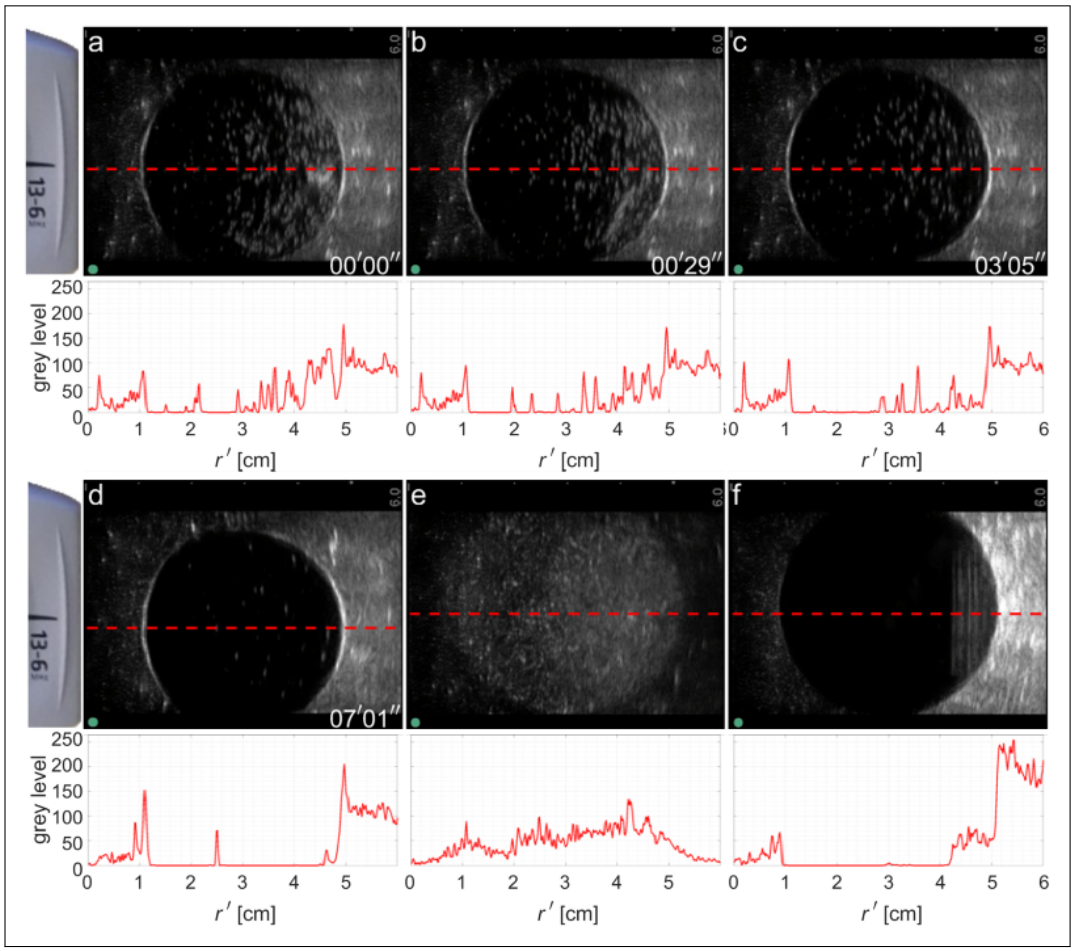


Figure 2.4: Brightness-mode scans at a 13-MHz ultrasound frequency of a phantom receptacle well filled with black ink (a–d), phantom material (e), and distilled water (f); and corresponding axial backscattering profiles [8-bit grey scale] as a function of perceived distance [cm]. Time stamps are relative to (a). The green dot corresponds to the right-hand side of the probe.

circular areas in frames (a–d) indicate scatterers inside the black ink. The number of scatterers decreased over time, but a few are still visible in frame (d).

The axial backscatter of the ink-filled well shows first peaks at a 1-cm axial distance with 8-bit grey levels rising from 84 (a) to 152 (d). These peaks correspond to the proximal phantom–well interface. The second peaks, at a 5-cm axial distance, correspond to the distal phantom–well interface. These second-peak values rose from 199 to 215 during the 7′01″ image sequence. Although not visible with the naked eye, the perceived distance between the peaks is 0.16 mm less between frames (c) and (d), indicating a change in the speed of sound. From (3), it followed that the speed of sound of ink was $1621\,\mathrm{m\,s^{-1}}$ in (a) and $1627\,\mathrm{m\,s^{-1}}$ in (d).

The axial backscatter of the water-filled well had a proximal peak grey levels of 67 and a distal level of 244. Substituting the values obtained from (2.3) into the right-hand side of (2.4) resulted in a reflection coefficient ratio between ink (d) and water (f) of -2.25. The ratio of proximal peaks in (d) and (e) was 2.27. Thus, compared to the level from ink, this low proximal amplitude of distilled water can be attributed to the difference in reflection coefficients. Although the density of nucleating ink could not be measured directly, it could be computed from (2.5), using (2.4) as pressure-ratio input. The density of nucleating ink was computed to be around $1200\,\mathrm{kg\,m^{-3}}$ in frame (a). Knowing the steady-state density of black ink, this result means that gas comprises 9% of the volume fraction of nucleating ink. This indicates that the cavitation activity is very dynamic.

The device compensation for tissue attenuation created a 16-dB amplification between the two interfaces. Therefore, the scattering from nucleation is actually not just taking place in the distal part of the well cross section, but over the whole cross section. This is supported by the gradient of the grey level as a function of r' inside the well. The higher distal peak levels in frames (a–d) and (f) are also explained from the lack of attenuation of both media compared to the tissue attenuation compensation. The ink distal peak was portrayed 20 dB higher, the distilled water peak 32 dB. The reflection coefficient played only a minor role in the distal peak amplitude: $|R_n|(1+R_n)(1-R_n)$ is $+2\,\mathrm{dB}$ for ink and $-1\,\mathrm{dB}$ for distilled water.

Another indicator of cavitation dynamics is the mean grey level distal to the distal interface. In frames (a–d), the mean distal grey level gradually rose from 96 in (a) to 111 in (d). The mean distal grey level of distilled water (f) was 201. Here, the transmission coefficient played a minor role in the scattered amplitude of a phantom speckle: $(1+R_n)^2(1-R_n)^2$ is $-2\,\mathrm{dB}$ for ink and $+1\,\mathrm{dB}$ for distilled water. These are, however, negligible compared to the device amplification. Therefore, both media have an increased distal grey level, depending on their own attenuation coefficient. As the phantom material itself had an attenuation coefficient slightly higher than that used for tissue compensation, the grey level in (e) gradually declined with distance r according to $e^{-2(\alpha_\phi-\alpha_\mathrm{t})f_\mathrm{c}r}$, in addition to the geometric decline according to r^{-1}. Cavitation activity was also reflected by the attenuation coefficient itself. The attenuation coefficient had increased to approximately $0.2\,\mathrm{dB\,cm^{-1}\,MHz^{-1}}$ in frames (a–d). Its steady state-value was $0.15\pm0.01\,\mathrm{dB\,cm^{-1}\,MHz^{-1}}$, measured in a subsequent image sequence, $13'31''$ later (not shown).

The attenuation coefficient of the carbon black pigment dispersion in steady-state, $0.15\,\mathrm{dB\,cm^{-1}\,MHz^{-1}}$, corresponds to the attenuation coefficient of whole blood [72]

and is just 0.02 dB cm^{-1} MHz^{-1} less than the attenuation coefficient of testes [71]. The attenuation coefficient found for distilled water was 0.00±0.01 dB cm^{-1} MHz^{-1}, which corresponds to the literature value of 0.002 dB cm^{-1} MHz^{-1} [80]. Our attenuation coefficient for saline, 0.02±0.02, corresponds to the literature value 0.01 dB cm^{-1} MHz^{-1} [80]. The steady-state speeds of sound were measured to be 1639 m s^{-1} of ink; of saline 1568 m s^{-1}, and 1480 m s^{-1} of distilled water.

Figure 2.5 shows 5-MHz brightness-mode scans of a phantom receptacle well with a 28-mm bore diameter and their respective axial profiles. Although nucleation activity was visible in the circular areas in frames (a–d), the speed of sound in the ink was not observed to change, nor the attenuation coefficient, which remained steady at 0.15±0.01 dB cm^{-1} MHz^{-1} at this frequency. As the sonicating frequency was approximately one third of the resonance frequency, only stable cavitation and dissolution were to be expected in this acoustic regime.

The device amplification between the two interfaces was 6 dB for ink and 7 dB for saline (f). Contrary to the results at 13-MHz sonication, here the geometric and reflection contributions could not be neglected. The total signal amplification was 3 dB for ink and 8 dB for saline. This amplification is clearly visible at distances greater than the distal interface. The axial cross section from the well filled with phantom material shows a steady decline, supporting the slight difference in attenuation with respect to the device compensation.

In the tubes and capillaries, the ink had been diluted to 25% to make flow into the receptacle possible. Scattering from ink particles inside these receptacles was not observed. Therefore, the influence of dilution on the transient nature and the quantity of acoustic scatterers could not be established. Figure 2.6 shows brightness-mode scans of capillaries with a 0.20-mm bore diameter and their respective axial profiles.

As the wavelength of the 13-MHz ultrasound in water, approximately 0.12 mm, is less than the diameter of the capillary, two capillary walls should be visible if the acoustic impedance difference is sufficiently high. The axial backscattering in the ink-filled capillary had peak 8-bit grey levels of 95 and 114, respectively. The acoustic impedance difference was high enough to make both capillary walls visible. The peak-to-peak distance of 0.28 mm approximated the capillary width.

The backscattering of the water-filled capillary had a peak grey level of 68. Here, no separate walls were visible. This cannot be attributed to the capillary being outside the elevation plane, as the 0.22-mm outer capillary diameter is substantially less than the transducer elevation. The contribution to the acoustic response can be

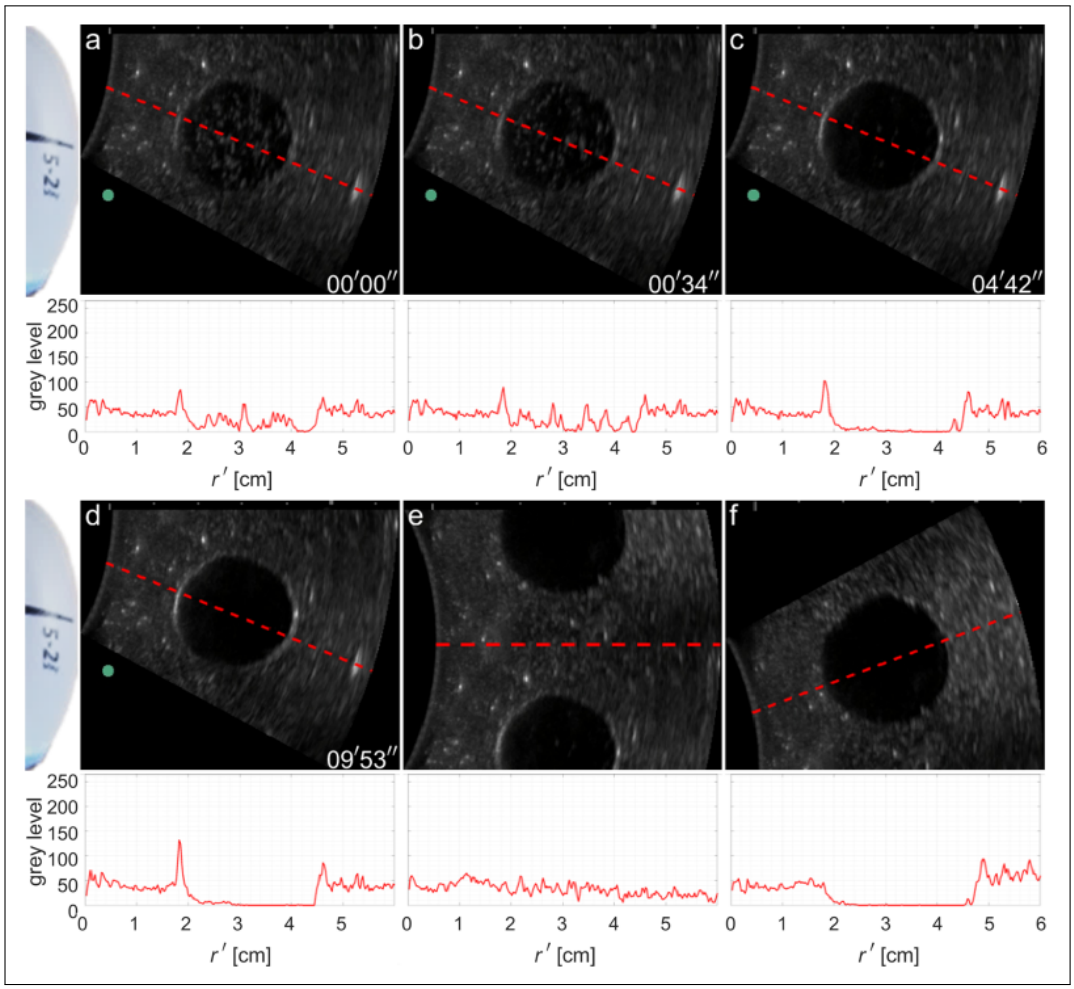


Figure 2.5: Brightness-mode scans at a 5-MHz ultrasound frequency of a phantom receptacle well filled with black ink (a–d), phantom material (e), and saline (f); and corresponding axial backscattering profiles [8-bit grey scale] as a function of perceived distance [cm]. Time stamps are relative to (a). The green dot corresponds to the right-hand side of the probe.

fully attributed to the cellulose material, as the medium inside the capillary was the same as outside. The backscattering of the air-filled capillary had one peak level of 233. Here, separate walls were not visible either. The long axial scattering zone of 0.99 mm (grey level threshold of 20) is explained from the linear oscillating dynamics of the air trapped in the capillary, which responded to the incident sound field. The resonance frequency of the air-filled capillary was less than 50 kHz, too far from the incident sound field frequency to cause any other dynamic effect [81].

These results show that there was a clear acoustic impedance difference between water and black ink. Thus, the black ink acted as a reflector, although it was in 25% dilution. This outcome limits absolute quantification from distal scatterers, as

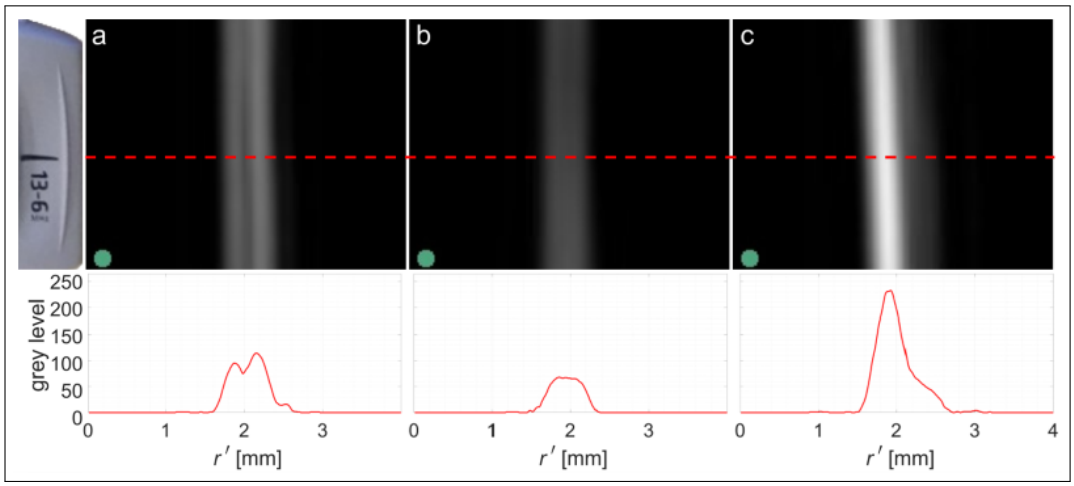


Figure 2.6: Brightness-mode scans of capillaries filled with black ink (a), degassed water (b), and air (c); and their respective axial backscattering profiles on an 8-bit grey scale. The green dot corresponds to the right-hand side of the probe.

the transmitted ultrasound pulse may have changed when passing through an inked region.

2.5 Conclusions

In this study, brightness-mode sonography was performed on ink-filled receptacles, using pulsed ultrasound with centre frequencies of 13 MHz and 5 MHz.

The attenuation coefficient of ink was measured to be $0.15\pm0.01\,\mathrm{dB\,cm^{-1}\,MHz^{-1}}$, of saline $0.02\pm0.02\,\mathrm{dB\,cm^{-1}\,MHz^{-1}}$, and of distilled water $0.00\pm0.01\,\mathrm{dB\,cm^{-1}\,MHz^{-1}}$. The speed of sound of tattoo ink in steady-state was measured to be $1639\,\mathrm{m\,s^{-1}}$, of saline $1568\,\mathrm{m\,s^{-1}}$, and of distilled water $1480\,\mathrm{m\,s^{-1}}$.

Transient scattering from the ink was observed. Backscattering from distal phantom materials was amplified by the presence of carbon black.

The speed of sound in ink was observed to drop to transiently to $1621\,\mathrm{m\,s^{-1}}$ for less than ten minutes during 13-MHz sonication, but not during 5-MHz sonication. The drop in speed at 13-MHz sonication may be attributed to strong, yet transient, cavitation activity, as the resonance frequency of the largest hydrophobic carbon black nanoparticles is 15 MHz.

This finding is useful for the potential deposition of acoustic energy into tattoos with

the purpose of modifying them.

Acknowledgements

The sonography equipment was kindly supplied by High Tech Medical, Randburg, South Africa. Laser scanning confocal microscopy was performed at the Life Sciences Imaging Facility of the University of the Witwatersrand, Johannesburg. This work has been based on research supported in part by the National Research Foundation of South Africa, Grant Number 127102.

Chapter 3

Transient Ink Nucleation

This chapter is based on: C. S. Carlson, R. Matsumoto, K. Fushino, M. Shinzato, N. Kudo, and M. Postema, "Transient ink nucleation: the proof is in the pudding," in *Proceedings of the 41st Symposium on Ultrasonic Electronics*, no. 2E5–1, 2020.

The author conceptualised the work; performed the brightness-mode sonography experiments; analysed the data; and wrote the majority of the article.

Abstract

Hydrophobic particles have been shown to behave as cavitation nuclei during sonication. Black tattoo ink comprises hydrophobic carbon black nanoparticles. In this study, we investigated the inertial cavitation behaviour of black tattoo ink under sonication. Black tattoo ink was observed to transiently nucleate using brightness-mode sonography, and confirmed with high-speed photography. Therefore, ultrasound changes the hydrophobicity of carbon black nanoparticles in black tattoo ink.

3.1 Introduction

Although ultrasonic technology is most commonly used for medical imaging [49], it is also regularly applied to manipulate [56], deform [57], and disrupt microscopic particles [58]. Ultrasound can disperse nanoparticles, a process which has been associated with inertial cavitation and acoustic streaming [59]. High-speed photography is commonly used to study acoustic cavitation dynamics [58, 92].

Hydrophobic particles can be regarded as particles with a thin gaseous layer surrounding the solid cores [82]. They have been observed to act as cavitation nuclei that lose their gaseous layer during sonication [60].

Black tattoo ink comprises hydrophobic carbon black nanoparticles. In this study, we hypothesised that black tattoo ink exhibits similar transient inertial cavitation behaviour under sonication.

3.2 Materials and methods

The first set of experiments was carried out in a Perspex container of $580\times235\times65\,(\mathrm{mm})^3$ internal dimensions, which was filled with degassed water.

A C60x 5–2 MHz curvilinear probe of a SonoSite® M-Turbo® sonography device (FUJIFILM SonoSite, Inc., WA, USA) was clamped in the length direction of the container. The sonography device was operating in brightness mode throughout the experiments.

A $160\times120\times50\,(\mathrm{mm})^3$ tissue-mimicking phantom with three empty cylindrical wells, manufactured according to the recipe [91], was positioned in the container such that its 160-mm-wide front face touched the probe surface. The cylindrical wells, with 28-mm diameter and 42-mm height, were located 20-mm from the front face (*cf.* Figure 3.1).

Zuper Black pigment dispersion (INTENZE Products, Inc., NJ, USA) was used for black ink. 20 mL each of black ink and SABAX Pour Saline 0.9 % (Adcock Ingram Critical Care (Pty) Ltd, Johannesburg, South Africa) was inserted into the centre and right wells respectively.

The ultrasound was set to a penetration depth of 6.6 cm, a mechanical index of 0.6, and a thermal index of 0.1.

The second set of experiments was carried out in the 0.2-mL observation chamber of a high-speed photography system [93].

A quantity of 0.5 μL Zuper Black pigment dispersion was pipetted into a FALCON® 15-mL High-Clarity Polypropylene Conical Tube (Corning Science México S.A. de C.V., Tamaulipas, Mexico), after which 5 mL of 049-16787 Distilled Water (FUJIFILM Wako Pure Chemical Corporation, Osaka, Japan) was added. The tube was

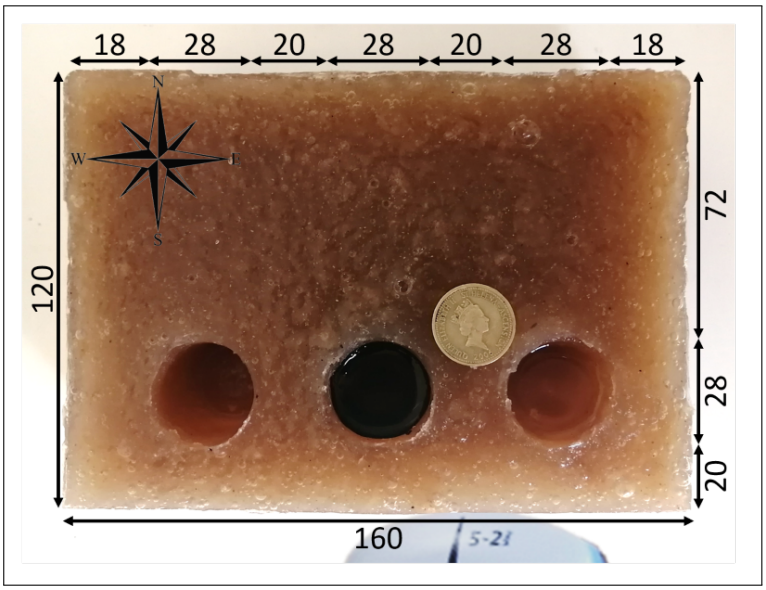


Figure 3.1: Top view of the tissue-mimicking phantom with three cylindrical wells. The probe is visible on the South face. A £1 coin is included for scale. Dimensions have been stated in mm.

manually shaken for 5 minutes. From the tube, 0.2 mL was pipetted into the observation chamber, which was placed under an Eclipse Ti inverted microscope (Nikon Corporation, Tokyo, Japan) with a CFI S Plan Fluor ELWD 20XC objective lens of 20× magnification and 0.45 numerical aperture. Attached to the microscope was an HPV-X2 high-speed camera (Shimadzu, Kyoto, Japan), operating at 10 million frames per second [94]. During camera recording, the materials were subjected to ultrasound pulses.

The pulses consisted of 20 cycles, each at a centre transmitting frequency of 1.0 MHz and a peak-negative pressure of 400 kPa, from a laboratory-assembled single-element transducer [93, 94]. The time between subsequent pulses was at least 1 minute. The signal fed into the transducer was generated by an AFG320 arbitrary function generator (Sony-Tektronix, Tokyo, Japan) and amplified by a UOD-WB-1000 wideband power amplifier (TOKIN Corporation, Miyagi, Japan).

A total number of 5800 images and 87 high-speed video sequences (each sequence consisted of 256 frames) were recorded during seven imaging sessions.

3.3 Results and discussion

Brightness-mode scans of the phantom wells are shown in Figure 3.2. Transient scattering was observed from individual spots inside the ink-filled well only (Figure 3.2a, left). After 9 minutes, no more scattering was observed (Figure 3.2b, left). This scattering can be attributed to the transient hydrophobic behaviour of carbon black, similar to the transient behaviour in an earlier study [60]. No scattering was observed in the saline-filled well. To observe this transient hydrophobicity at higher frame resolution, high-speed photography experiments were performed.

Figure 3.3 shows three frames of a representative example from the high-speed video

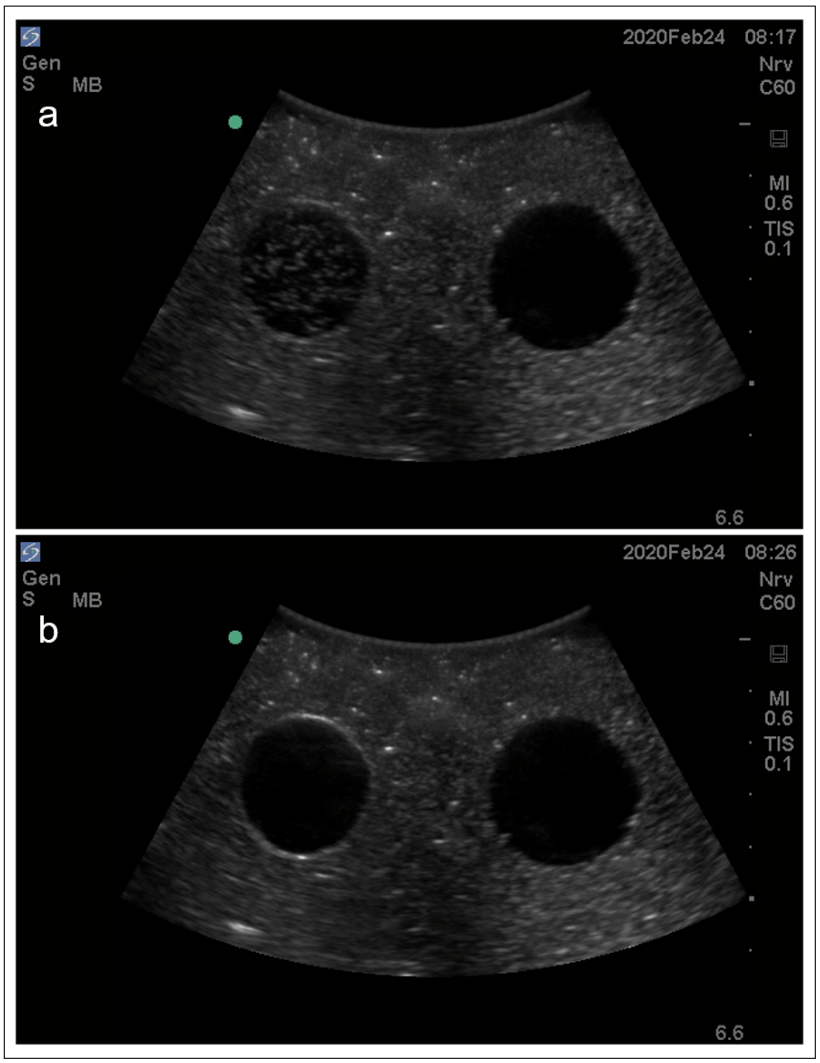


Figure 3.2: Phantom wells filled with black ink (left) and saline (right), directly after filling (a) and 9 minutes later (b). The green dot corresponds to the left-hand side of the probe. Each tick corresponds to 1.1 cm.

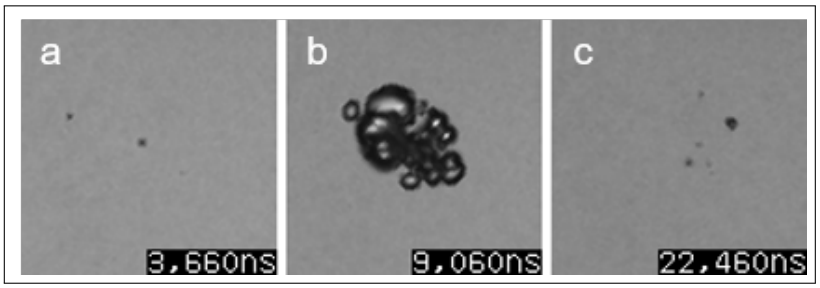


Figure 3.3: Zuper Black ink particles before (a), during (b), and after (c) sonication. Each frame corresponds to a $36 \times 36\,(\mu\mathrm{m})^2$ area. Time stamps, in nanoseconds, are in the lower right corners.

recordings of black ink. The frames show multiple ink particles before, during, and after 1.0-MHz sonication. During sonication, inertial cavities were seen to nucleate on the ink particles, after which cavity clusters were generated from interaction with other nucleations. During subsequent ultrasound pulses, the ink particles that had been involved in this nucleation cycle remained unaffected (not shown). This supports the observation from the brightness-mode scans.

3.4 Conclusions

Using brightness-mode sonography and high-speed photography, black tattoo ink was observed to transiently nucleate. Subsequent ultrasound bursts did not reactivate the ink. It is concluded that ultrasound changes the hydrophobicity of carbon black ink particles.

Acknowledgements

This work was supported by JSPS KAKENHI Grant Numbers 17H00864, 20H04542.

Chapter 4

Nucleation Threshold of Ink

This chapter is based on: C. S. Carlson, R. Matsumoto, K. Fushino, M. Shinzato, N. Kudo, and M. Postema, "Nucleation threshold of carbon black ultrasound contrast agent," *Japanese Journal of Applied Physics*, vol. 60, no. SDDA06, 2021.

The author conceptualised the work; analysed the data; and wrote the majority of the article.

Abstract

Most ultrasound contrast agents used in ultrasonic imaging comprise shell-encapsulated microbubbles, whose ingredients have been associated with adverse bioeffects. In this study, we investigated the nucleation behaviour of carbon black dispersion, whose hydrophobic nanoparticles are used intradermally. For a hypothetical, perfectly spherical carbon black particle surrounded by a perfectly spherical gaseous void, we derived a theoretical nucleation threshold of only 1.3× the resting radius. Carbon black particles and aggregates thereof were investigated using high-speed photography during 1.0-MHz sonication. The nucleation threshold found experimentally is lower than the Blake cavitation threshold of 2.0× the resting radius of free, unencapsulated microbubbles. Therefore, carbon black dispersion may be a promising ultrasound contrast agent.

4.1 Introduction

Ultrasound contrast agents typically comprise lipid- or albumin-encapsulated perfluorocarbon gas microbubbles [81, 95, 96]. They are injected during sonography with the main purposes of imaging perfusion processes and detecting tumours [97–101]. Using acoustic transmit amplitudes sufficiently high to generate asymmetric microbubble oscillations, the presence of microbubbles is subsequently detected by means of so-called harmonic imaging [63, 102, 103]. The encapsulating microbubbles shells and the perfluorocarbon gas ensure a prolonged lifespan of the microbubbles by several minutes to hours [104,105]. Without an encapsulating shell, a perfluorocarbon gas microbubble would dissolve in seconds, whilst a nitrogen microbubble would dissolve in milliseconds [106, 107].

The main disadvantage of said encapsulation materials is allergic reactions to them [108, 109]. Due to the prolonged lifespan of the microbubbles, caution should also be observed when subjecting people to sudden ambient pressure changes post contrast-agent administration, such as flying or scuba diving. Although the acoustic amplitudes required for harmonic imaging have been considered clinically safe, they may inadvertently generate harmonic response from surrounding tissue and associated unintended bioeffects [110–112]. Therefore, there has been an interest in ultrasound contrast agents that are safer in use than shell-encapsulated gas microbubbles and that express harmonics at lower acoustic amplitudes, *i.e.*, amplitudes that do not generate tissue harmonics.

Hydrophobic carbon black nanoparticles have demonstrated harmonic behaviour [70]. As the nucleation of carbon black nanoparticles is transient [60], we hypothesise that harmful cavitation-related aftereffects must be less prominent when using hydrophobic carbon black instead of a microbubble-based ultrasound contrast agent. However, most carbon nanoparticles are not desirable for *in-vivo* utilisation.

Carbon black pigment dispersion is allowed to be inserted through the skin by means of needles for cosmetic reasons — the inking of a tattoo [28]. In solid state, it comprises nanoparticles or nanoparticle aggregates with a mode diameter of $0.24\,\mu$m and a maximum diameter of $0.97\,\mu$m [113]. In solution, a hydrophobic particle takes up its own volume plus a surrounding void [82]. Consequently, in solution, the carbon black pigment dispersion nanoparticles or aggregates thereof were measured to have a mode diameter of $0.29\,\mu$m and a maximum diameter of $1.14\,\mu$m [113]. In carbon black dispersion, the gaseous void surrounding the hydrophobic solid nanoparticle takes up approximately 20% of the diameter [113]. The linear resonance frequencies of these

suspended nanoparticles were estimated to be greater than 15 MHz [113]. In a recent feasibility study, we found that carbon black pigment dispersion under sonication demonstrates transient nucleation [114]. In this follow-up study, we investigated the nucleation threshold of carbon black pigment dispersion nanoparticles both theoretically and experimentally.

4.2 Theory

Let us assume a perfectly spherical hydrophobic particle in suspension in an infinite liquid. Its resting radius including polytropic gaseous void is R_0, whilst its incompressible solid core radius is R_c. The instantaneous surface pressure p_s as a function of instantaneous radius R_i is equal to

$$p_\mathrm{s}(R_\mathrm{i}) = p_\mathrm{g}(R_\mathrm{i}) + p_\mathrm{v} - p_\mathrm{L} = \frac{2\sigma R_\mathrm{i}}{R_\mathrm{i}^2 - R_\mathrm{c}^2} \ , \tag{4.1}$$

where p_L the absolute pressure in the liquid at the bubble surface, p_g is the gas pressure inside the void, p_v is the vapour pressure inside the void, and σ is the surface tension at the void–liquid interface. If there is no disturbance in the liquid pressure, *i.e.*, if the particle is at rest, $p_\mathrm{L} = p_0$, in which p_0 is the ambient pressure, close to 1 atm.

Following the derivation of the cavitation threshold of a free bubble [81], if buoyancy and gas diffusion are slow with respect to a change in ambient pressure,

$$p_\mathrm{g}\, V^\gamma = \text{constant} \ , \tag{4.2}$$

where $V = \frac{4}{3}\pi\left(R_\mathrm{i}^3 - R_\mathrm{c}^3\right)$ is the instantaneous void volume and γ is the ratio of specific heats of the gas. For air, $\gamma = 1.4$ is a good approximation [81].

Substituting (4.1) for the gas pressures yields

$$\left(p_0 - p_\mathrm{v} + \frac{2\sigma R_0}{R_0^2 - R_\mathrm{c}^2}\right) V_0^\gamma = \left(p_\mathrm{L} - p_\mathrm{v} + \frac{2\sigma R_\mathrm{i}}{R_\mathrm{i}^2 - R_\mathrm{c}^2}\right) V^\gamma \ , \tag{4.3}$$

where $V_0 = \frac{4}{3}\pi\left(R_0^3 - R_\mathrm{c}^3\right)$ is the resting volume of the void. Rewriting V_0 and V in terms of R_i and reordering gives an expression of the absolute liquid pressure as a function of instantaneous void radius:

$$p_\mathrm{L}(R_\mathrm{i}) = \left(p_0 - p_\mathrm{v} + \frac{2\sigma R_0}{R_0^2 - R_\mathrm{c}^2}\right)\left(\frac{R_0^3 - R_\mathrm{c}^3}{R_\mathrm{i}^3 - R_\mathrm{c}^3}\right)^\gamma + p_\mathrm{v} - \frac{2\sigma R_\mathrm{i}}{R_\mathrm{i}^2 - R_\mathrm{c}^2} \ . \tag{4.4}$$

The function $p_\mathrm{L}(R_\mathrm{i})$ has a minimum in point (R_θ, p_θ). If the liquid pressure is lowered below the critical threshold pressure p_θ, corresponding to threshold radius R_θ, there is no equilibrium for (4.4), which results in explosive expansion of R_i.

For microbubbles, $R_\theta \approx 2.0\,R_0$, which is referred to as the Blake cavitation threshold [81]. A temporal pressure change $\Delta p(t) = [p_\mathrm{L}(t) - p_0]$ can be generated by an acoustic wave $\Delta p(t) = p_\mathrm{a}\sin(2\pi f t)$ of frequency f and pressure amplitude p_a. For the pressure change to be quasi-isostatic, f must be much less than the resonance frequencies of the suspended nanoparticles [81].

Using $\Delta p(t)$ as a driving function and following the derivation for an oscillating antibubble [115], the fundamental equation of spherical hydrophobic particle dynamics is found to be

$$R_\mathrm{i}\ddot{R}_\mathrm{i} + \frac{3}{2}\dot{R}_\mathrm{i}^{\,2} = \frac{1}{\rho}\left[\left(p_0 - p_\mathrm{v} + \frac{2\sigma R_0}{R_0^2 - R_\mathrm{c}^2}\right)\left(\frac{R_0^3 - R_\mathrm{c}^3}{R_\mathrm{i}^3 - R_\mathrm{c}^3}\right)^{\gamma} + p_\mathrm{v} - \frac{2\sigma R_\mathrm{i}}{R_\mathrm{i}^2 - R_\mathrm{c}^2} - p_0 - \Delta p(t)\right]. \tag{4.5}$$

Assuming a low driving amplitude, the linear resonance frequency f_r of a spherical hydrophobic particle follows to be

$$f_\mathrm{r} = \frac{1}{2\pi R_0\sqrt{\rho}}\sqrt{\frac{3\gamma\left(p_0 - p_\mathrm{v} + \frac{2\sigma R_0}{R_0^2 - R_\mathrm{c}^2}\right)}{1 - \left(\frac{R_\mathrm{c}}{R_0}\right)^3} - \frac{2\sigma R_0}{R_0^2 - R_\mathrm{c}^2}}\,, \tag{4.6}$$

which is similar to the linear resonance frequency of an unencapsulated antibubble [61]. The radial dynamics of antibubbles subjected to higher acoustic amplitudes have shown to be highly nonlinear [61]. Leaving out R_c from (4.6) gives us the linear resonance frequency of a free gas bubble for comparison.

4.3 Materials and methods

Solutions of (4.4) and (4.6) were computed using MATLAB® (The MathWorks, Inc., Natick, MA, USA). It was assumed that $p_0 = 1.0\,\mathrm{atm}$, $p_\mathrm{v} = 1.0\,\mathrm{kPa}$, $R_\mathrm{c} = 0.80\,R_0$, $\gamma = 1.4$, and $\sigma = 0.072\,\mathrm{N\,m^{-1}}$. From (4.6) it followed that a particle of outer diameter $2R_0 \leq 1.14\,\mu\mathrm{m}$ and core size $R_\mathrm{c} = 0.80\,R_0$ must have a linear resonance frequency $f_\mathrm{r} \geq 15\,\mathrm{MHz}$. This is more than double the frequency of a free gas bubble of equal size.

The experimental procedure was identical to the experimental procedure described in Ref. 60, except for the compound under investigation and the camera frame rates.

A quantity of $0.50\,\mu\mathrm{L}$ Zuper Black pigment dispersion (INTENZE Products, Inc., Rochelle Park, NJ, USA) was pipetted into a FALCON® 15 mL High-Clarity Polypropylene Conical Tube (Corning Science México S.A. de C.V., Reynosa, Tamaulipas,

Mexico), after which 5.0 mL of 049-16787 Distilled Water (FUJIFILM Wako Pure Chemical Corporation, Chuo-Ku, Osaka, Japan) was added. Tubes were either gently manually shaken for 5.0 minutes, or individually held for 1.0 minute in a 2510J-MT BRANSONIC® ULTRASONIC CLEANER (BRANSON ULTRASONICS CORPORATION, Danbury, CT, USA) filled with degassed water and operating at a transmitting frequency of 45 kHz. The sonically shaken tubes were used as controls.

From each tube, 0.2 mL was pipetted into the observation chamber of a high-speed observation system. [93] The observation chamber was placed under an Eclipse Ti inverted microscope (Nikon Corporation, Minato-ku, Tokyo, Japan) with a CFI S Plan Fluor ELWD 20XC objective lens of 20× magnification and 0.45 numerical aperture. Attached to the microscope was an HPV-X2 high-speed camera (Shimadzu, Nakagyo-ku, Kyoto, Japan), operating at frame rates equal to or greater than two million frames per second. [94] The maximum exposure time corresponded to 0.50 μs per frame. During camera recording, the material was subjected to ultrasound pulses.

A laboratory-assembled single-element transducer produced focussed ultrasound pulses [93, 94]. Each pulse had a centre frequency of 1.0 MHz. It is noted that 1.0 MHz$\ll$15 MHz, so the pressure changes in the liquid could be considered quasi-isostatic. The voltage amplitudes of the pulses were varied from 1 V to 5 V, with 1 V increments. In a running wave field, these voltages corresponded to peak-negative acoustic pressures between 0.20 MPa and 1.0 MPa, equivalent to mechanical indices between 0.20 and 1.0 [81]. To avoid a standing-wave situation, we only took the first eight ultrasonic cycles into account. The time between subsequent experiments was at least one minute. The signal fed into the transducer was generated by an AFG320 arbitrary function generator (Sony-Tektronix, Shinagawa-ku, Tokyo, Japan) and amplified by a UOD-WB-1000 wide-band power amplifier (TOKIN Corporation, Shiroishi, Miyagi, Japan).

A total number of 87 high-speed video sequences were recorded during five imaging sessions. Each video sequence consisted of 256 frames. The video sequences were stored on a personal computer and processed offline using the `onan.m` programme in MATLAB®. In the first frame of a sequence, the rectangular area of a particle i to be sized was selected manually, after which automated adaptive thresholding was used to measure the particle cross-section areas A_{ij} per frame j [116]. The particle radii R_{ij} as a function of time t_j were computed from $R_{ij}(t_j) = \sqrt{\frac{A_{ij}}{\pi}}$. Particles oscillating out of phase with respect to the incident sound field were classified as non-nucleating, whilst particles undergoing a phase shift during sonication were classified as nucleating.

4.4 Results and discussion

Figure 4.1 shows solutions of (4.4), expressed in Δp as a function of $R\,R_0^{-1}$.

The curves had been computed for the mode diameter $2R_0 = 0.29\,\mu$m with a solid core diameter $2R_c = 0.24\,\mu$m and for the largest diameter $2R_0 = 1.14\,\mu$m with a solid core diameter $2R_c = 0.97\,\mu$m. The minimum in each curve corresponds to a nucleation threshold $R_\theta\,R_0^{-1} = 1.3$. The corresponding threshold pressure change $\Delta p_\theta = p_\theta - p_0 = 0.88\,$MPa for suspended nanoparticles with the mode diameter and $\Delta p_\theta = 0.30\,$MPa for suspended nanoparticles with the maximum diameter.

These results indicate that carbon black pigment dispersion nanoparticles nucleate in acoustic regimes with amplitudes less than those required for microbubble nucleation.

Figure 4.2 shows representative $R(t)$ curves from a high-speed video recording of Zuper Black dispersion particles.

The frames were selected from the full video sequence, to illustrate particle sizes prior to sonication and during maximum rarefaction. Particles 1 and 2 were observed to nucleate during the third and fourth sonication cycle, respectively. Particle 1 had a maximum expansion of R_{max}=8×R_0 during its first nucleation cycle, whilst particle 2 had a maximum expansion of R_{max}=9×R_0 during its first nucleation sonication

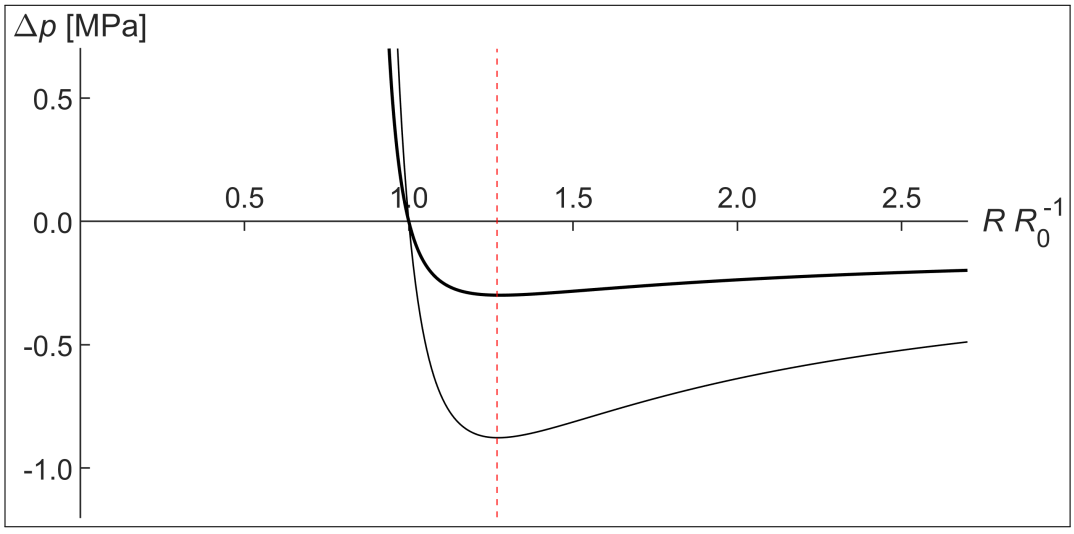


Figure 4.1: Quasi-isostatic liquid pressure change Δp as a function of $\left(R\,R_0^{-1}\right)$, computed for the mode particle diameter (—) and the largest particle diameter (—) of carbon black pigment dispersion. A red dashed line is drawn through the minima, for which $R_\theta\,R_0^{-1} = 1.3$ holds (– –).

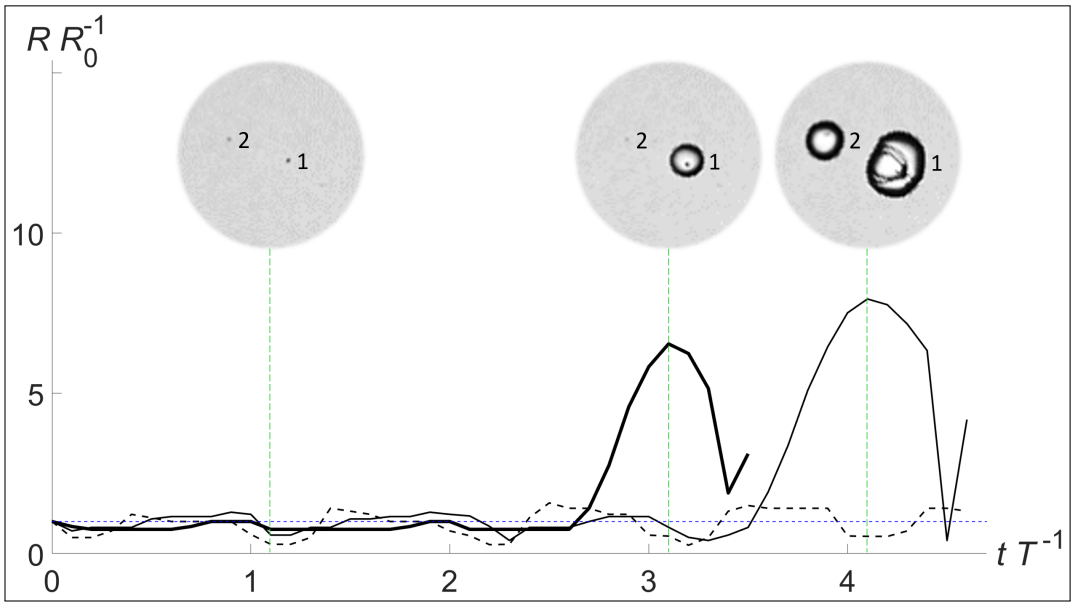


Figure 4.2: Curves of the radii R of three nucleating Zuper Black dispersion particles normalised by their respective resting radii R_0 as a function of time t normalised by period T, during a 20-cycle burst with a 2-V amplitude, with 36-μm-diameter inlays of high-speed video footage. Particles 1–3 are represented by bold (—), thin (—), and dashed (– –) lines, respectively. Particle 3 is not shown in the inlays. The stationary situation $R_{\max}R_0^{-1}$=1 is indicated by a blue dotted line (···).

cycle. Particle 3, not shown in the frames but represented by the dashed $R(t)$ curve, was observed to undergo volumetric oscillations with an expansion amplitude $R_{\max}$=1.6×R_0 during sonication, $\frac{1}{2}\pi$ out of phase with respect to the incident sound field, but without explosive growth. During subsequent ultrasound pulses, the ink particles that had been involved in this nucleation cycle remained unaffected (not shown).

Figure 4.3 shows a histogram maximum expansion results of Zuper Black dispersion particles under sonication, normalised by their resting radii.

For particles visibly undergoing explosive growth, the maximum expansion during the first nucleation cycle was taken for $R_{\max}$, whilst for the remaining particles, the greatest expansion over all oscillation cycles was taken. All but one particle not undergoing explosive growth had a maximum expansion $R_{\max} \leq 1.75R_0$. Although the exact nucleation threshold could not be determined, these results confirm that the nucleation threshold is lower than 2× the resting radius.

Only the manually suspended ink particles demonstrated nucleation activity, whereas not a single recording of ink suspended with the ultrasonic cleaner showed nucleation.

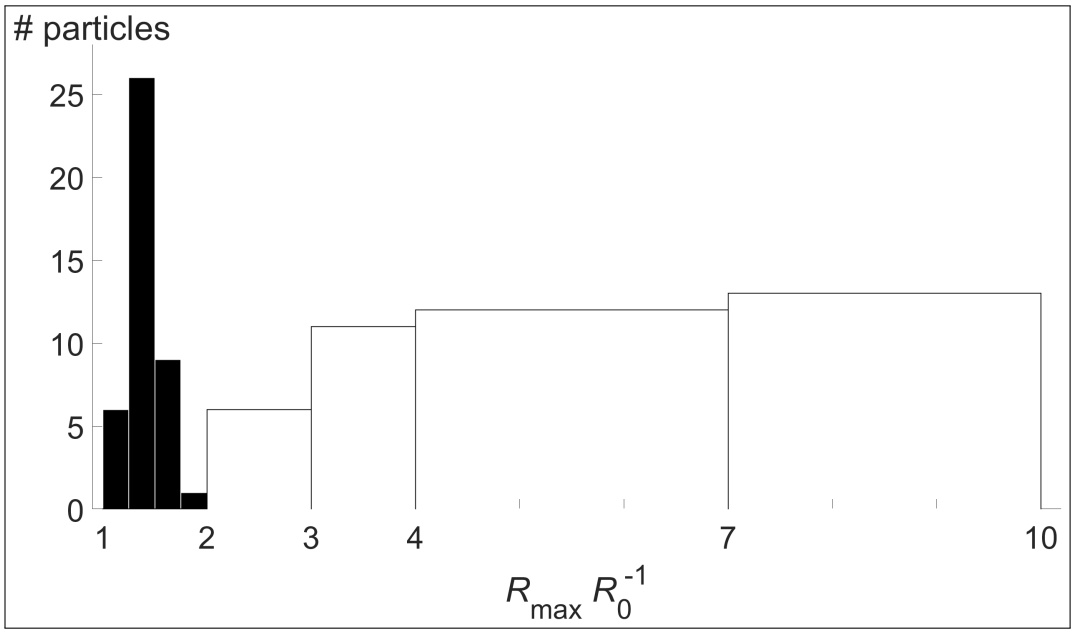


Figure 4.3: Histogram of maximum Zuper Black expansion normalised by particle resting radii. White bins represent particles that underwent explosive growth, black bins represent particles that did not undergo explosive growth.

These results agree with our observations of other hydrophobic particles [60].

4.5 Conclusions

Tattoo ink particles were observed to lose part their gaseous shells. Up to five subsequent ultrasound bursts were observed to reinitiate nucleation of the same particle at the same acoustic amplitude. Sonication at a higher acoustic amplitude was also observed to renucleate particles that had stopped nucleating in a lower-amplitude regime.

It is concluded that ultrasonic nucleation of carbon black pigment dispersion nanoparticles is a transient phenomenon. The theoretical nucleation threshold of a perfectly spherical particle surrounded by a perfectly spherical gaseous void is 1.3× the resting radius of the hydrophobic nanoparticle in suspension. This is lower than the Blake cavitation threshold of free, unencapsulated microbubbles.

Acknowledgements

This work was supported by JSPS KAKENHI, Grant Numbers JP17H00864 and JP20H04542, and by the National Research Foundation of South Africa, Grant Number 127102.

Chapter 5

Acoustic Analysis of Inked Tissues

This chapter is based on: C. S. Carlson, and M. Postema, "Deep impact of superficial skin inking: acoustic analysis of underlying tissue," *BIO Integration*, vol. 2, 2021.

The author conceptualised the work; performed the experiments; analysed the data; and wrote the majority of the article.

Abstract

Skin tattoos are a common decoration, but profound scientific study whether the presence of a skin tattoo alters the acoustic response from superficial and therefore from underlying tissue was previously lacking. Any image aberrations caused by tattoo presence may have been thought negligible, yet empirically found artefacts in brightness-mode images of tattooed skin suggest otherwise. This study investigated the nature of these artefacts theoretically and experimentally in extremely simplified cases of perfectly flat and homogenous layered media and in tattooed pork. Theory was derived for computing the acoustic response from horizontally and vertically layered media containing a thin inked layer. Experiments were performed *in vitro*. Artificial and pork skin were tattooed, attached to phantom material, and sonicated with a 13–6-MHz probe. The speed of sound of these materials was determined, and the perceived refraction angles measured. The measured speeds of sound of tattooed materials were higher than those of their uninked counterparts. The presence of tattoo ink was found to have increased the linear acoustic attenuation by $1\,\mathrm{dB\,cm^{-1}}$. This value is negligible for typical tattoos of only few millimetres. The perceived critical refraction angles of adjacent materials could be detected and their corresponding speeds of sound were quantified. These coincided with values derived from theory.

The ratio in speeds of sound of adjacent materials was shown to create distinct highlights in brightness-mode images. The artefacts observed in *in-vitro* and *in-vivo* brightness-mode scans were explained from near-vertical transitions between areas of different sound speed. This is the first study correlating so-called critical refraction highlighting with speed-of-sound information. In addition, it was found that phantom material is a room-temperature acoustic alternative for experiments on live human skin. In summary, the presence of superficial tattoos has a small but quantifiable effect on the acoustic response from deeper tissues.

5.1 Introduction

Ultrasonic imaging is used for real-time medical diagnosis of internal organs and for guided delivery of therapeutics to those organs [117–120]. Although skin tattoos are a widespread and common form of permanent visible decoration, they are very rarely associated with ultrasonic imaging. In fact, with the exception of a recent *in-vivo* study at 13–24 MHz sonication [121], subjecting inked skin to ultrasound has exclusively been performed for monitoring of dermatological tattoo complications [67, 68] and for tattoo removal [46, 48]. Ultrasonic imaging of so-called carbon-marked organ tissue is more common, however [122, 123].

To date, it has not been investigated whether the presence of a skin tattoo alters the acoustic response from deeper underlying tissue. In this study, we theoretically and experimentally quantify these potential alterations. This is a relevant research topic, as novel medical treatment methods rely on quantitative data from ultrasonic images of deep tissue [124, 125]. It might be thought that ultrasonic tattoo removal requires profound knowledge on the interaction of ultrasound with inked skin. However, ultrasonic tattoo removal methods utilise high-intensity focussed ultrasound [48], which heats up tissue structures [126], irrespective of tattoo presence. Here, we focus on the effects following interaction of ultrasound with tattoo ink particles themselves. It could be hypothesised however that the absorption of low-amplitude ultrasound by tattoo ink might lead to its disintegration.

Previous acoustic studies of hydrophobic carbon particles demonstrated nucleation at low acoustic amplitudes, but this phenomenon was found to be transient [60, 114]. As a follow-up, undiluted black tattoo ink was subjected to ultrasound *in vitro*. Its linear acoustic attenuation coefficient was measured to be $0.15 \pm 0.01\,\mathrm{dB\,cm^{-1}\,MHz^{-1}}$ and its speed of sound in steady, non-nucleating state to be $1639\,\mathrm{m\,s^{-1}}$ [113]. Since human tissue has an average linear acoustic attenuation coefficient of $0.3\,\mathrm{dB\,cm^{-1}\,MHz^{-1}}$

and a speed of sound of $1540\,\mathrm{m\,s^{-1}}$ [86], one might hypothesise that the visible presence of pigment dispersion in the skin alters the pressure amplitudes of the ultrasound propagating through it. It has therefore been suggested that tattoo ink might act as a, very superficial, ultrasound contrast agent [127]. Yet, in tattooed tissue, the inked layer is only a few millimetres thick, reducing potential scattering and attenuation effects. Furthermore, the acoustic parameters of undiluted ink *in vitro* may not apply to the diluted situation *in vivo*.

Nevertheless, the hypothesis that the presence of a superficial tattoo results in visible artefacts in brightness-mode ultrasound images has been infused by sporadic *in-vivo* observations. Such observations are shown in Figure 5.1, which depicts scans of a dorsal tattoo. A highlighted region of increased scattering amplitudes from tissue transitions can be observed in both scans, originating from the separations of inked and uninked skin and directed at respective angles of 13° and 14° with respect to the normal, on the side corresponding to the uninked part.

Such observations are rare indeed, yet this study investigates the nature of these aberrations theoretically and experimentally, for the extremely simplified cases of perfectly flat and homogenous layered media and for tattooed pork. The media of choice in this study have been embedding in tissue-mimicking phantoms. Phantoms are common in various medical imaging modalities including ultrasound [128], but sonography of tissue materials embedded in tissue-mimicking phantoms, although most certainly not novel, has not been reported.

5.2 Theory

Quantitative ultrasonic imaging is typically using stochastic methods and analysis of backscattering spectral data from brightness-mode images [129–133]. In this study, we investigate absolute amplitudes from lines in such images, quite similar to early experimental work [134].

5.2.1 Orthogonal incidence

Let us assume a layered tissue-mimicking system with perfectly flat interfaces, separating media of different acoustic impedances. Let us also assume an ultrasound field, generated and recorded by a clinical ultrasound system, whose angle of incidence coincides with the normal of the interfaces, which means that an incident ultrasound

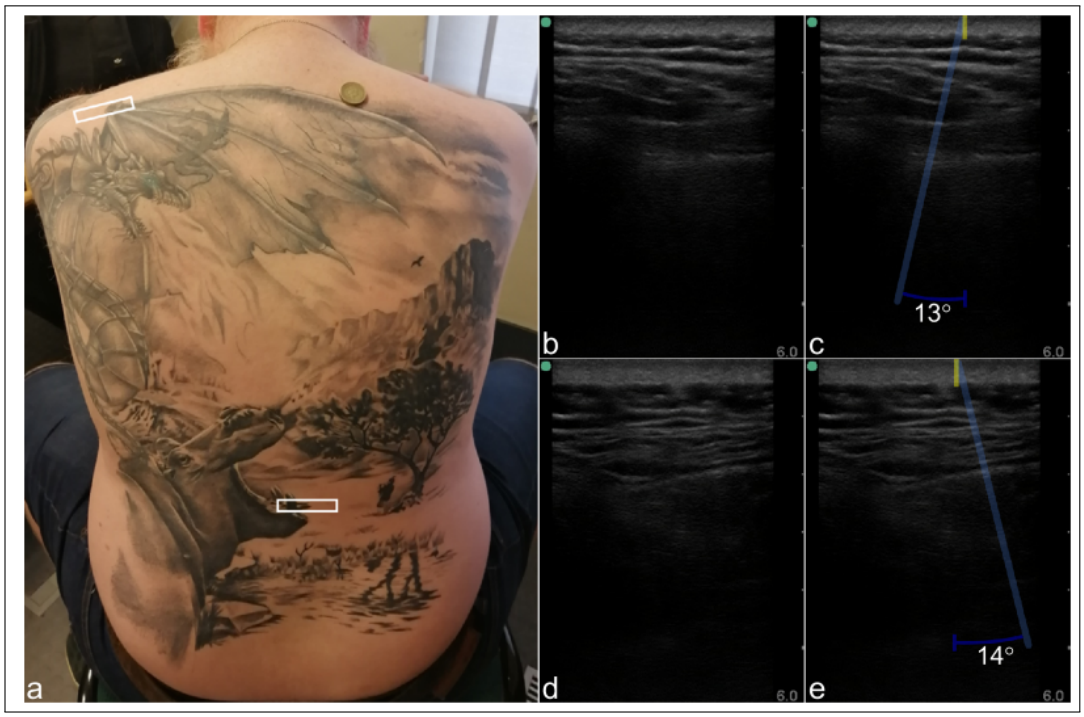


Figure 5.1: Dorsal tattoo comprising carbon black and titanium white pigments (a); the areas of the two rectangular half-inked regions of interest have been marked in white. Brightness-mode image of the region of interest on the left shoulder (b); the separation between inked and uninked skin is indicated by a yellow line and a zone of increased scattering amplitudes is indicated by an opaque blue trapezoid (c). Brightness-mode image of the region of interest on the lower back (d); the separation between inked and uninked skin is indicated by a yellow line and a zone of increased scattering amplitudes is indicated by an opaque blue trapezoid (e). Frames b–e have been horizontally flipped such that the left-hand-side of the scan corresponds to the inked left-hand-side of the region of interest. The probe was held by the same sonographer during scanning.

beam is orthogonal with respect to an interface plane itself. The ultrasound system converts two-way travel times to one-way radial distances presuming a constant speed of sound through tissue c_{t}. The one-way distances computed are henceforth referred to as perceived distances.

Taking into account the true tissue attenuation and the attenuation presumed by the system [86], and taking into account the dual transmission through interface i and the reflection on both respective interfaces [81], one must then find the ratio of absolute backscattered acoustic amplitudes from two adjacent interfaces i and $i+1$

to be

$$\frac{B_{i+1}}{B_i} = \left(1-R_i^2\right) \frac{|R_{i+1}|}{|R_i|} \, e^{\,2\,\alpha_\mathrm{t}\left(r'_{i+1}-r'_i\right) f_\mathrm{c}} \, e^{-2\,\alpha_i\,d_i\,f_\mathrm{c}}, \tag{5.1}$$

where B_i is the peak in the signal recorded from the proximal interface, B_{i+1} is the peak in the signal recorded from the distal interface, d_i is the true thickness of the medium between the proximal and distal interfaces, f_c is the centre frequency of the ultrasound pulse, R_i is the reflection coefficient of the proximal interface, R_{i+1} is the reflection coefficient of the distal interface, r'_i is the perceived axial distance from an arbitrary origin O to the proximal interface, r'_{i+1} is the perceived axial distance from the same origin O to the distal interface, α_i is the acoustic attenuation coefficient of the medium between the proximal and distal interfaces, and α_t is the average attenuation coefficient in soft tissue [72]. Throughout this study, it has been assumed that d_i is greater than the longest wavelength of the ultrasound pulse. It should be noted that the units of attenuation coefficients can be converted from $[\mathrm{Np\,m^{-1}\,MHz^{-1}}]$ to $[\mathrm{dB\,cm^{-1}\,MHz^{-1}}]$ by multiplication by a factor $2000\log_{10} e$. A graphical representation of the parameters in equation (5.1) is shown in Figure 5.2. The reflection coefficients are defined by

$$R_i = \frac{Z_i - Z_{i-1}}{Z_i + Z_{i-1}} = \frac{\rho_i c_i - \rho_{i-1} c_{i-1}}{\rho_i c_i + \rho_{i-1} c_{i-1}} \tag{5.2}$$

and

$$R_{i+1} = \frac{Z_{i+1} - Z_i}{Z_{i+1} + Z_i} = \frac{\rho_{i+1} c_{i+1} - \rho_i c_i}{\rho_{i+1} c_{i+1} + \rho_i c_i}, \tag{5.3}$$

where c_{i-1}, c_i, and c_{i+1} are the respective speeds of sound in media $i-1$, i, and $i+1$; ρ_{i-1}, ρ_i, and ρ_{i+1} are the respective densities of the media; Z_{i-1}, Z_i, and Z_{i+1} are the respective acoustic impedances of the media [81].

The unknown speed of sound of medium i of known thickness d_i is found from its relation to the presumed speed of sound through tissue by using

$$c_i = \frac{d_i}{r'_{i+1} - r'_i}\, c_\mathrm{t}. \tag{5.4}$$

It must be noted that no prior knowledge of any medium proximal to medium $i-1$ is required. Equations (5.1)–(5.4) hold for any layered backscattering entity, including artificial, living, dead, and even so-called undead [135] tissues. However, without prior knowledge of media $i-1$, i, and $i+1$ themselves, the linear attenuation coefficient cannot be extracted from (5.1), as the damping contribution from transmission and reflection cannot be quantified. Furthermore, the accuracy of computations using (5.1) relies on the precision of determining B_i and B_{i+1}. If we only focus on a change in tissue properties, instead of on the tissue properties themselves, we can circumvent this issue and reduce the number of parameters as follows. The

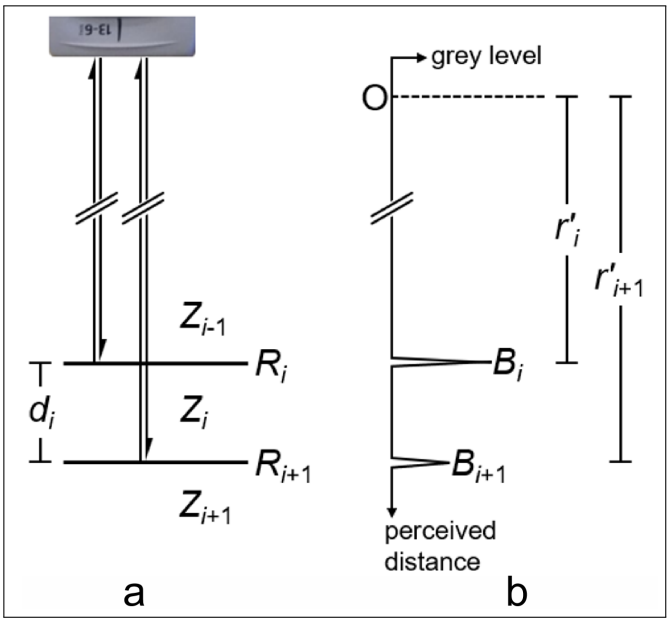


Figure 5.2: Graphical representation of the parameters in equation (5.1). The physical situation (a) results in an axial trace recording (b).

introduction of a small amount of foreign material, such as tattoo ink, in a thin medium i could slightly alter the speed of sound in the medium, causing the perceived distance from any distal interface or scatterer to shift even less slightly. However, the introduction of a foreign material should then also alter the acoustic attenuation of the medium, its density and, consequently, the reflection coefficients of both adjacent interfaces, resulting in an alteration in the scattered amplitude from any distal interface or scatterer. Now let us consider a scatterer j at an unknown but fixed distance beyond interface $i+1$, whose scattering amplitude is U_j if the medium i proximal to the scatterer is unaltered, but A_j if the medium is altered. Then, the ratio of scattered amplitudes of the scatterer under these two conditions is

$$\frac{A_j}{U_j} = \frac{\left(1-R_{i,\mathrm{A}}^2\right)\left(1-R_{i+1,\mathrm{A}}^2\right)}{\left(1-R_{i,\mathrm{U}}^2\right)\left(1-R_{i+1,\mathrm{U}}^2\right)}\, e^{-2(\alpha_\mathrm{A}-\alpha_\mathrm{U})d_i f_\mathrm{c}}, \tag{5.5}$$

where the subscript A denotes altered and the subscript U denotes unaltered. A graphical representation of the parameters in equation (5.5) is shown in Figure 5.3.

If prior information is known about the acoustic impedances of proximal media, the difference in attenuation of altered and unaltered media can be computed from distal scattering data, using equation (5.5). If no prior information is known about the acoustic impedances of proximal media, the total damping contribution equation (5.5) yields the total damping contribution. Thus, the influence of ink presence is expressed by one parameter only. As a side note, in fluid media with low concentrations of

materials of interest, but also in phantom materials, the contribution by the reflection coefficients has often been neglected [136–139].

5.2.2 Parallel incidence

Let us assume a layered tissue-mimicking system with perfectly flat interfaces, separating media of different speeds of sound. Let us also assume an ultrasound field, generated and recorded by a clinical ultrasound system, whose angle of incidence is parallel to the planes of the interfaces.

Let us consider one interface, separating two numbered media i and $i+1$ with respective speeds of sound of c_i and c_{i+1}. We choose our coordinate system such that $c_i < c_{i+1}$.

From Snell's law it follows that at the interface a wave front is generated with a

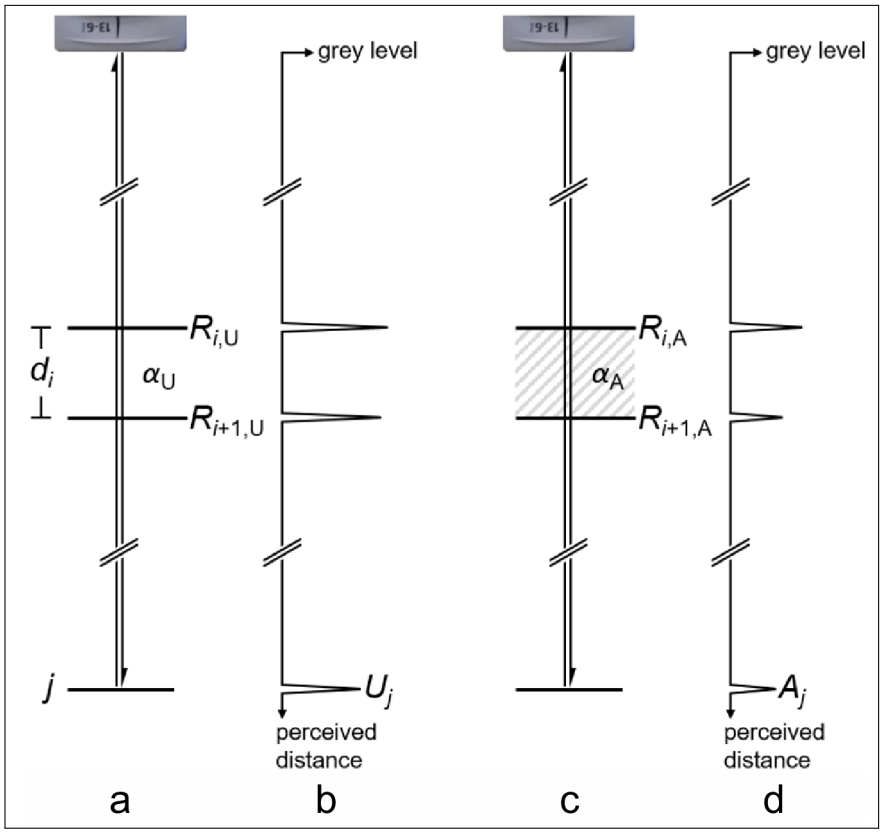


Figure 5.3: Graphical representation of the parameters in equation (5.5). The physical situations (a, c) result in axial trace recordings (b, d).

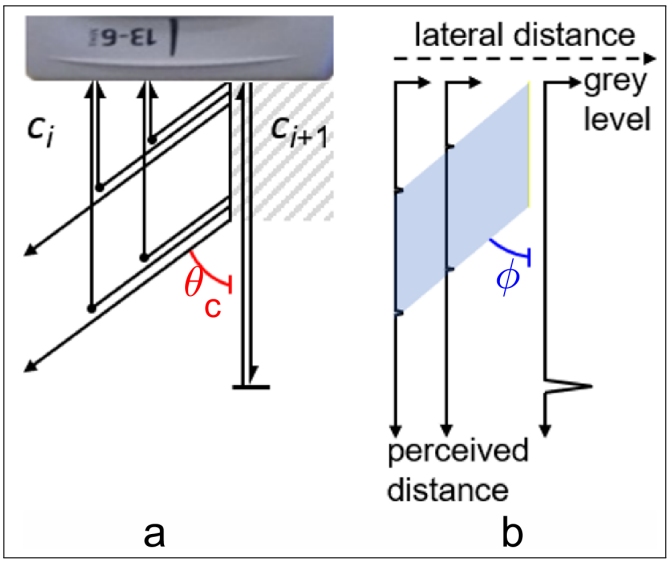


Figure 5.4: Graphical representation of the parameters in equations (5.6) and (5.7). The physical situation (a) results in axial trace recordings (b).

critical refraction angle θ_c with respect to the incident sound field, for which

$$\cos\theta_c = \frac{c_i}{c_{i+1}} \tag{5.6}$$

holds [81]. The scattering signals from this wave front in the direction of the probe surface are superimposed on backscattering from remote scatterers. Once the time-signal received by a transducer element has been converted to one-way axial distance with respect to the receiving element and the signal amplitudes have been plotted as bright points in a brightness-mode image, the points appear to be visibly connected as if they form a highlighted trapezoid. The highlighted trapezoid has a perceived angle ϕ_c with respect to the normal

$$\phi_c = \arctan\frac{2c_i}{c_t}\left(\frac{1}{\sin\theta_c}+\frac{1}{\tan\theta_c}\right)^{-1} = \arctan\frac{2c_i}{c_t}\sqrt{\frac{c_{i+1}-c_i}{c_{i+1}+c_i}}\,, \tag{5.7}$$

which has been derived from (5.6) under the assumption that the horizontal and vertical pixel sizes of the brightness-mode image are equal. A graphical representation of the parameters in equations (5.6) and (5.7) is shown in Figure 5.4.

With the reasoning above, the ratio of the speeds of sound of two adjacent media can be derived from an ultrasound image, using only (5.7). We refer to the phenomenon of perceived high scattering zones under an angle in brightness-mode images as critical refraction highlighting.

In case of a finite thickness of the layer with speed of sound c_i, the critically refracted

wave front re-refracts according to

$$\sin\theta_{\mathrm{r}} = \frac{c_{i+1}}{c_i}\sin\theta_{\mathrm{c}} = \frac{1}{c_i}\sqrt{c_{i+1}^2 - c_i^2}, \tag{5.8}$$

where θ_{r} is the re-refracted angle with respect to the normal. Similarly to the derivation of (5.7), a perceived angle ϕ_{r} of the resulting trapezoid below the interface is found to be

$$\phi_{\mathrm{r}} = \arctan\frac{2c_{i+1}}{c_{\mathrm{t}}}\sin\theta_{\mathrm{r}} = \arctan\frac{2c_{i+1}}{c_{\mathrm{t}}\,c_i}\sqrt{c_{i+1}^2 - c_i^2}\ . \tag{5.9}$$

In short, the speed of sound of inked tissue follows directly from the perceived re-refracted angle for any known tissue.

5.3 Materials and methods

5.3.1 Preparation of tissue samples

Practice skin–Silicone (yellow) 30×20 cm (Body Graphics Tattoo Supply, Douglasdale, Johannesburg, South Africa) with a 3.04-mm measured thickness was used for representing skin-mimicking material and a 1.104-kg piece of pork belly (FOOD LOVER'S MARKET, Brackenfell, South Africa) was used for representing skin and underlying tissue.

A TM-148 Iron Shader Tattoo Machine with a 1211F Standard Flat Needle in an 11F Black Disposable Tattoo Tube With Silica Gel Black Tattoo Grip (Yuelong Tattoo Supply, Yiwu, Zhejang, China) was used to tattoo our tissue materials with Zuper Black pigment dispersion (INTENZE Products, Inc., Rochelle Park, NJ, USA) until they were visibly covered. The needle was oscillating at a frequency of 100 Hz. Its penetration depth was set to 2 mm. The ink had a density of 1313 $\mathrm{kg\,m^{-3}}$ [113].

Sheets of artificial skin were cut into 95×65-$\mathrm{mm^2}$ pieces. These were tattooed with black ink or left untreated for controls. The untreated artificial skin was measured to have a density of 1087 $\mathrm{kg\,m^{-3}}$, the inked artificial skin was measured to have a density of 1097 $\mathrm{kg\,m^{-3}}$. For comparison, human epidermis has a density of 1110–1190 $\mathrm{kg\,m^{-3}}$ [72]. The difference in thickness between inked and uninked artificial skin was reasoned to be 0.02 mm.

A 20-mm wide strip of the pork skin was tattooed with black ink. The area next to this strip was dry-needled, *i.e.*, tattooed without ink, so as to ensure the same skin surface as the inked part. After tattooing, the pork belly was cut into an

approximately 70×45×35-mm^3 cuboid, such that the 20-mm-wide black shaded tattoo ran through the centre of the skin surface.

5.3.2 Preparation of phantoms

Five tissue-mimicking gelatine phantoms were manufactured, one of which contained a pork belly sample. For the phantom gelatine preparation, the method described by Bude and Adler was followed [91]. Boiled tap water was allowed to cool down to 80°C before ingredients were added. Per litre water, a mixture of 80 g Sheridans^{TM} Clear & Unflavoured EDIBLE GELATINE (Libstar Operations (Pty) Ltd., Dunkeld, Johannesburg, South Africa) and 40 g PSYLLIUM HUSK POWDER (Nature's Choice, Highbury, Randvaal, South Africa) was gradually added under continuous stirring, resulting in a homogenous hydrogel.

Each phantom was produced in two steps. For the first step, 50 ml of hydrogel was poured into an HPL806 mould (LocknLock CO., LTD., Seochu-gu, Seoul, Korea). For a phantom with tissue, the tissue sample had been placed inversely on the bottom of the mould. For a control phantom, a 27.75-mm-diameter glass 7621 20ml VIAL 22/400 (WEST PACK LIFESTYLE, Kya Sands, Johannesburg, South Africa) or a 17.80×7.80×48.00-mm^3 acrylonitrile butadiene styrene 4211075/2451 cuboid (LEGO System A/S, Billund, Denmark) had been placed on the bottom of the mould. The partly-filled mould was subsequently cooled at 6°C for 30 minutes.

For the second step, hydrogel was poured onto the partially set phantom. The filled mould was subsequently cooled at 6°C for 8 hours. For the control phantoms, the embedded objects were gently removed, leaving either a cylindrical or a cuboid well to be filled with distilled water for calibration purposes.

At room temperature, the resulting phantoms measured 112×79×40 mm^3 each. The density of the phantom material was measured to be 1025 kg m^{-3}.

5.3.3 Experimental procedure

A photograph of the experimental setup in operation is shown in Figure 5.5.

A container of inner dimensions 580×235×65 mm^3, custom-made from 5-mm PLEXIGLAS® plates (Röhm GmbH & Co. KG, Darmstadt, Germany), was filled with degassed Distilled Water (CJ Distribution, Glen Austin, Midrand, South Africa).

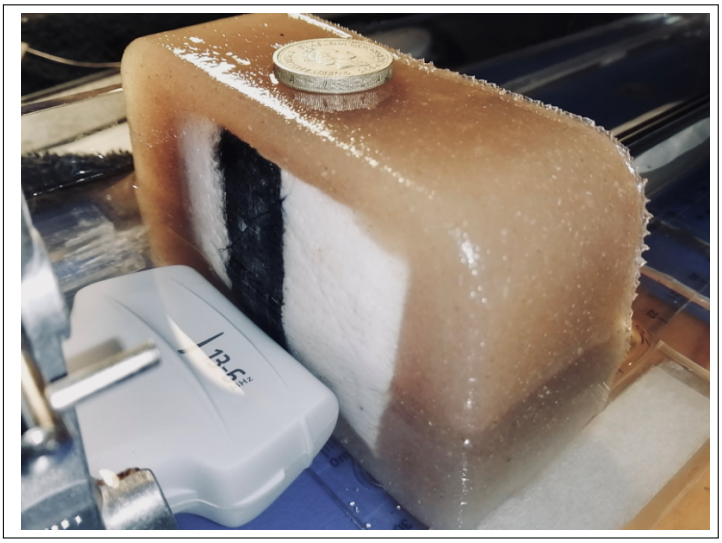


Figure 5.5: Experimental setup of the probe sonicating tattooed pork embedded in a tissue-mimicking phantom. According to practice [140], a St Helena £1 coin with a diameter of 23.44-mm and thickness of 2.80-mm, has been added for scale and for three-dimensional perspective. The dimensions of the phantom were $112 \times 79 \times 40\,\mathrm{mm}^3$.

An HFL38x 13–6-MHz linear probe of a SonoSite® M-Turbo® sonography device (FUJIFILM SonoSite, Inc., Bothell, WA, USA) was clamped in the length direction of the container such that the probe was underwater. There was no human interaction with the probe during the experiments.

The first side lobe of this probe has a maximum at approximately 20° with respect to the transmission axis at its centre frequency [141]. An HGL-0200 S/N 1269 hydrophone (Onda Corporation, Sunnyvale, CA, USA) was placed on a 17-mm-high glass plateau such that the hydrophone was inline with and directed towards the centre element of the probe, at an axial distance of 50 mm with respect to the probe surface.

All objects to be investigated were individually scanned. All dimensions were callipered before and after scanning.

A tissue-mimicking phantom was positioned centrally on the bottom plane of the container, tilted such that the plane containing tissue was facing the probe surface. The probe position was not adjusted, assuring constant axial distance, azimuth, and elevation of the probe with respect to the phantom throughout the experiments.

The ultrasound system was operating in either intima-media thickness (IMT) or

musculoskeletal (MSK) pulsed brightness mode. IMT mode was used when the tissue of interest was at an axial distance of less than 3.0 cm and MSK mode was used when the tissue of interest was at an axial distance greater than 3.0 cm. A single pulse comprised a chirp with frequencies of the broad bandwidth 6–13 MHz. The pulse repetition frequency was 2.5 kHz. When using control phantoms, tissue samples were positioned on the proximal side of the phantom during sonication. For controls, the tissue samples were gently removed, leaving a gap filled with distilled water between the probe and the phantom. The penetration depth of the ultrasound was set to 6.0 cm relative to the probe surface. Ultrasound pulses were indicated by the system to have a mechanical index of 0.6 and a thermal index of 0.1 [142].

5.3.4 Image processing

A total number of 337 brightness-mode video clips and 450 brightness-mode still-frames was recorded using the ultrasound scanner internal storage, yielding a total number greater than 15 000 brightness-mode images.

Image adjustment settings were not changed throughout the experiments. The ultrasound system was assumed to have converted two-way travel times to one-way radial distances using c_t=1540 m s^{-1} for the speed of sound in tissue and to have compensated for tissue attenuation by amplifying the backscattered signal by 0.3 dB cm^{-1}MHz^{-1}.

Image processing was done using MATLAB® (The MathWorks, Inc., Natick, MA, USA). In all images recorded, the axial backscattering profiles were extracted on an 8-bit grey scale, after which the absolute peak scatter amplitudes, corresponding to the respective interfaces and individual strong scatterers, and their respective perceived distances were identified.

In addition, critical refraction angles were measured manually from selected images with clear tissue transitions. The precision of measurement was 1°.

The influence of reflections and attenuation on the acoustic amplitudes was computed using (5.5) for single distal scatterers. The speed of sound of each medium was computed from the perceived distances between peak scattering amplitudes using (5.4) or from the perceived highlighted angle between two media using (5.7).

Table 5.1: Measured values of the speed of sound compared with literature values.

Material	Measured c [$\mathrm{m\,s^{-1}}$]	Compared with	Literature c [$\mathrm{m\,s^{-1}}$]	
Phantom	1537±10	Human skin	1537	[143]
Artificial skin	1043±17	Silicone rubber	959–1113	[144]
Artificial skin, tattooed	1067±18	Silicone rubber	959–1113	[144]
Pork skin, dry-needled	1508±2	Pig skin	1503	[145]
Pork skin, tattooed	1509±3	Pig skin	1503	[145]

5.4 Results and discussion

Table 5.1 shows an overview of the measured values of the speed of sound of the materials investigated. For comparison, literature values were included of media similar to those investigated.

The phantom material had a speed of sound at room temperature equal to that of human skin at body temperature [143].

The speed of sound in inked artificial skin was greater than in uninked skin, but the error bars overlapped. Both values are in the range found in literature for its primary component [144]. Despite the near-matching density of artificial skin, its speed of sound is not representative for human skin at all.

In pork skin, no significant difference in the speed of sound was measured between the inked and the uninked skin, based on 640 brightness-mode images. The mean value pork skin at room temperature of $1508\pm2\,\mathrm{m\,s^{-1}}$ is close to the literature value of pig skin at body temperature of $1503\,\mathrm{m\,s^{-1}}$ [145]. It has been reported that storage increases the speed of sound of meat over time [145], which might account for the minor difference.

Figure 5.6 shows an example of brightness-mode images of artificial skin positioned between the ultrasound probe and a control phantom with a cuboid space filled with distilled water. From the axial greyscale profile of unaltered skin, the peak backscattered value U_1 representing the phantom–water interface and U_2 representing the water–phantom interface were found to be 75 and 126, respectively. From the axial greyscale profile of tattooed skin, the peak backscattered value A_1 representing the phantom–water interface and A_2 representing the water–phantom interface were found to be 70 and 120, respectively.

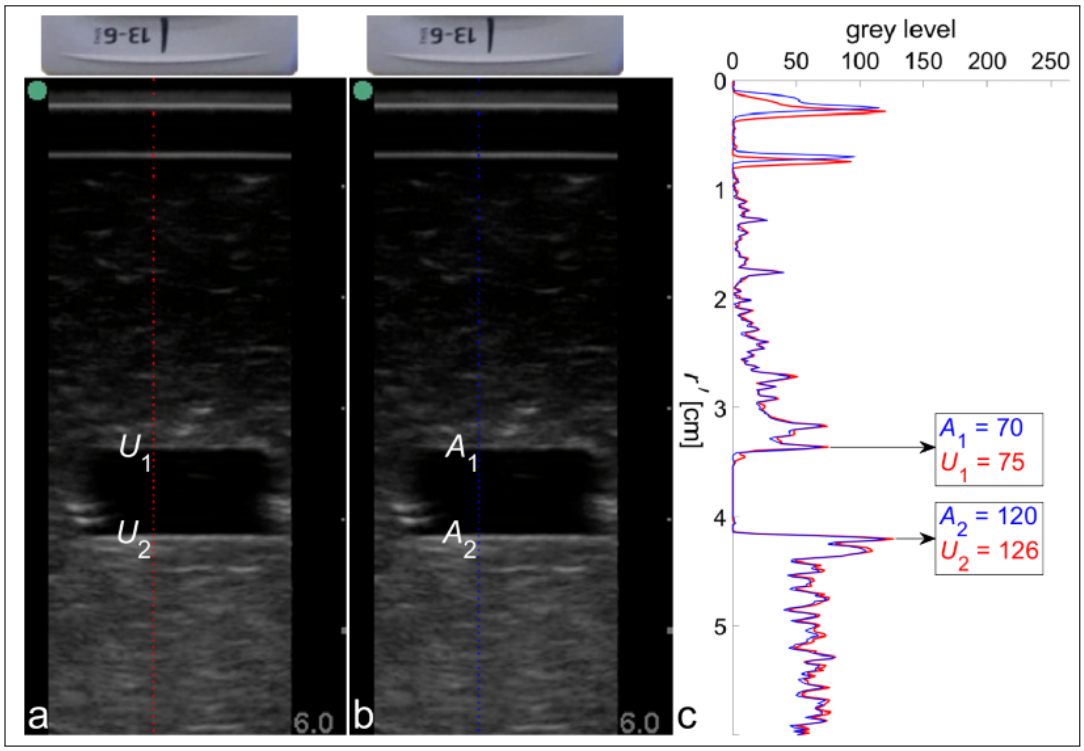


Figure 5.6: Brightness-mode scans of artificial skin, unaltered (a) and altered by tattooing (b), positioned proximal to phantom material and their respective axial greyscale profiles (c).

Knowing the respective reflection coefficients, the difference in attenuation between inked and unaltered skin followed from equation (5.5), which had been applied to 1 206 brightness-mode images. Using the backscattering amplitude from either interface, the 1-dB cm^{-1} difference caused by the presence of tattoo ink is negligible knowing that the thickness of the tattooed layer is only a few millimetres. This finding would also suggest that ultrasonic tattoo removal at low acoustic amplitudes is not feasible in the frequency range investigated, whilst noting that this is beyond the scope of the present study.

A few representative examples of critical refraction highlighting are demonstrated in Figures 5.7 and 5.8. These serve to illustrate theory and practical limitations.

Figure 5.7 shows four representative proofs-of-principle scans of pork belly adjacent to phantom material, from a subset of 468 brightness-mode images. The perceived angles of the multiple highlighted regions were seen to vary between 10° and 21°. Taking into account the error margins of both materials, we computed angles for the ratio of the speeds of sound of phantom and pork skin between 9° and 14°. However, if we also include the speed of sound of pig fat, 1426 $\mathrm{m\,s}^{-1}$, in (5.7), the greatest

theoretical angle is 24°. Consequently, our measurements on pork belly fell inside the theoretical margin. This control experiment showed that regions were highlighted in brightness-mode images if adjacent materials have a different speed of sound.

Figure 5.8 shows another four representative scans of embedded pork, but this time of the transition between inked and uninked skin, from a subset of 394 brightness-mode images. Here, the perceived angles deviated from the normal by 6° or less. Taking into account the standard deviation of the speed of sound of pork skin (*cf.* Table 5.1), which had been measured from 640 brightness-mode images, the perceived angle should lie between 2° and 5°. Although the highlighted areas confirm theory, determining the angles is too subjective to draw firm conclusions.

Revisiting Figure 5.1, presuming a speed of sound of $1537\,\mathrm{m\,s^{-1}}$ in the uninked skin of the subject and a critical refraction angle of 13°–14°, equation (5.7) yields a speed of sound of the inked skin of $1579\text{–}1586\,\mathrm{m\,s^{-1}}$, suggesting a high ink concentration. This speed of sound difference between inked and uninked skin cannot be observed from the dermis thicknesses, as the perceived difference in thickness of the approximately 2-mm tattooed layer would be only 0.06 mm. Furthermore, it is noted that in this case a 1° measurement difference in the critical refraction angle leads to a rather insignificant difference in sound speed of $7\,\mathrm{m\,s^{-1}}$.

Although critical refraction highlighting has shown plausible speed-of-sound ratios in the simplified situations presented in this study, an inherent flaw is the measurement error in the perceived angle. By defining scattering brightness criteria and automating the highlighted region selection and measurement, the precision might be improved.

Our interest was primarily focussed on subsurface acoustic effects resulting from superficial skin tattoos, but critical refraction highlighting might be applied in fields where the detection of vertically layered media with high speed-of-sound differences is crucial. These might include the identification of near-surface tissue types, the nondestructive detection of construction flaws, and even the detection and identification of geological trap constructions.

The ultrasound frequencies generated by the probe used in this study were high enough to detect tissue transitions but low enough to avoid scattering from skin inhomogeneities. As the purpose of this study was to quantify acoustic effects of superficial skin inking on deeper structures, the choice of the probe used was justified.

Despite its straightforward approach, the embedding of tissues in phantom for quantitative ultrasonic imaging has been novel.

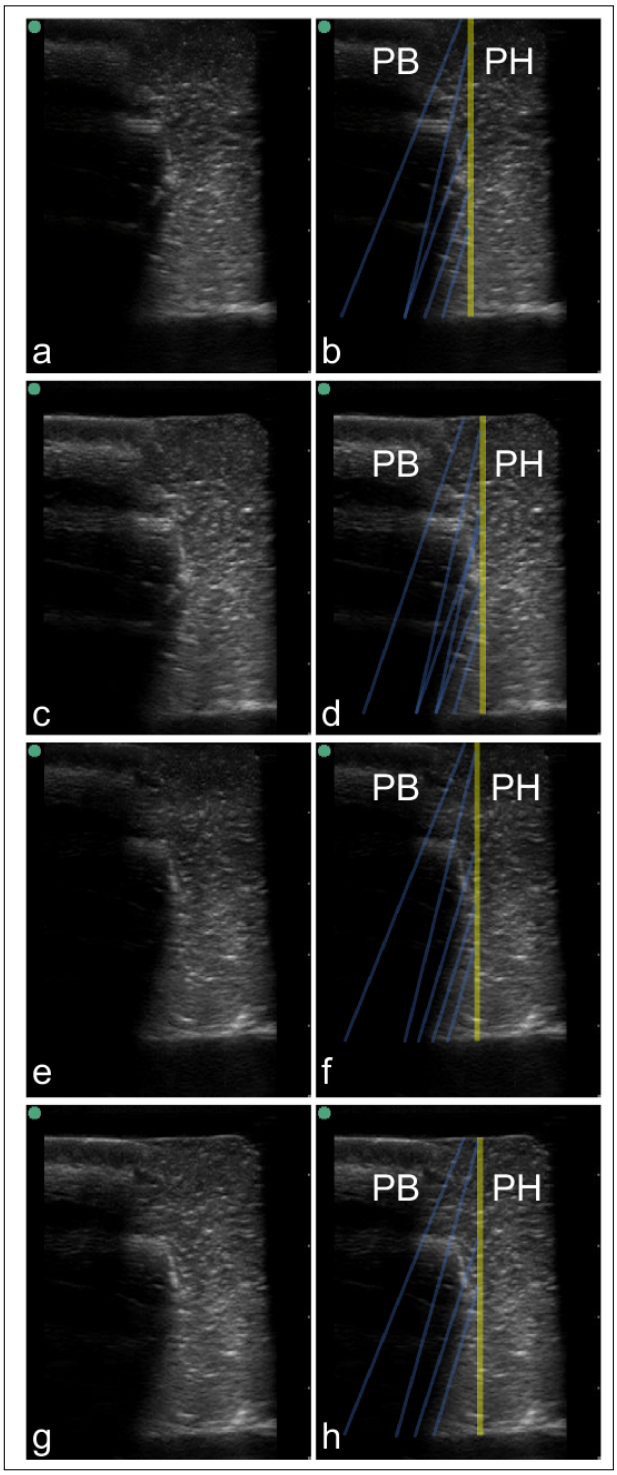


Figure 5.7: Unmarked (a,c,e,g) and marked (b,d,f,h) brightness-mode scans of pork belly (PB) adjacent to phantom material (PH). The separation between pork and phantom material is indicated by a yellow line and zones of increased scattering amplitudes by opaque blue lines.

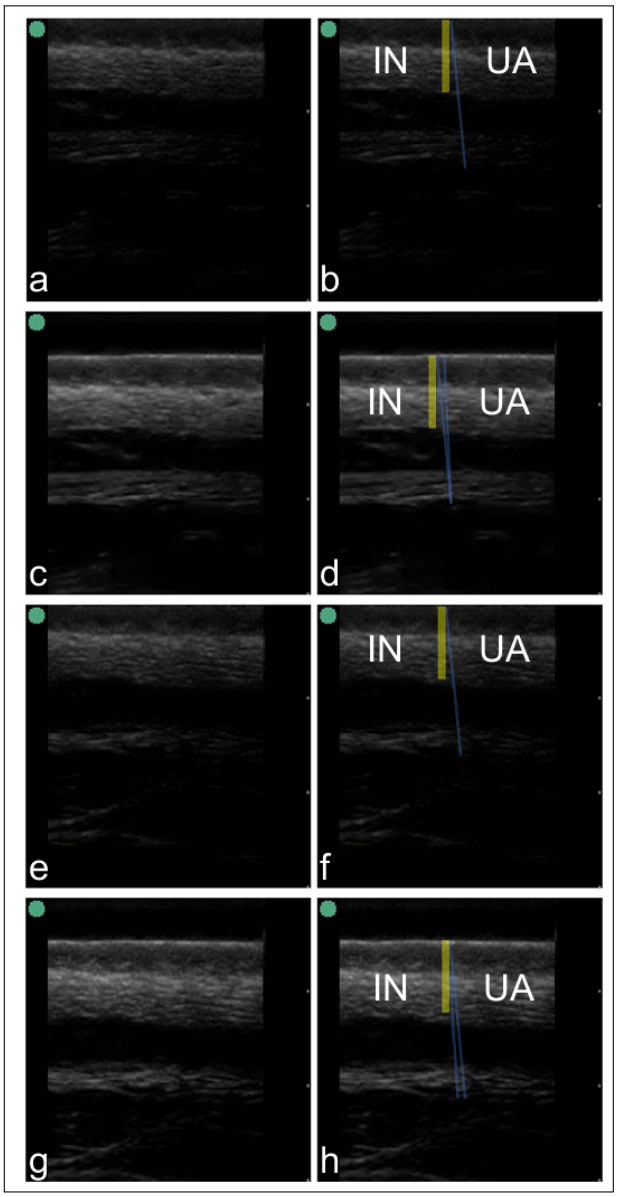


Figure 5.8: Unmarked (a,c,e,g) and marked (b,d,f,h) brightness-mode scans of inked pork belly (IN) and unaltered pork belly (UA). The separation between inked and uninked skin is indicated by a yellow line and zones of increased scattering amplitudes by opaque blue lines.

As for the theoretical considerations, we have used straightforward derivations to deduce acoustic properties of tissues and tissue-mimicking materials from greyscale values in brightness-mode images. Although this idea may not come across as novel, literature on this topic has been sparse, possibly because some commerical ultrasound equipment does not represent birhgtness-mode images on a linear greyscale. Thus, our study has shown benefits of ultrasound equipment without automatic gain control and other image adjustment features.

5.5 Conclusions

Phantom material at room temperature has the same speed of sound as human skin at body temperature. It is therefore a potential alternative for acoustic experiments on skin at lower-than-body temperatures. To our knowledge, no other materials have been proposed for this purpose.

The ratio in speeds of sound of adjacent materials was shown to create distinct highlights in brightness-mode images. The artefacts observed in *in-vivo* brightness-mode scans might be explained from vertical transitions between inked and uninked skin areas.

No prior study has reported the correlation of critical refraction highlighting with the speed of sound of adjacent materials.

This finding is useful for the quantification from brightness-mode ultrasound images of tissue structures deep underneath inked skin in particular, but also for the detection and identification of adjacent media in general from such images.

Acknowledgements

The sonography equipment was kindly supplied by High Tech Medical, Randburg, South Africa. Ethical clearance was obtained from the Human Research Ethics Committee (Medical) of the University of the Witwatersrand, Johannesburg, under Clearance Certificate No. M190808 MED19-07-006. This work has been based on research supported in part by the National Research Foundation of South Africa, Grant Number 127102.

Chapter 6

Sharp Sonic Cutting

This chapter is based on: C. S. Carlson, A. Pohl, D. G. Keir, and M. Postema, "Cutting edge technology: sound sharpens the blade," *Applied Acoustics*, vol. 166, no. 107336, 2020.

The author conceptualised the work; performed the experiments; analysed the data; and wrote the majority of the article. A. Pohl and D. G. Keir developed the prototype transducer used in this work.

Abstract

Constantly sharp knives have applications in industrial cutting, clean shaving, and precision surgery. With the purpose of increasing blade sharpness, an ultrasonic knife was built, operating at 134-kHz continuous ultrasound with an average temperature increase of 0.4 °C at the blade. The sharpness of the incisions made to a sheet of plain printer paper with a blunted blade under sonication were compared to those of the same blade without sonication and to industrially cut paper edges. The incisions from the sonicated blade were visibly sharper than those from the unsonicated blade, and at least as sharp as those from the industrially cut paper edge.

6.1 Introduction

Blades lose their sharpness over time with every cut or shaving stroke made. Research on cutting technology focusses on blade materials and physical sharpening tools. Ultrasound is commonly used in cleaning and sterilising cutting equipment [146].

The role of sonication on cutting performance has previously been investigated with a focus on the processing of food [147–149] and wood [150]. These investigations utilise an application-specific transducer and blade construction. The use of ultrasonic cutting has also been investigated in the support of surgeries [151–153]. However, the key consideration in these investigations was the effect of temperature where a lower temperature rise resulted in less tissue damage.

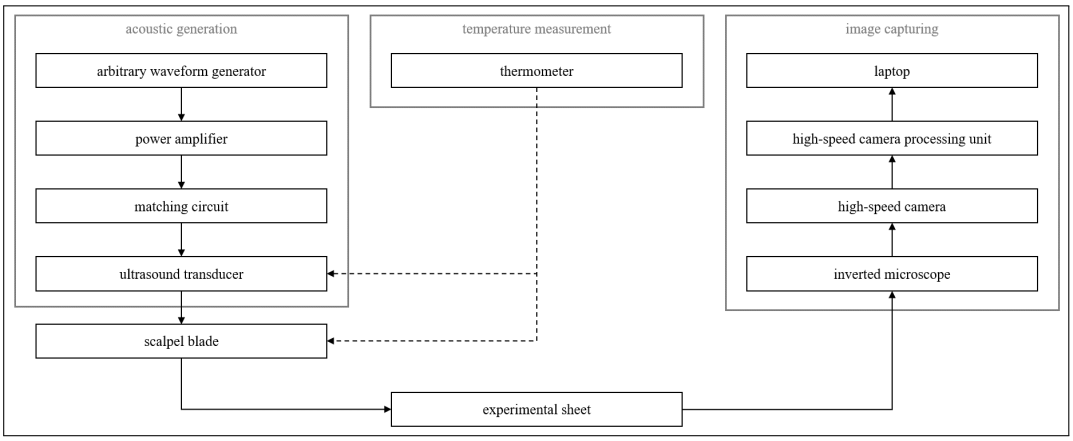
To this purpose, a set-up was designed which allowed for the sonication of an interchangeable blade, whilst keeping the blade temperature consistent. The main applications of this technology are in industrial cutting, clean shaving, and precision surgery.

6.2 Materials and methods

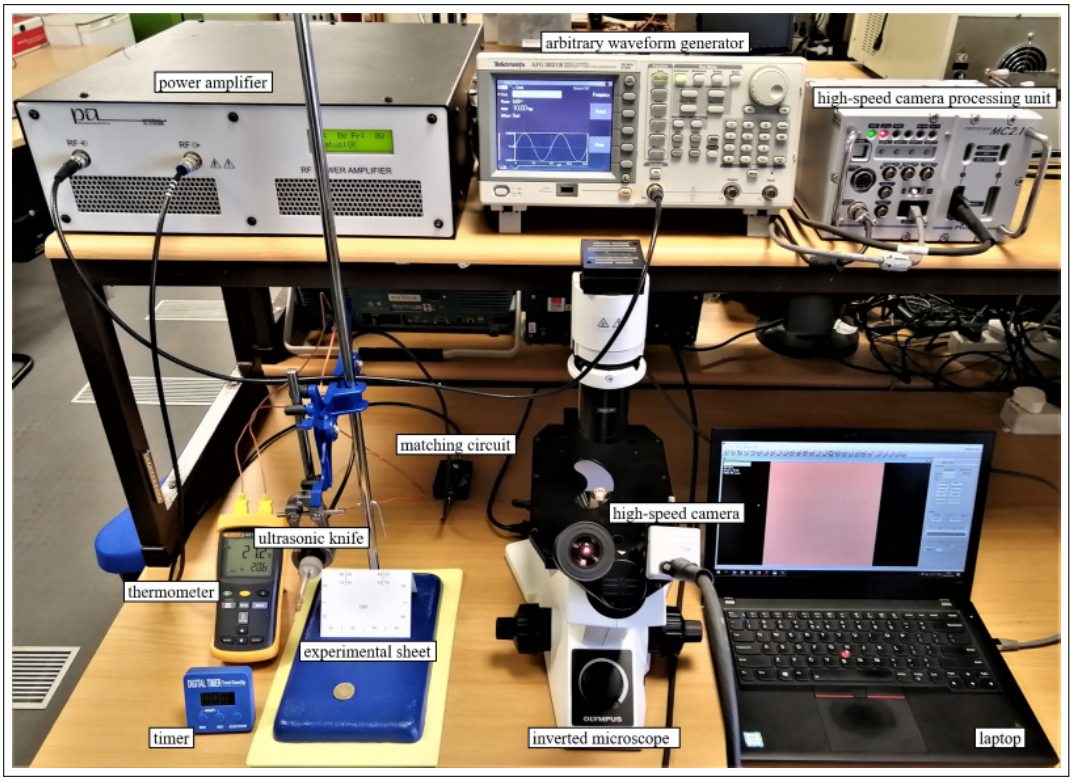
As illustrated in Figure 6.1, an AFG 3021B arbitrary waveform generator (Tektronix Incorporated, Beaverton, Oregon, United States) was used to generate a continuous signal of 134 kHz with a 10-V peak-to-peak amplitude, which was fed into an A-150 55-dB linear power amplifier (ENI Technology, Inc., Rochester, New York, United States). This signal was converted to ultrasound using a custom-built, impedance matched, backed, single element ultrasound transducer that was constructed using a Pz37 piezoelectric disc (Ferroperm Piezoceramics A/S, Kvistgård, Denmark), with a Perspex casing surrounding the transducer. The Pz37 piezoelectric disc was chosen for its low acoustic impedance for improved acoustic matching.

A Perspex rod, serving as a waveguide, with a 6-mm diameter and a 55-mm length was attached to the 13-mm Perspex matching layer by means of a 1-mm diameter wire of 15-mm length. Perspex was used, as it has an acoustic impedance close to that of water. The total length of the matching layer and waveguide corresponded to a multiple of the transducer wavelength for maximum acoustic energy transfer to the blade.

With two screws, a Stainless Steel No. 11 Surgical Scalpel Blade (Swann-Morton Limited, Sheffield, United Kingdom) was attached to the Perspex rod, illustrated in Figure 6.2. The No. 11 surgical scalpel blade is used in surgeries such as ligament reconstruction [154], and laproscopic surgery [155]. It is also commonly used as a hobby knife blade, thus serving multiple purposes. The blade can be easily changed if a different cutting purpose is required. The blade was blunted by manual cutting and exposure.



(a)



(b)

Figure 6.1: A schematic (a) and photograph (b) of the experimental set-up.

The two input channels of a FLUKE 52II THERMOMETER (Fluke Corporation, Everett, Washington, United States) were physically connected to a position on the blade (T1) and to a position to the side of the piezoelectric element (T2), shown in Figure 6.3. Temperature measurements were taken every 30 seconds for 15 minutes.

For sharpness testing, plain printer paper was used. Mondi Rotatrim 160C1E ENVIROWHITE 80 g/m^2 A4 paper (Mondi Limited, Melrose Arch, South Africa)

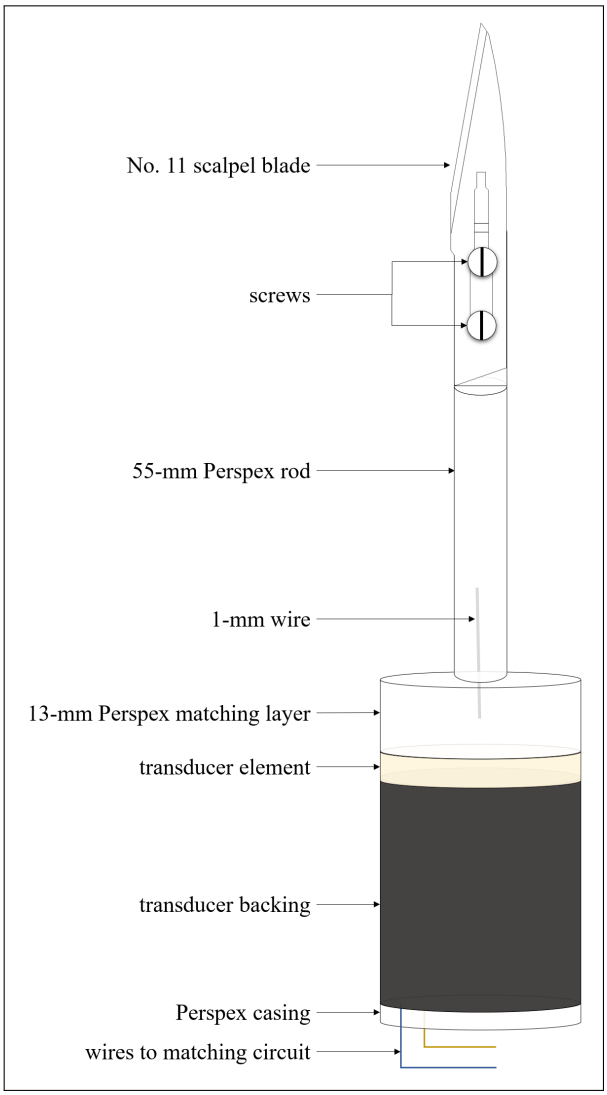


Figure 6.2: Ultrasonic cutting device with a single element ultrasound transducer and a scalpel blade attached with screws to a 55-mm Perspex rod.

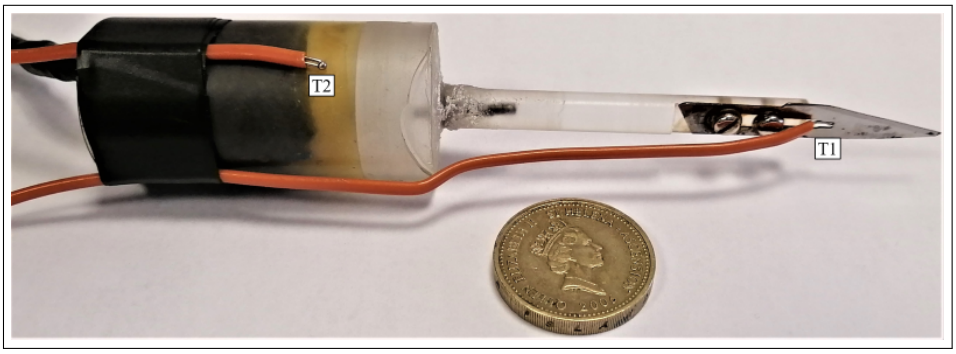


Figure 6.3: Position of the temperature probes on the ultrasonic knife on the blade (T1) and over the ultrasound transducer (T2).

was guillotined into quarters (equivalent to an A6 page size), and each quarter folded in half. The experimental sheet is shown in Figure 6.4. Seventeen of these experimental sheets were used for unsonicated incisions and seventeen for sonicated incisions. Incisions were made manually by the researcher using a forward motion along the length of the blade through the fold at two positions.

The incisions were optically evaluated using a CKX31 inverted microscope (Olympus Corporation, Shinjuku, Tokyo, Japan) with a C-Plan 10× objective lens (Olympus) that has a numerical aperture of 0.25 and a working distance of 10.6 mm. Each experimental sheet was observed at eight positions on the industrially cut edge (E1-E8 in Figure 6.4) and at eight positions on the incisions made (F1-F8 in Figure 6.4).

6.3 Results and discussion

The maximum temperature measured during the 15 minute measurement period was 36.7 °C and 21.4 °C over the ultrasound transducer and at the blade respectively, at an ambient temperature of 21.0 °C. The maximum temperature occurred at 3 minutes. Thereafter the system stabilised where the generation of heat matched the

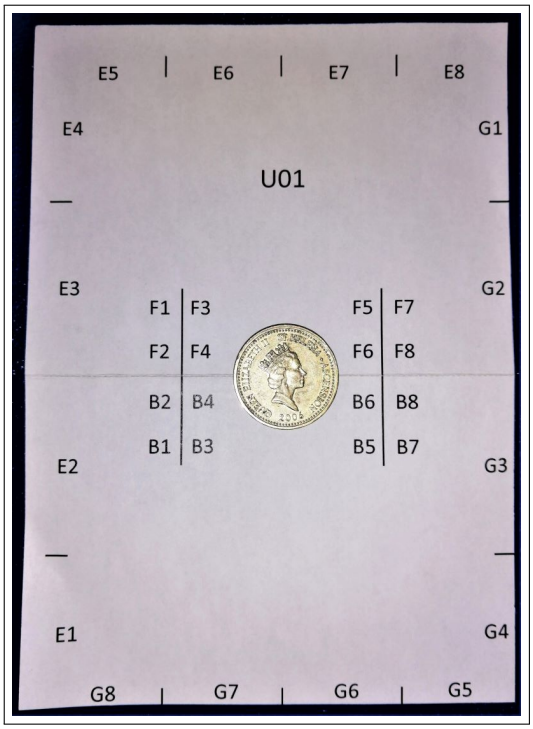


Figure 6.4: A6-sized experimental sheet with marks indicating the industrially cut edge (E1-E8) and along the incisions (F1-F8).

dissipation to the surrounding environment. As seen in Figure 6.5, under sonication the temperature over the ultrasound transducer increased by an average of 14.7 °C (median of 15.5 °C, maximum of 17.0 °C). In comparison, the temperature at the blade increased by an average of 0.4 °C (median of 0.4 °C, maximum of 0.6 °C).

Each experimental sheet was optically evaluated along the incisions resulting in a total sample size of 136 for both the control and the experiment, with an average length of 14 mm and a standard deviation of 1 mm. Incisions outside of this range were excluded from the experiment. Thus analysis was considered for 116 unsonicated samples, and 124 sonicated samples.

Figure 6.6 shows a sample of images of the edge of an industrially-cut sheet of paper as well as demonstration of the incision made by a blunt blade with and without sonication. When cutting with the blade without sonication, the edge of the incision is tortuous with multiple paper fibres visible. In contrast, the incision of the blade with sonication has limited visible paper fibres and a well-defined, non-tortuous edge. The edge of an industrially cut sheet of paper has distinct paper fibres in various planes of focus. Comparing the incision produced by the blade without sonication to the incision produced by the blade with sonication, it is clear that sonication significantly improves the sharpness of the cut. The incision made by the blade with sonication appears to be as sharp as the edge of the industrially cut paper. This indicates that sonication has a sharpening effect on blunt blades. This finding may have implications for multiple fields reliant on sharp, precision cutting.

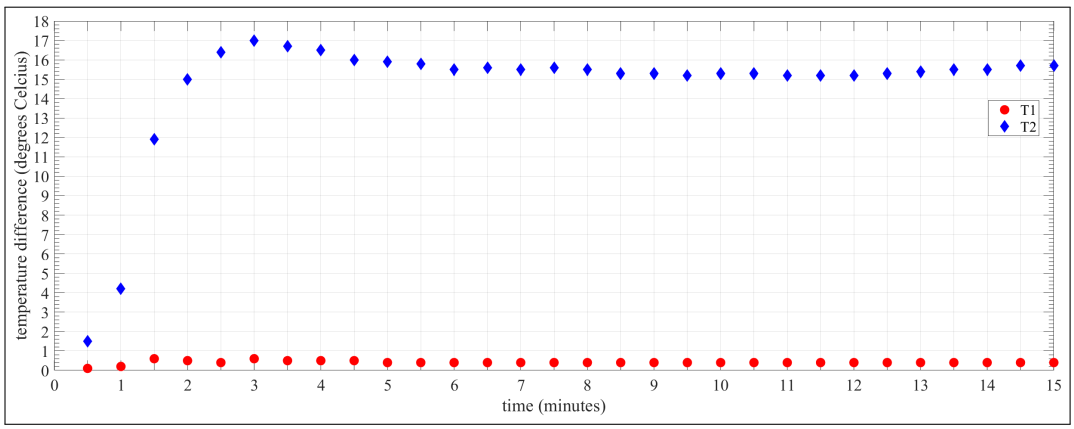


Figure 6.5: Temperature difference over a 15 minute period with the ultrasonic knife under sonication. The red dots indicate the temperature difference at the blade (T1) and blue diamonds indicate the temperature difference over the ultrasound transducer (T2).

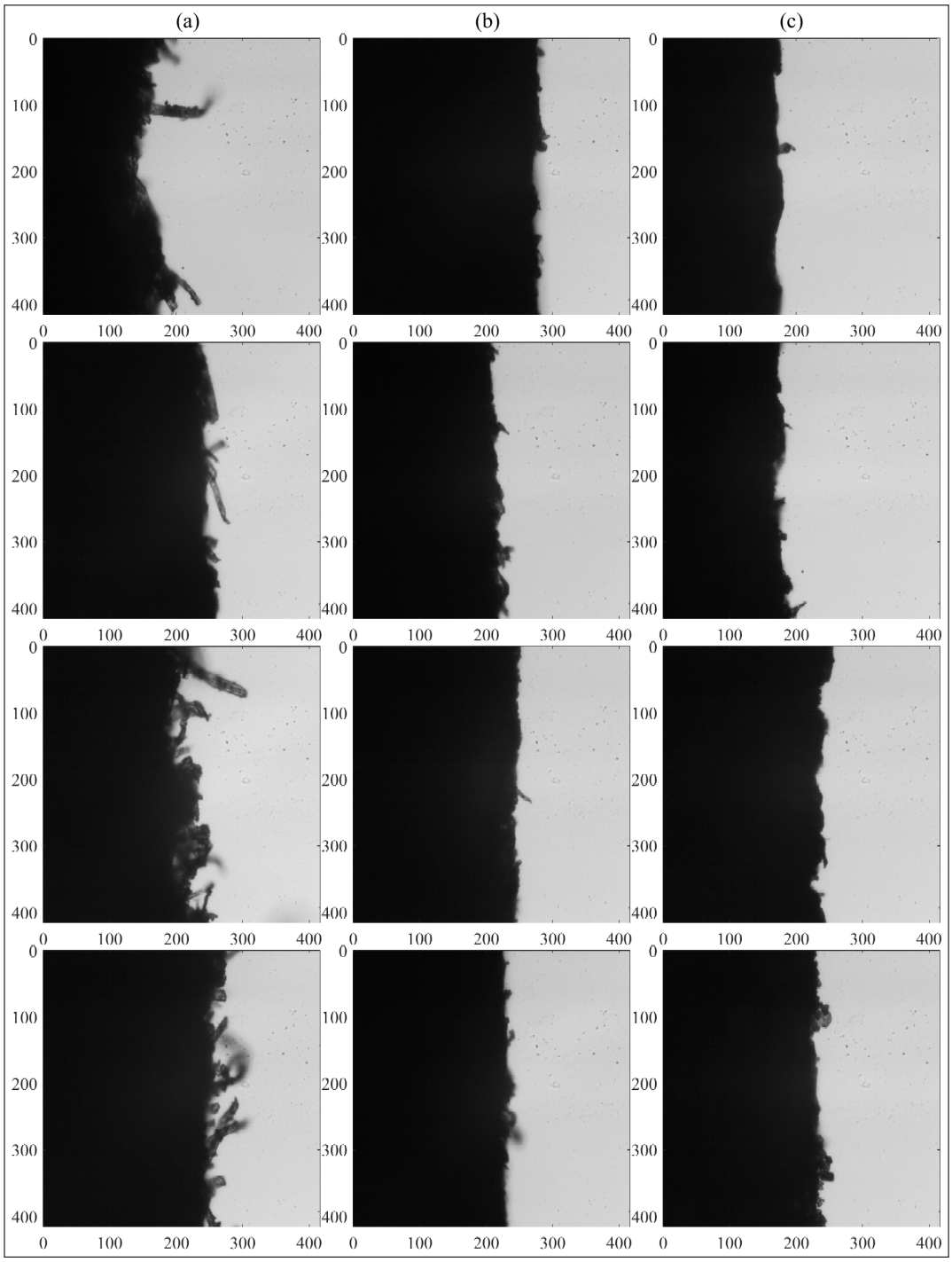


Figure 6.6: Back-lit bright-field 10× microscopy images of incisions in paper from an unsonicated blunt blade (a) and a sonicated blunt blade (b), compared to the paper edge from sharp industrial cutting (c). The darks areas represent the paper. Each frame corresponds to a 416 × 416 (μm^2) area.

6.4 Conclusions

Blades lose their sharpness over time with every cut made. This paper presented a set-up of an ultrasonic knife with an interchangeable blade which showed an average temperature increase of 0.4 °C at the blade whilst improving the cutting ability. Using a continuous 134-kHz 10-V peak-to-peak input signal the ultrasonic knife was confirmed to have fewer visible paper fibres on the edge of the cut when compared to without sonication. Further to this, the sonicated cut appears to be as clean as the industrially cut paper edges. The potential impacts of this technology are in industrial cutting, clean shaving, and precision surgery.

Chapter 7

Discussion

The first objective sought to determine the size distributions and resonance frequency of the pigment particles in black tattoo ink. This objective was addressed in Chapter 2, with the mode particle diameter being 0.29 μm and the largest particle diameter 1.14 μm. The associated resonance frequency of the largest particles was 15 MHz, with the smaller particles even higher. Considering most commercially available medical ultrasound devices have an upper frequency limit of 15 MHz, this finding restricts the potential usefulness of medical ultrasound as a means to manipulate particles using resonance. This does not exclude the possibility of a custom device being developed to achieve particle disruption. However, this falls outside of the scope of this thesis.

The aim of Objective 2 was to quantify the speed of sound and attenuation coefficient of pure black tattoo ink using ultrasound. This objective was addressed in Chapter 2. These properties were found to be 1639 $\mathrm{m\,s^{-1}}$ and 0.15 ± 0.01 $\mathrm{dB\,cm^{-1}\,MHz^{-1}}$ at steady-state. The transient scattering that was observed in the pure black tattoo ink, and associated transient changes of the speed of sound and attenuation was an unexpected observation which supports existing literature that hydrophobic carbon black acts as cavitation nuclei under sonication. More importantly to note, the method introduced to determine the speed of sound and attenuation coefficient is quick and does not require additional specialised equipment aside the medical ultrasound device. This method is not limited to black tattoo ink, but could be used for other materials with unknown speeds of sound and attenuation coefficients.

Considering the transient nucleation observed in pure black tattoo ink, the aim of Objective 3 was to determine the nucleation threshold of black tattoo ink. This objective was addressed in Chapter 3 and Chapter 4. The theoretical nucleation threshold was calculated to be 1.3$\times$ the resting radius, which could not be confirmed

precisely through experiments, but it was confirmed to be lower than the Blake cavitation threshold of 2× the resting radius in a low concentration of black tattoo ink. When considering pure black ink, the nucleation threshold could not be determined due to the high concentration of carbon black pigments obscuring observation. This lower nucleation threshold indicates that there is a possibility that black tattoo ink could be manipulated with clinically safe ultrasound.

The outcome of Objective 4 was to quantify the change of the speed of sound and attenuation coefficient in tissues due to *in situ* black tattoo ink using ultrasound. Chapter 5 served to address this objective. There was a minor change observed in the speed of sound in the sample materials. The attenuation coefficient also decreased by 1-dB cm^{-1} in a tattooed region. These changes are lower than expected. Knowing that tattoos are only a matter of millimetres thick may account for the inconclusive results observed. Due to the unknown concentration and distribution of ink in the samples, the presented method could not be fully validated. The fact that the results are inconclusive in the controlled *in vitro* environment casts doubt whether the presented method could be reliably extended for *in vivo* use.

Objective 5 was intended to describe the artefacts that tattoos introduce on ultrasound images. This objective was addressed in Chapter 5. Bands of increased scattering was observed at the interface between tissues of different speeds of sound. The concept of critical refraction highlighting was defined to describe these artefacts. The identification of these bands allows for the identification of the interface between materials of different speeds of sound, as well as determining what the speed of sound is in one of the materials provided the other is known. Even under *in vitro* cases the identification of the bands of increased scattering is subjective. This may restrict the feasibility of extending critical refraction highlighting as a reliable means to identify the transitions between materials with different speeds of sound.

Finally, Objective 6 sought to demonstrate the sharpening effect that ultrasound has on fixed-blade cutting devices. Chapter 6 presents the work to address this objective. The edges of sonicated cuts were visibly sharper than the edges of unsonicated cuts, demonstrating the anticipated outcome using a single frequency, cutting edge and material to be cut. As a proof of concept implementation, the objective has been met. However, the results are limited so a definite conclusion cannot be made that ultrasound will sharpen cuts under all conditions.

The results presented contribute to the knowledge base of tattoos and ultrasound. However, there are several limitations that must be acknowledged. First and foremost

this study was restricted to black tattoo ink only, which leaves a gap in the knowledge of other coloured inks. The methods presented in Chapter 2 and Chapter 5 are reliant on a controlled experimental environment which restricts the possibility of extending the study to a less controlled environment. The effect of concentration is not known as pure ink or very low concentrations of ink were used in the experiments. In the *in vitro* and *in vivo* experiments the concentration of the ink is unknown. This may have an impact on the change of hydrophobicity that has been identified. To close the knowledge gap of the role of hydrophobicity in tattoos, it would be beneficial to dehydrophobise the tattoo ink and use it *in vivo* to investigate whether it remains *in situ*, or is absorbed by the body.

Considering the results presented in this thesis, it can be concluded that it is possible to understand more about tattoos and tattoo inks using ultrasound. However, as it stands it appears more promising to use ultrasound as a diagnostics tool rather than a tool to administer and manipulate tattoos and tattoo inks. The methods introduced in this thesis to determine the speed of sound and attenuation coefficients of materials, as well as critical refraction highlighting, are a significant contribution of this work since it can also be applied in multiple fields outside of tattoos and tattoo inks.

References

[1] A. Deter-Wolf, B. Robitaille, L. Krutak, and S. Galliot, "The world's oldest tattoos," *Journal of Archaeological Science: Reports*, vol. 5, pp. 19–24, 2016.

[2] A. E. Laumann and A. J. Derick, "Tattoos and body piercings in the United States: a national data set," *Journal of the American Academy of Dermatology*, vol. 55, no. 3, pp. 413–421, 2006.

[3] N. Kluger, S. Seité, and C. Taieb, "The prevalence of tattooing and motivations in five major countries over the world," *Journal of the European Academy of Dermatology and Venereology*, vol. 33, no. 12, pp. e484–e486, 2019.

[4] W. Heywood, K. Patrick, A. M. A. Smith, J. M. Simpson, M. K. Pitts, J. Richters, and J. M. Shelley, "Who gets tattoos? Demographic and behavioral correlates of ever being tattooed in a representative sample of men and women," *Annals of Epidemiology*, vol. 22, no. 1, pp. 51–56, 2012.

[5] A. Stirn, A. Hinz, and E. Brähler, "Prevalence of tattooing and body piercing in Germany and perception of health, mental disorders, and sensation seeking among tattooed and body-pierced individuals," *Journal of Psychosomatic Research*, vol. 60, pp. 531–534, 2006.

[6] M. A. Kayıran, E. Özkul, and M. S. Gürel, "Tattoos: why do we get? What is our attitude?" *Turkish Journal of Dermatology*, vol. 14, pp. 18–22, 2020.

[7] T. Høgsberg, K. Hutton Carlsen, and J. Serup, "High prevalence of minor symptoms in tattoos among a young population tattooed with carbon black and organic pigments," *Journal of the European Academy of Dermatology and Venereology*, vol. 27, no. 7, pp. 846–852, 2013.

[8] A. Aslam and C. M. Owen, "Fashions change but tattoos are forever: time to regret," *British Medical Journal*, vol. 169, no. 6, pp. 1364–1366, 2018.

[9] N. Kluger, L. Misery, S. Seité, and C. Taieb, "Regrets after tattooing and tattoo removal in the general population of France," *Journal of the European Academy of Dermatology and Venereology*, vol. 33, pp. e157–e159, 2019.

[10] S. Varma and S. Lanigan, "Reasons for requesting laser removal of unwanted tattoos," *British Journal of Dermatology*, vol. 140, pp. 483–485, 1999.

[11] J. Latreille, J. L. Levy, and C. Guinot, "Decorative tattoos and reasons for their removal: a prospective study in 151 adults living in south of France," *Journal of the European Academy of Dermatology and Venereology*, vol. 25, no. 2, pp. 181–187, 2011.

[12] G. W. Grumet, "Psychodynamic implications of tattoos," *American Journal of Orthopsychiatry*, vol. 53, no. 3, pp. 482–492, 1983.

[13] K. Sperry, "Tattoos and tattooing part 1: history and methodology," *American Journal of Forensic Medicine and Pathology*, vol. 12, no. 4, pp. 313–318, 1991.

[14] A. Oanță, M. Irimiei, D. Brănișteanu, G. Stoleriu, and S. Morariu, "Tattoos: history and actuality," *Medical Sciences*, vol. 7, no. 2, pp. 125–132, 2014.

[15] N. Khunger, A. Molpariya, and A. Khunger, "Complications oftattoos and tattoo removal: stop and think before you ink," *Journal of Cutaneous and Aesthetic Surgery*, vol. 8, no. 1, pp. 30–36, 2015.

[16] K. Burris and K. Kim, "Tattoo removal," *Clinics in Dermatology*, vol. 25, pp. 388–392, 2007.

[17] S. M. Sweeney, "Tattoos: a review of tattoo practices and potential treatment options for removal," *Current Opinion in Pediatrics*, vol. 18, pp. 391–395, 2006.

[18] T. Isaacs, R. M. Ngwanya, and R. J. Lehloenya, "Tattoos: a summary knowledge for the practising clinician," *South African Medical Journal*, vol. 108, no. 9, pp. 714–720, 2018.

[19] S. M. Weiler, B.-O. Tetzlaff, P. Y. Herzberg, and T. Jacobsen, "When personality gets under the skin: need for uniqueness and body modifications," *PLoS ONE*, vol. 16, no. e0245158, 2021. [Online]. Available: http://dx.doi.org/10.1371/journal.pone.0245158

[20] M. L. Armstrong, "Career-oriented women with tattoos," *Journal of Nursing Scholarship*, vol. 23, no. 4, pp. 215–220, 1991.

[21] M. Kang and K. Jones, "Why do people get tattoos?" *Contexts*, vol. 6, no. 1, pp. 42–47, 2007.

[22] L. Kierstein and C. Kjelskau, "Tattoo as art, the drivers behind the fascination and the decision to become tattooed," *Current Problems in Dermatology*, vol. 48, pp. 37–40, 2015.

[23] L. M. Uyeda, "Permanent dots in radiation therapy," *Radiologic Technology*, vol. 58, no. 5, pp. 409–411, 1987.

[24] J. J. Kim, "Temporary henna tattoos as an alternative marking method for external beam radiation therapy patients who decline permanent tattoos," *Journal of Medical Imaging and Radiation Sciences*, vol. 46, no. S1, pp. S10–S11, 2015.

[25] E. Dawson, A. Maino, and J. Lee, "A unique use for a corneal tattoo," *Strabismus*, vol. 17, no. 3, pp. 98–100, 2009.

[26] N. Islam and W. Franks, "Therapeutic corneal tattoo following peripheral iridotomy complication," *Eye*, vol. 20, pp. 389–390, 2006.

[27] L. Franczak, "How tattoos can complement breast reconstruction," *AMA Journal of Ethics*, vol. 20, no. 4, pp. 396–402, 2018.

[28] T. Høgsberg, K. Loeschner, D. Löf, and J. Serup, "Tattoo inks in general usage contain nanoparticles," *British Journal of Dermatology*, vol. 165, no. 6, pp. 1210–1218, 2011.

[29] C. A. Grant, P. C. Twigg, R. Baker, and D. J. Tobin, "Tattoo ink nanoparticles in skin tissue and fibroblasts," *Beilstein Journal of Nanotechnology*, vol. 6, no. 1, pp. 1183–1191, 2015.

[30] W. Bäumler, "Chemical hazard of tattoo colorants," *La Presse Médicale*, vol. 49, no. 104046, 2020.

[31] N. Jacobsen and P. Clausen, "Carbon black nanoparticles and other problematic constituents of black ink and their potential to harm tattooed humans," *Current Problems in Dermatology*, vol. 48, pp. 170–175, 2015.

[32] P. Minghetti, U. M. Musazzi, R. Dorati, and P. Rocco, "The safety of tattoo inks: possible options for a common regulatory framework," *Science of the Total Environment*, vol. 651, pp. 634–637, 2019.

[33] M. Giulbudagian, I. Schreiver, A. Vikram, S. Peter, and L. Andreas, "Safety of tattoos and permanent make-up: a regulatory view," *Archives of Toxicology*, vol. 94, pp. 357–369, 2020.

[34] J. Kazandjieva and N. Tsankov, "Tattoos: dermatological complications," *Clinics in Dermatology*, vol. 25, no. 4, pp. 375–382, 2007.

[35] N. Kluger and V. Koljonen, "Tattoos, inks, and cancer," *The Lancet Oncology*, vol. 13, no. 4, pp. e161–e168, 2012.

[36] K. Hutton Carlsen and J. Serup, "Patients with tattoo reactions have reduced quality of life and suffer from itch dermatology life quality index and itch severity score measurements," *Skin Research and Technology*, vol. 21, no. 1, pp. 101–107, 2015.

[37] Y. Eklund and A. Troilius Rubin, "Laser tattoo removal, precautions, and unwanted effects," *Current Problems in Dermatology*, vol. 48, pp. 88–96, 2015.

[38] G. E. Long and L. S. Rickman, "Infectious complications of tattoos," *Infectious Diseases*, vol. 18, no. 4, pp. 610–619, 1994.

[39] F. Rosenkilde, "Tattoo machines, needles and utilities," *Current Problems in Dermatology*, vol. 48, pp. 21–30, 2015.

[40] P. Harrison, "The surgical removal of amateur tattoos," *Clinical and Experimental Dermatology*, vol. 10, no. 6, pp. 540–544, 1985.

[41] W. Kirby, C. L. Chen, A. Desai, and T. Desai, "Causes and recommendations for unanticipated ink retention following tattoo removal treatment," *Journal of Clinical and Aesthetic Dermatology*, vol. 6, no. 7, pp. 27–31, 2013.

[42] S. Luebberding, "New tattoo approaches in dermatology," *Dermatologic Clinics*, vol. 32, pp. 91–96, 2014.

[43] M. Kuperman-Beade, V. J. Levine, and R. Ashinoff, "Laser removal of tattoos," *American Journal of Clinical Dermatology*, vol. 2, no. 1, pp. 21–25, 2001.

[44] W. Bäumler and K. T. Weiß, "Laser assisted tattoo removal: state of the art and new developments," *Photochemical and Photobiological Sciences*, vol. 18, pp. 349–358, 2019.

[45] S. Shah and S. Aurangabadkar, "Newer trends in laser tattoo removal," *Journal of Cutaneous and Aesthetic Surgery*, vol. 8, no. 1, pp. 25–29, 2015.

[46] D. Hazlewood and X. Yang, "Enhanced laser surface ablation with an integrated photoacoustic imaging and high intensity focused ultrasound system," *Lasers in Surgery and Medicine*, vol. 51, no. 7, pp. 616–624, 2019.

[47] J. Teng, *Ultrasound: An Alternative Solution for Removing Tattoos.* Dissertation. Massachusetts Institute of Technology, 2005.

[48] J. Serup, T. Bove, T. Zawada, A. Jessen, and M. Poli, "High-frequency (20 MHz) high-intensity focused ultrasound: New ablative method for color-independent tattoo removal in 1–3 sessions. An open-label exploratory study," *Skin Research and Technology*, vol. 26, pp. 839–850, 2020.

[49] S. Ishikura, M. Yoshizawa, N. Tagawa, and T. Irie, "Visualization of frequency dependence of tissue characteristics by phase-contrast imaging based on ultrasonic interference method," *Japanese Journal of Applied Physics*, vol. 57, no. 07LF20, 2018.

[50] K. Johansen, E. Kimmel, and M. Postema, "Theory of red blood cell oscillations in an ultrasound field," *Archives of Acoustics*, vol. 42, no. 1, pp. 121–126, 2017.

[51] D. M. Rubin, N. Anderton, C. Smalberger, J. Polliack, M. Nathan, and M. Postema, "On the behaviour of living cells under the influence of ultrasound," *Fluids*, vol. 3, no. 4, 2018.

[52] E. Zilonova, M. Solovchuk, and T. W. H. Sheu, "Bubble dynamics in viscoelastic soft tissue in high-intensity focal ultrasound thermal therapy," *Ultrasonics Sonochemistry*, vol. 40, pp. 900–911, 2018.

[53] M. Postema and G. Schmitz, "Bubble dynamics involved in ultrasonic imaging," *Expert Review of Molecular Diagnostics2*, vol. 6, no. 3, pp. 493–502, 2006.

[54] M. Guédra, S. Cleve, C. Mauger, P. Blanc-benon, and C. Inserra, "Dynamics of nonspherical microbubble oscillations above instability threshold," *Physical Review*, vol. 96, no. 063104, 2017.

[55] S. Cleve, M. Guédra, C. Inserra, C. Mauger, and P. Blanc-benon, "Surface modes with controlled axisymmetry triggered by bubble coalescence in a high-amplitude acoustic field," *Physical Review*, vol. 98, no. 033115, 2018.

[56] T. Kambayashi, T. Saeki, and I. Buchanan, "Wastewater treatment with acoustic separator," *Japanese Journal of Applied Physics*, vol. 56, no. 07JE04, 2017.

[57] J. Kim, J. Kim, J. Yeom, K. Ha, and M. Kim, "Size distribution of Nanoparticles In the droplets ultrasonically atomized from Al_2O_3 suspension," *Japanese Journal of Applied Physics*, vol. 56, no. 07JD04, 2017.

[58] S. Nishitaka, D. Mashiko, S. Yoshizawa, and S.-I. Umemura, "Effect of scanning the focus on generating cavitation bubbles and reactive oxygen species by using trigger high-intensity focused ultrasound sequence," *Japanese Journal of Applied Physics*, vol. 57, no. 07LF25, 2018.

[59] M. Kim and J. Kim, "Nanoparticle dispersionizer by ultrasonic cavitation and streaming," *Japanese Journal of Applied Physics*, vol. 57, no. 07LE03, 2018.

[60] M. Postema, R. Matsumoto, R. I. Shimizu, A. T. Poortinga, and N. Kudo, "High-speed footage shows transient ultrasonic nucleation of different hydrophobic particles in suspension," *Japanese Journal of Applied Physics*, vol. 59, no. SKKD07, 2020.

[61] N. Kudo, R. Uzbekov, R. Matsumoto, R.-i. Shimizu, C. S. Carlson, N. Anderton, A. Deroubaix, C. Penny, A. T. Poortinga, D. M. Rubin, A. Bouakaz, and M. Postema, "Asymmetric oscillations of endoskeletal antibubbles," *Japanese Journal of Applied Physics*, vol. 59, no. SKKE02, 2020.

[62] N. Kudo, R. Uzbekov, R. Matsumoto, R.-i. Shimizu, C. Carlson, N. Anderton, A. Deroubaix, C. Penny, A. T. Poortinga, D. M. Rubin, A. Bouakaz, and M. Postema, "Oscillating endoskeletal antibubbles," in *Proceedings of the 40th Symposium on Ultrasonic Electronics*, vol. 2E3–1, 2019.

[63] M. Kudo, *Contrast Harmonic Imaging in the Diagnosis and Treatment of Hepatic Tumors*. Springer, Tokyo, 2003.

[64] S. Turco, P. Frinking, R. Wildeboer, M. Arditi, H. Wijkstra, J. R. Lindner, and M. Mischi, "Constrast-enhanced ultrasound quantification: from kinetic modeling to machine learning," *Ultrasound in Medicine and Biology*, vol. 46, no. 3, pp. 518–543, 2020.

[65] M. T. French, K. Mortensen, and A. R. Timming, "Are tattoos associated with employment and wage discrimination? Analyzing the relationships between body art and labor market outcomes," *Human Relations*, vol. 72, no. 5, pp. 962–987, 2019.

[66] S. T. Carroll, R. H. Riffenburgh, T. A. Roberts, and E. B. Myhre, "Tattoos and body piercings as indicators of adolescent risk-taking behaviors," *Pediatrics*, vol. 109, no. 6, pp. 1021–1027, 2002.

[67] K. Hutton Carlsen, J. Tolstrup, and J. Serup, "High-frequency ultrasound imaging of tattoo reactions with histopathology as a comparative method. Introduction of preoperative ultrasound diagnostics as a guide to therapeutic intervention," *Skin Research and Technology*, vol. 20, no. 3, pp. 257–264, 2014.

[68] J. Serup, "Diagnostic tools for doctors' evaluation of tattoo complications," *Current Problems in Dermatology*, vol. 52, pp. 42–57, 2017.

[69] A. Humphries, T. S. Lister, P. A. Wright, and M. P. Hughes, "Determination of the thermal and physical properties of black tattoo ink using compound analysis," *Lasers in Medical Science*, vol. 28, no. 4, pp. 1107–1112, 2013.

[70] M. Postema, S. Phadke, A. Novell, R. Uzbekov, C. Nyamupangedengu, M. Anouti, and A. Bouakaz, "Ultrasonic identification technique in recycling of lithium ion batteries," in *Proceedings of the 2019 IEEE AFRICON*, no. 9133954, 2019.

[71] J. Bamber, "Ultrasonic attenuation in fresh human tissues," *Ultrasonics*, vol. 19, no. 4, pp. 187–188, 1981.

[72] F. A. Duck, *Physical Properties of Tissue: A Comprehensive Reference Book*. Academic Press, London, 1990.

[73] W. Secomski, A. Nowicki, and P. Tortoli, "Estimation of hematocrit by means of attenuation measurement of ultrasonic wave in human blood," in *Proceedings of the 2001 IEEE Ultrasonics Symposium*, 2001, pp. 1277–1280.

[74] M. M. Calor-Filho and J. C. Machado, "Measurement of the ultrasonic attenuation coefficient of human blood plasma during clotting in the frequency range of 8 to 22 MHz," *Ultrasound in Medicine and Biology*, vol. 32, no. 7, pp. 1055–1064, 2006.

[75] B. Patterson and D. L. Miller, "Experimental measurements of ultrasound attenuation in human chest wall and assessment of the mechanical index for lung ultrasound," *Ultrasound in Medicine and Biology*, vol. 46, no. 6, pp. 1442–1454, 2020.

[76] T. Yoshida and T. Kondo, "Measurement on ultrasonic attenuation coefficient of tissue mimicking materials," in *Proceedings of the 30th Symposium on Ultrasonic Electronics*, 2009, pp. 23–24.

[77] A. I. Farrer, H. Odéen, J. de Bever, B. Coats, D. L. Parker, A. Payne, and D. A. Christensen, "Characterization and evaluation of tissue-mimicking gelatin phantoms for use with MRgFUS," *Journal of Therapeutic Ultrasound*, vol. 3, no. 9, 2015.

[78] C.-T. Chen, L.-S. Chen, and F. J. Millero, "Speed of sound in NaCl, $MgCl_2$, Na_2SO_4, and $MgSO_4$ aqueous solutions as functions of concentration, temperature, and pressure," *Journal of the Acoustical Society of America*, vol. 63, no. 6, pp. 1795–1800, 1978.

[79] S. J. Kleis and L. A. Sanchez, "Dependence of speed of sound on salinity and temperature in concentrated NaCl solutions," *Solar Energy*, vol. 45, no. 4, pp. 201–206, 1990.

[80] E. Franceschini, F. T. H. Yu, F. Destrempes, and G. Cloutier, "Ultrasound characterization of red blood cell aggregation with intervening attenuating tissue-mimicking phantoms," *Journal of the Acoustical Society of America*, vol. 127, no. 2, pp. 1104–1115, 2010.

[81] M. Postema, *Fundamentals of Medical Ultrasonics*. Taylor & Francis, London, 2011.

[82] P. Attard, "Nanobubbles and the hydrophobic attraction," *Advances in Colloid and Interface Science*, vol. 104, no. 1-3, pp. 75–91, 2003.

[83] T. Leighton, *The Acoustic Bubble*. Academic Press, London, 1994.

[84] M. Postema, R. Matsumoto, R. I. Shimizu, A. T. Poortinga, and N. Kudo, "Ultrasound homogenises suspensions of hydrophobic particles," in *Proceedings of the 40th Symposium on Ultrasonic Electronics*, no. 2E2–4, 2019.

[85] K. Johansen and M. Postema, "Lagrangian formalism for computing oscillations of spherically symmetric encapsulated acoustic antibubbles," *Hydroacoustics*, vol. 19, pp. 197–208, 2016.

[86] G. ter Haar, "Ultrasonic imaging: safety considerations," *Interface Focus*, vol. 1, no. 4, pp. 686–697, 2011.

[87] K. Attenborough and M. Postema, *A pocket-sized introduction to acoustics*. University of Hull, Kingston upon Hull, 2008.

[88] A. Deroubaix, B. Moahla, and C. Penny, "Monitoring of intracellular localization of hepatitis B virus P22 protein using laser scanning confocal microscopy and Airyscan," *Microscopy Research and Technique*, vol. 83, no. 5, pp. 499–506, 2020.

[89] M. Nathan, *Ultrasonic Blood Fractionation*. Dissertation. University of the Witwatersrand, Johannesburg, 2020.

[90] C. Smalberger, *Ultrasound-Assisted Cell Eradication*. Dissertation. University of the Witwatersrand, Johannesburg, 2020.

[91] R. O. Bude and R. S. Adler, "An easily made, low-cost, tissue-like ultrasound phantom material," *Journal of Clinical Ultrasound*, vol. 23, no. 4, pp. 271–273, 1995.

[92] K. Suzuki, R. Iwasaki, R. Takagi, S. Yoshizawa, and S.-i. Umemura, "Simultaneous observation of cavitation bubbles generated in biological tissue by high-speed optical and acoustic imaging methods," *Japanese Journal of Applied Physics*, vol. 56, no. 07JF27, 2017.

[93] N. Kudo, "High-speed in situ observation system for sonoporation of cells with size- and position-controlled microbubbles," *IEEE Transactions on Ultrasonics, Ferroelectrics, and Frequency Control*, vol. 64, no. 1, pp. 273–280, 2017.

[94] S. Imai and N. Kudo, "Development of a microvascular phantom for studies on microbubble dynamics and bubble-cell interaction inside a capillary," in *Proceedings of the 2018 IEEE Ultrasonics Symposium*, no. 184, 2018.

[95] M. Chan and K. Soetanto, "Study on contrast effect of microbubbles as ultrasound contrast agents," *Japanese Journal of Applied Physics*, vol. 37, no. 3078, 1998.

[96] K. Soetanto and M. Chan, "Fundamental studies on contrast images from different-sized microbubbles: analytical and experimental studies," *Ultrasound in Medicine and Biology*, vol. 26, no. 1, pp. 81–91, 2000.

[97] S. Tano, N. Ueno, T. Tomiyama, and K. Kimura, "Possibility of differentiating small hyperechoic liver tumours using contrast-enhanced colour doppler ultrasonography: a preliminary study," *Clinical Radiology*, vol. 52, pp. 41–45, 1997.

[98] J.-M. Correas, O. Høløønon, and J.-F. Moreau, "Contrast-enhanced ultrasonography of native and transplanted kidney diseases," *European Radiology*, vol. 9, Suppl., pp. S394–S400, 1999.

[99] H. Yoshikawa, T. Azuma, K. Sasaki, K.-i. Kawabata, and S.-i. Umemura, "Dynamic and precise visualization of contrast agent in blood vessels with motion correction," *Japanese Journal of Applied Physics*, vol. 45, no. 5B, pp. 4754–4760, 2006.

[100] K. Numata, W. Luo, M. Morimoto, M. Kondo, Y. Kunishi, T. Sasaki, A. Nozaki, and K. Tananka, "Contrast enhanced ultrasound of hepatocellular carcinoma," *World Journal of Radiology*, vol. 2, no. 2, pp. 68–82, 2010.

[101] H. Uemura, F. Sano, A. Nomiya, T. Yamamoto, M. Nakamura, Y. Miyoshi, K. Miki, K. Noguchi, S. Egawa, Y. Homma, and Y. Kubota, "Usefulness of perflubutane microbubble-enhanced ultrasound in imaging and detection of prostate cancer: phase II multicenter clinical trial," *World Journal of Urology*, vol. 31, pp. 1123–1128, 2013.

[102] K.-i. Kawabata, N. Sugita, H. Yoshikawa, T. Azuma, and S.-i. Umemura, "Nanoparticles with multiple perfluorocarbons for controllable ultrasonically induced phase shifting," *Japanese Journal of Applied Physics*, vol. 44, no. 6B, pp. 4548–4552, 2005.

[103] M. Tanabe, K. Okubo, N. Tagawa, and T. Moriya, "Inline transmitter/receiver system using $Pb(Zn_{1/3}Nb_{2/3})O_3$–$PbTiO_3$ single crystal and poly(vinylidene fluoride) for harmonic pulse compression imaging," *Japanese Journal of Applied Physics*, vol. 47, no. 5, pp. 4149–4145, 2008.

[104] W. Luo, K. Numata, M. Morimoto, M. Kondo, S. Takebayashi, M. Okada, S. Morita, and K. Tanaki, "Focal liver tumors: characterization with 3D perflubutane microbubble agent–enhanced US versus 3D contrast-enhanced multidetector CT," *Radiology*, vol. 251, no. 1, pp. 287–295, 2009.

[105] M. Lafond, A. Watanabe, S. Yoshizawa, S.-i. Umemura, and K. Tachibana, "Cavitation-threshold determination and rheological-parameters estimation of albumin-stabilized nanobubbles," *Scientific Reports*, vol. 8, no. 7472, 2018.

[106] M. Chan, K. Soetanto, and M. Okujima, "Acoustic properties of surfactant microbubbles in relation to their lifetime in vitro as determined by diffusion," *Japanese Journal of Applied Physics*, vol. 35, no. 5B, pp. 3148–3151, 1996.

[107] M. Postema, A. Bouakaz, F. J. ten Cate, G. Schmitz, N. de Jong, and A. van Wamel, "Nitric oxide delivery by ultrasonic cracking: some limitations," *Ultrasonics*, vol. 44, pp. e109–e113, 2006.

[108] C. Beavers, D. Flinchum, and T. Ayyoubi, "Severe intraoperative albumin transfusion reaction and review of the literature," *Lab Medicine*, vol. 44, no. 4, pp. e129–e131, 2013.

[109] C. Hu, Y. Feng, P. Huang, and J. Jin, "Adverse reactions after the use of SonoVue contrast agent," *Medicine*, vol. 98, no. 44, 2019.

[110] S.-i. Umemura, K.-i. Kawabata, and K. Sasaki, "Enhancement of sonodynamic tissue damage production by second-harmonic superimposition: theoretical analysis of its mechanism," *IEEE Transactions on Ultrasonics, Ferroelectrics, and Frequency Control*, vol. 43, no. 6, pp. 1054–1062, 1996.

[111] K. Tanabe, M. Belohlavek, J. F. Greenleaf, and J. B. Seward, "Tissue harmonic imaging: experimental analysis of the mechanism of image improvement," *Japanese Circulation Journal*, vol. 64, pp. 202–206, 2000.

[112] S.-i. Umemura, K.-i. Kawabata, and K. Sasaki, "In vivo acceleration of ultrasonic tissue heating by microbubble agent," *IEEE Transactions on Ultrasonics, Ferroelectrics, and Frequency Control*, vol. 52, no. 10, pp. 1690–1698, 2005.

[113] C. S. Carlson, A. Deroubaix, C. Penny, and M. Postema, "On the attenuation of ultrasound by pure black tattoo ink," *SAIEE Africa Research Journal*, vol. 112, no. 1, pp. 24–31, 2021.

[114] C. S. Carlson, R. Matsumoto, K. Fushino, M. Shinzato, N. Kudo, and M. Postema, "Transient ink nucleation: the proof is in the pudding," in *Proceedings of the 41st Symposium on Ultrasonic Electronics*, no. 2E5–1, 2020.

[115] S. Kotopoulis, K. Johansen, O. Gilja, A. Poortinga, and M. Postema, "Acoustically active antibubbles," *Acta Physica Polonica A*, vol. 127, no. 1, pp. 99–102, 2015.

[116] D. Bradley and G. Roth, "Adaptive thresholding using the integral image," *Journal of Graphics Tools*, vol. 12, no. 2, pp. 13–21, 2007.

[117] P. Huang, "An integrated approach to ultrasound imaging in medicine and biology," *BIO Integration*, vol. 1, no. 3, pp. 105–109, 2020.

[118] F. Piscaglia, F. Stefanini, V. Cantisani, P. S. Sidhu, R. Barr, A. Berzigotti, M. C. Chammas, J. M. Correas, C. F. Dietrich, S. Feinstein, P. Huang, C. Jenssen, C. Jenssen, Y. Kono, M. Kudo, P. Liang, A. Lyshchik, C. Nolsoe, X. Xie, and F. Tovoli, "Benefits, open questions and challenges of the use of ultrasound in the COVID-19 pandemic era. The views of a panel of worldwide international experts," *Ultraschall in der Medizin*, vol. 41, pp. 228–236, 2020.

[119] Y. Yang, Q. Li, X. Guo, J. Tu, and D. Zhang, "Mechanisms underlying sonoporation: interaction between microbubbles and cells," *Ultrasonics Sonochemistry*, vol. 67, no. 105096, 2020.

[120] T. Zhang, B. Wu, O. U. Akakuru, C. Yao, S. Sun, L. Chen, W. Ren, A. Wu, and P. Huang, "Hsp90 inhibitor-loaded IR780 micelles for mitochondria-targeted mild-temperature photothermal therapy in xenograft models of human breast cancer," *Cancer Letters*, vol. 500, pp. 41–50, 2021.

[121] E. R. Bolookat, L. J. Rich, G. Paragh, O. R. Colegio, A. K. Singh, and M. Seshadri, "Photoacoustic imaging of tattoo inks: phantom and clinical evaluation," *Applied Sciences*, vol. 10, no. 1024, 2020.

[122] T. Matsuda, T. Iwasaki, K. Hirata, D. Tsugawa, Y. Sugita, S. Ishida, S. Kanaji, and Y. Kakeji, "Simple and reliable method for tumor localization during

totally laparoscopic gastrectomy: intraoperative laparoscopic ultrasonography combined with tattooing," *Gastric Cancer*, vol. 20, pp. 548–552, 2017.

[123] S. Hartmann, T. Kühn, J. de Boniface, A. Stachs, A. Winckelmann, J. Frisell, I. Wiklander-Bråkenhielm, J. Stubert, B. Gerber, and T. Reimer, "Carbon tattooing for targeted lymph node biopsy after primary systemic therapy in breast cancer: prospective multicentre TATTOO trial," *British Journal of Surgery*, vol. 108, no. 3, pp. 302–307, 2021.

[124] S. Kotopoulis, A. Delalande, M. Popa, V. Mamaeva, G. Dimcevski, O. H. Gilja, M. Postema, B. T. Gjertsen, and E. Mc Cormack, "Sonoporation-enhanced chemotherapy significantly reduces primary tumour burden in an orthotopic pancreatic cancer xenograft," *Molecular Imaging and Biology*, vol. 16, pp. 53–62, 2013.

[125] G. Dimcevski, S. Kotopoulis, T. Bjånes, D. Hoem, J. Schjøtt, B. T. Gjertsen, M. Biermann, A. Molven, H. Sorbye, E. Mc Cormack, M. Postema, and O. H. Gilja, "A human clinical trial using ultrasound and microbubbles to enhance gemcitabine treatment of inoperable pancreatic cancer," *Journal of Controlled Release*, vol. 243, pp. 172–181, 2016.

[126] G. ter Haar, "HIFU tissue ablation: concept and devices," *Advances in Experimental Medicine and Biology*, vol. 880, pp. 3–20, 2016.

[127] C. S. Carlson, R. Matsumoto, K. Fushino, M. Shinzato, N. Kudo, and M. Postema, "Nucleation threshold of carbon black ultrasound contrast agent," *Japanese Journal of Applied Physics*, vol. 60, no. SDDA06, 2021.

[128] L. W. Hofstetter, L. Fausett, A. Mueller, H. Odéen, A. Payne, D. A. Christensen, and D. L. Parker, "Development and characterization of a tissue mimicking psyllium husk gelatin phantom for ultrasound and magnetic resonance imaging," *International Journal of Hyperthermia*, vol. 37, no. 1, pp. 283–290, 2020.

[129] P.-H. Tsui, Y.-C. Shu, W.-S. Chen, H. L. Liu, I.-T. Hsiao, and Y.-T. Chien, "Ultrasound temperature estimation based on probability variation of backscatter data," *Medical Physics*, vol. 39, no. 5, pp. 2369–2385, 2012.

[130] M. L. Oelze and J. Mamou, "Review of quantitative ultrasound: envelope statistics and backscatter coefficient imaging and contributions to diagnostic ultrasound," *IEEE Transactions on Ultrasonics, Ferroelectrics, and Frequency Control*, vol. 63, no. 2, pp. 336–351, 2016.

[131] A. Han, Y. N. Zhang, A. S. Boehringer, M. P. Andre, J. W. Erdman, R. Loomba, C. B. Sirlin, and W. D. O'Brien, "Inter-platform reproducibility of ultrasonic

attenuation and backscatter coefficients in assessing NAFLD," *European Radiology*, vol. 29, pp. 4699–4708, 2019.

[132] M. Omura, H. Hasegawa, R. Nagaoka, K. Yoshida, and T. Yamaguchi, "Validation of differences in backscatter coefficients among four ultrasound scanners with different beamforming methods," *Journal of Medical Ultrasonics*, vol. 47, pp. 35–46, 2020.

[133] G. Iori, J. Du, J. Hackenbeck, V. Kilappa, and K. Raum, "Estimation of cortical bone microstructure from ultrasound backscatter," *IEEE Transactions on Ultrasonics, Ferroelectrics, and Frequency Control*, vol. 68, no. 4, pp. 1081–1095, 2021.

[134] H. Lopez and K. M. Harris, "Ultrasound interactions with free silicone in a tissue-mimicking phantom," *Journal of Ultrasound in Medicine*, vol. 17, pp. 163–170, 1998.

[135] L. Ressel, "The biopsy "undead"," *Veterinary Pathology*, vol. 55, no. 6, pp. 916–917, 2018.

[136] R. Kuc and M. Schwartz, "Estimating the acoustic attenuation coefficient slope for liver from reflected ultrasound signals," *IEEE Transactions on Sonics and Ultrasonics*, vol. SU-26, no. 5, pp. 353–362, 1979.

[137] K. Hensel and G. Schmitz, "Method for the estimation and compensation of attenuating tissue layers by the acoustic observation of microbubbles for sonoporation therapy," in *Proceedings of the 2010 IEEE Ultrasonics Symposium*, 2010, pp. 1700–1703.

[138] O. Perlman and H. Azhari, "Ultrasonic computed tomography imaging of iron oxide nanoparticles," *Physics in Medicine and Biology*, vol. 62, pp. 825–842, 2017.

[139] N. Alves, A. Kim, J. Tan, G. Hwang, T. Javed, B. Neagu, and B. K. Courtney, "Cardiac tissue-mimicking ballistic gel phantom for ultrasound imaging in clinical and research applications," *Ultrasound in Medicine and Biology*, vol. 46, no. 8, pp. 2057–2069, 2020.

[140] P. Stanway, J. Nudds, and F. Broadhurst, "The depositional environment of the Ashfell Sandstone Formation (Arundian, Mississippian), Ash Fell Edge, Cumbria, NW England," in *Proceedings of the Yorkshire Geological Society*, vol. 60, 2015, pp. 145–152.

[141] J. Krautkrämer and H. Krautkrämer, *Werkstoffprüfung mit Ultraschall*, 5th ed. Springer, Berlin, 1986.

[142] A. Nowicki, "Safety of ultrasonic examinations; thermal and mechanical indices," *Medical Ultrasonography*, vol. 22, no. 2, pp. 203–210, 2020.

[143] S. Yongchen, D. Yanwu, T. Jie, and T. Zhensheng, "Ultrasonic propagation parameters in human tissues," in *Proceedings of the 1986 IEEE Ultrasonics Symposium*, 1986, pp. 905–908.

[144] D. Folds, "Speed of sound and transmission loss in silicone rubbers at ultrasonic frequencies," *Journal of the Acoustical Society of America*, vol. 56, no. 4, pp. 1295–1296, 1974.

[145] P. A. Lewin and H. Busk, "In vivo ultrasonic measurements of tissue properties," in *Proceedings of the 1982 IEEE Ultrasonics Symposium*, 1982, pp. 709–712.

[146] P. Gehrke, R. Smeets, M. Gosau, R. E. Friedrich, E. Madani, D. Duddeck, C. Fischer, F. Tebbel, R. Sader, and P. Hartjen, "The influence of an ultrasonic cleaning protocol for CAD/CAM abutment surfaces on cell viability and inflammatory response *in vitro*," *In Vivo*, vol. 33, no. 3, pp. 689–698, 2019.

[147] S. Zahn, Y. Schneider, and H. Rohm, "Ultrasonic cutting of foods: effects of excitation magnitude and cutting velocity on the reduction of cutting work," *Innovative Food Science and Emerging Technologies*, vol. 7, no. 4, pp. 288–293, 2006.

[148] G. Arnold, L. Leiteritz, S. Zahn, and H. Rohm, "Ultrasonic cutting of cheese: composition affects cutting work reduction and energy demand," *International Dairy Journal*, vol. 19, no. 5, pp. 314–320, 2009.

[149] L. Liu, W. Jia, D. Xu, and R. Li, "Applications of ultrasonic cutting in food processing," *Journal of Food Processing and Preservation*, vol. 39, pp. 1762–1769, 2015.

[150] G. Sinn, B. Zettl, H. Mayer, and S. Stanzl-Tschegg, "Ultrasonic-assisted cutting of wood," *Journal of Materials Processing Technology*, vol. 170, no. 1–2, pp. 42–49, 2005.

[151] D. Schneider, K. Goppold, P. W. Kaemmerer, G. Schoen, M. Woehlke, and R. Bschorer, "Use of ultrasonic scalpel and monopolar electrocautery for skin incisions in neck dissection: a prospective randomized trial," *Oral and Maxillofacial Surgery*, vol. 22, pp. 169–175, 2018.

[152] A. R. Khan, M. Hafeez, and A. U. Arif, "Ultrasonic cutting in multinodar thyroid swellings," *Journal of Medical Sciences*, vol. 27, no. 1, pp. 7–10, 2019.

[153] A. Cardoni, A. MacBeath, and M. Lucas, "Methods for reducing cutting temperature in ultrasonic cutting of bone," *Ultrasonics*, vol. 44, no. Suppl. 22, pp. e37–e42, 2006.

[154] G. L. Camanho, A. C. Bitar, A. J. Hernandez, and R. Olivi, "Medial patellofemoral ligament reconstruction: a novel technique using the patellar ligament," *Arthroscopy*, vol. 23, no. 1, pp. 108.e1–108.e4, 2007.

[155] A. Mattei, M. Fambrini, G. Bargelli, A. Minervini, A. Valeri, A. Pieralli, K. L. Andersson, M. Marchionni, and G. Scarselli, "Use of a No. 11 blade scalpel and reusable blunt trocar to establish pneumoperitoneum: description of a safe and inexpensive technique," *Journal of Minimally Invasive Gynecology*, vol. 17, no. 6, pp. 760–765, 2010.

Appendix A

Supplementary Material

This appendix captures supplementary material for several chapters that was not included in the original publications.

A.1 Transient ink nucleation

Due to the page limits of the Symposium on Ultrasonic Electronics, 3 representative frames of one of the high-speed videos were included in the proceeding. To further illustrate the transient nucleation of black tattoo ink, Figure A.1 to Figure A.4 have been included. These figures show the full progression of nucleation during a 20 cycle, 1.0-MHz, 400 kPa ultrasound pulse under 20× magnification. The video was captured at 10 million frames per second.

There were several challenges that were experienced when capturing these dynamic phenomena. First, the observations made were a 2D representation of a 3D environment. This resulted in the challenge of finding the focal point, and of course the particles staying in the focal plane when exposed to sonication. Provided the particles did anything at all. It was not known which particles would undergo nucleation or when. There was a limitation on the resolution of the images. All too often in this research the particles corresponded with a single pixel. For particles of this small size, any compression as a result of the ultrasound field was not visible. Although the camera allowed for 10 frames to be captured per cycle, there could still be higher frequency dynamics that have not been observed in this study.

A.2 Acoustic analysis of inked tissues

The focus of the paper in BIO Integration was on physical tissues, and tissue-mimicking materials. As such, results that did not include tissue-like materials were excluded from the paper. One such result utilised a phantom with a cuboid well filled with distilled water, shown in Figure A.5.

Figure A.6 shows a representative proof-of-principle scan of distilled water adjacent to phantom material. The perceived angles of the highlighted regions were observed to lie between 14° and 15°. The theoretical perceived angle should lie between 14° and 16°. This is another confirmation that the theoretical model corresponds with what happens in reality.

Beyond this additional result, there were other tissue-mimicking phantoms produced for the experiments. One such additional phantom is shown in Figure A.7.

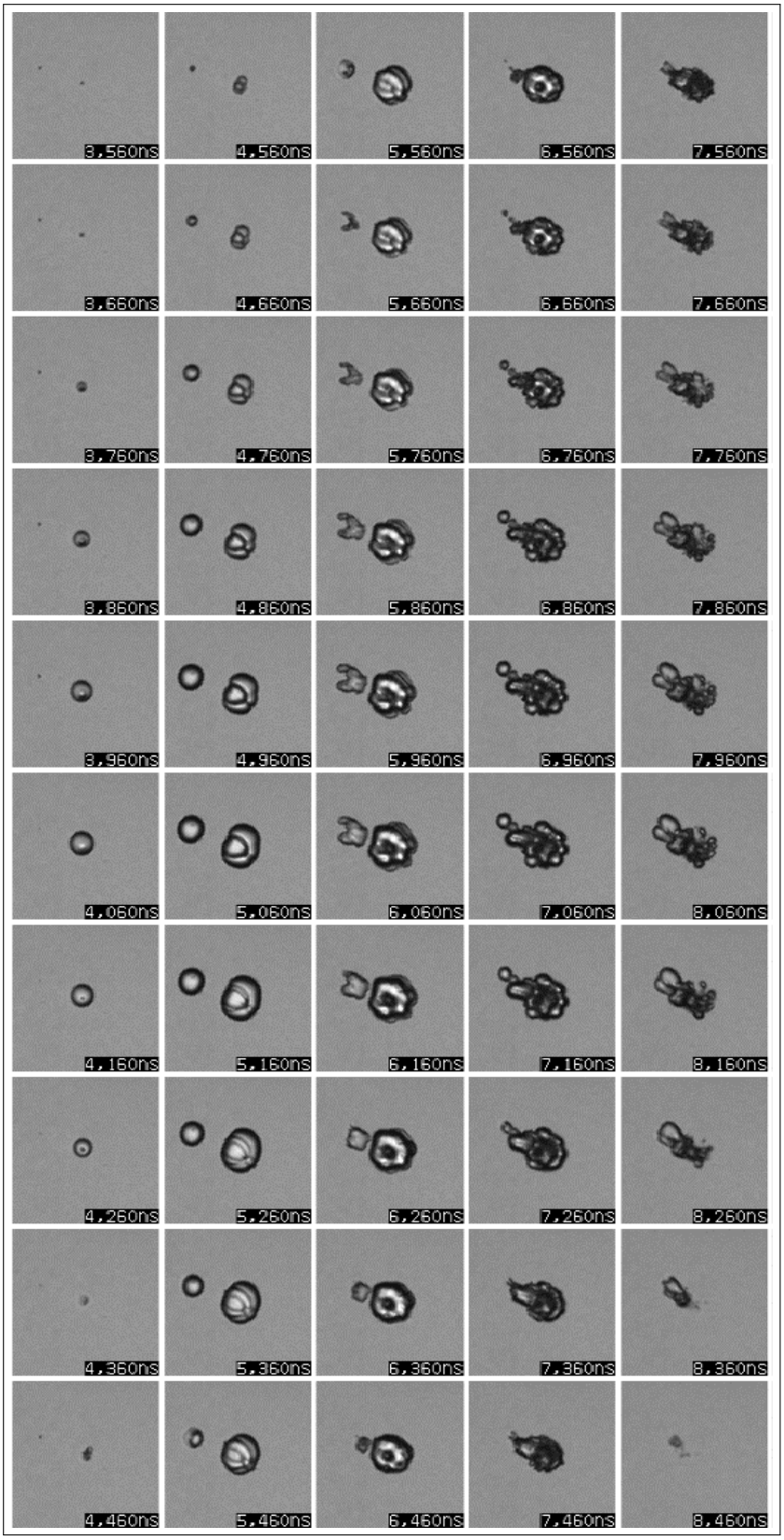


Figure A.1: Zuper Black ink particles during cycles 1 – 5 of sonication (left to right), where each cycle comprises 10 frames (top to bottom). Each frame corresponds to a $36 \times 36\,(\mu\text{m})^2$ area. Time stamps, in nanoseconds, are in the lower right corners.

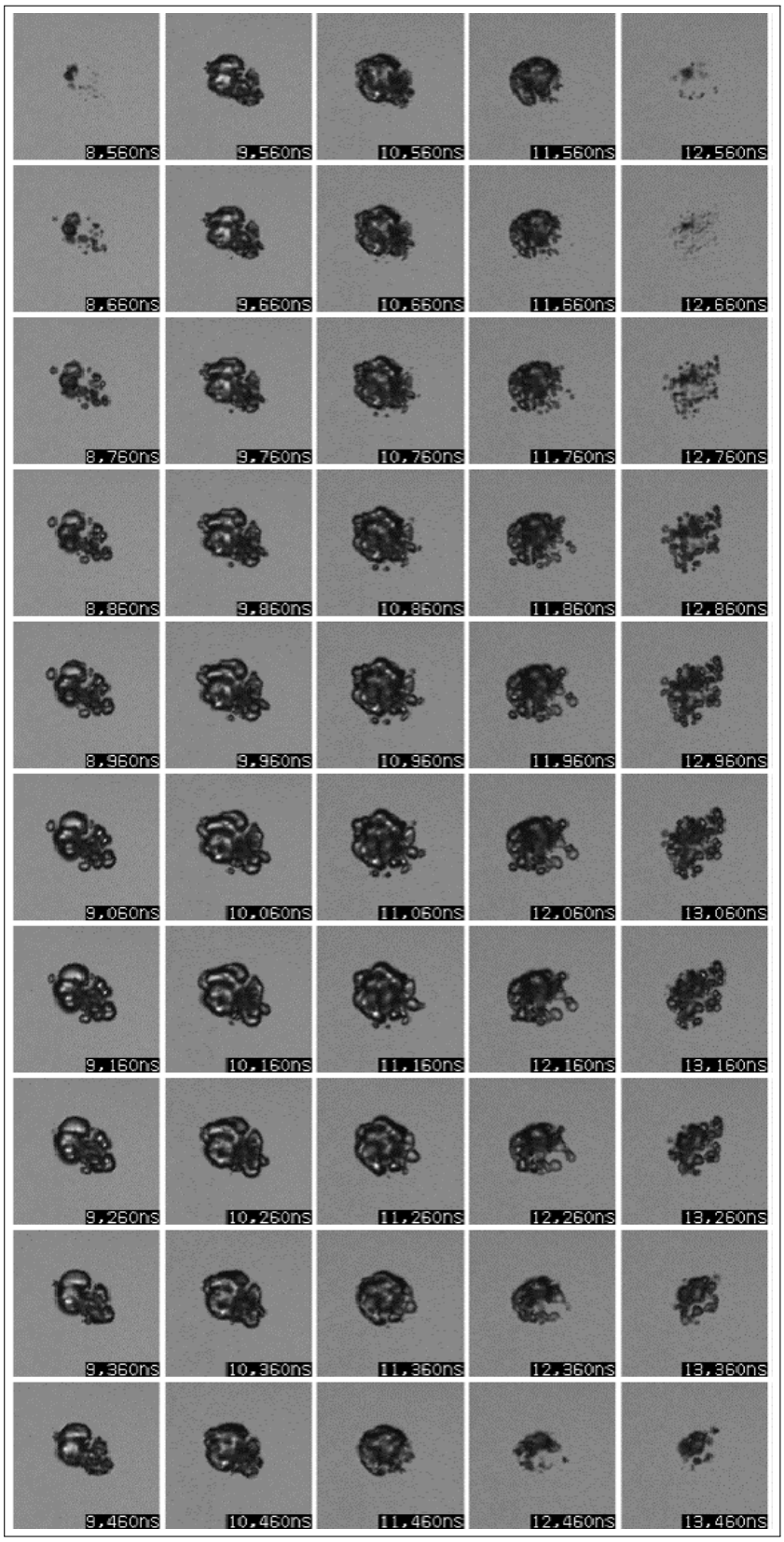


Figure A.2: Zuper Black ink particles during cycles 6 – 10 of sonication (left to right), where each cycle comprises 10 frames (top to bottom). Each frame corresponds to a $36 \times 36\,(\mu\text{m})^2$ area. Time stamps, in nanoseconds, are in the lower right corners.

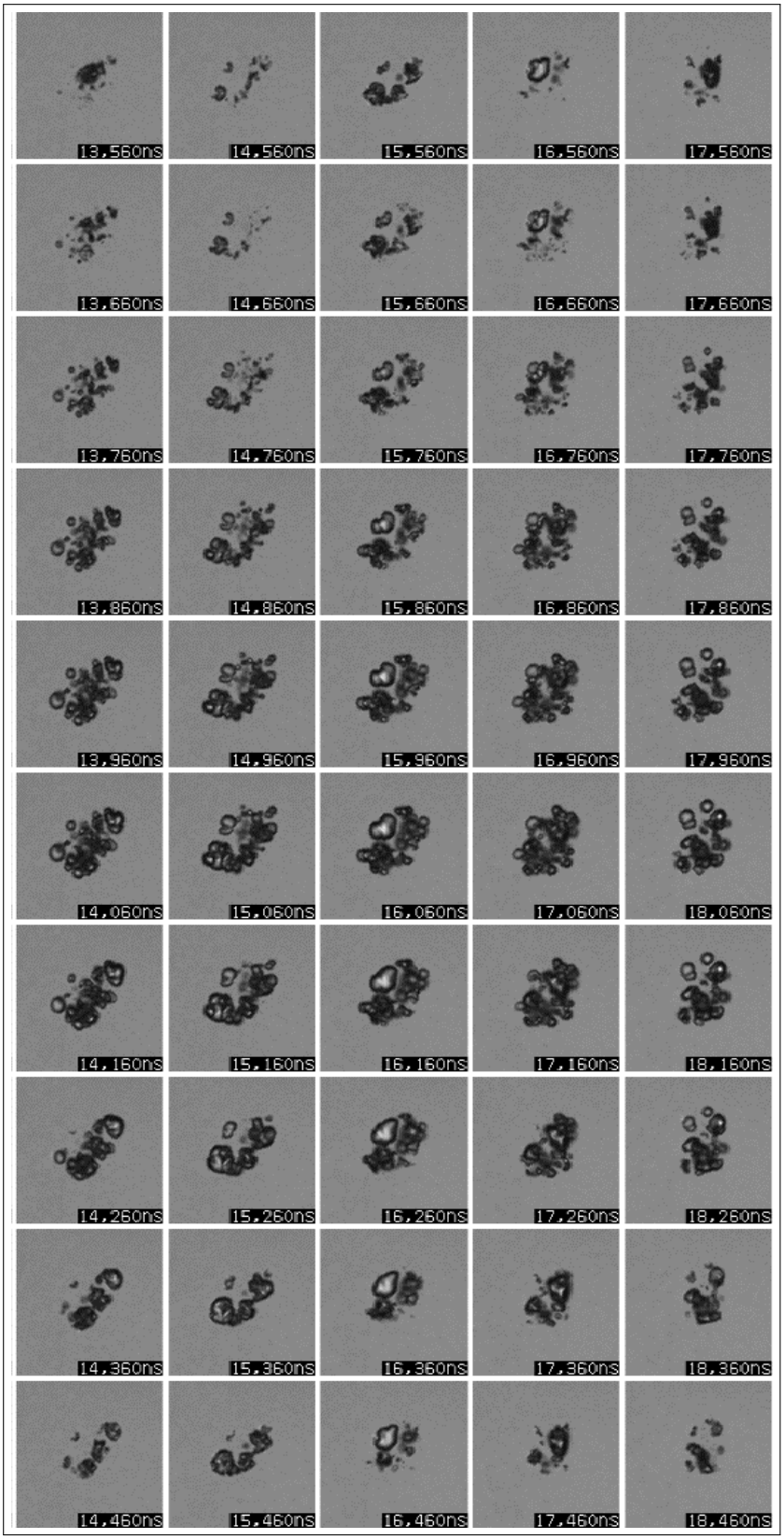


Figure A.3: Zuper Black ink particles during cycles 11 – 15 of sonication (left to right), where each cycle comprises 10 frames (top to bottom). Each frame corresponds to a $36 \times 36\,(\mu\text{m})^2$ area. Time stamps, in nanoseconds, are in the lower right corners.

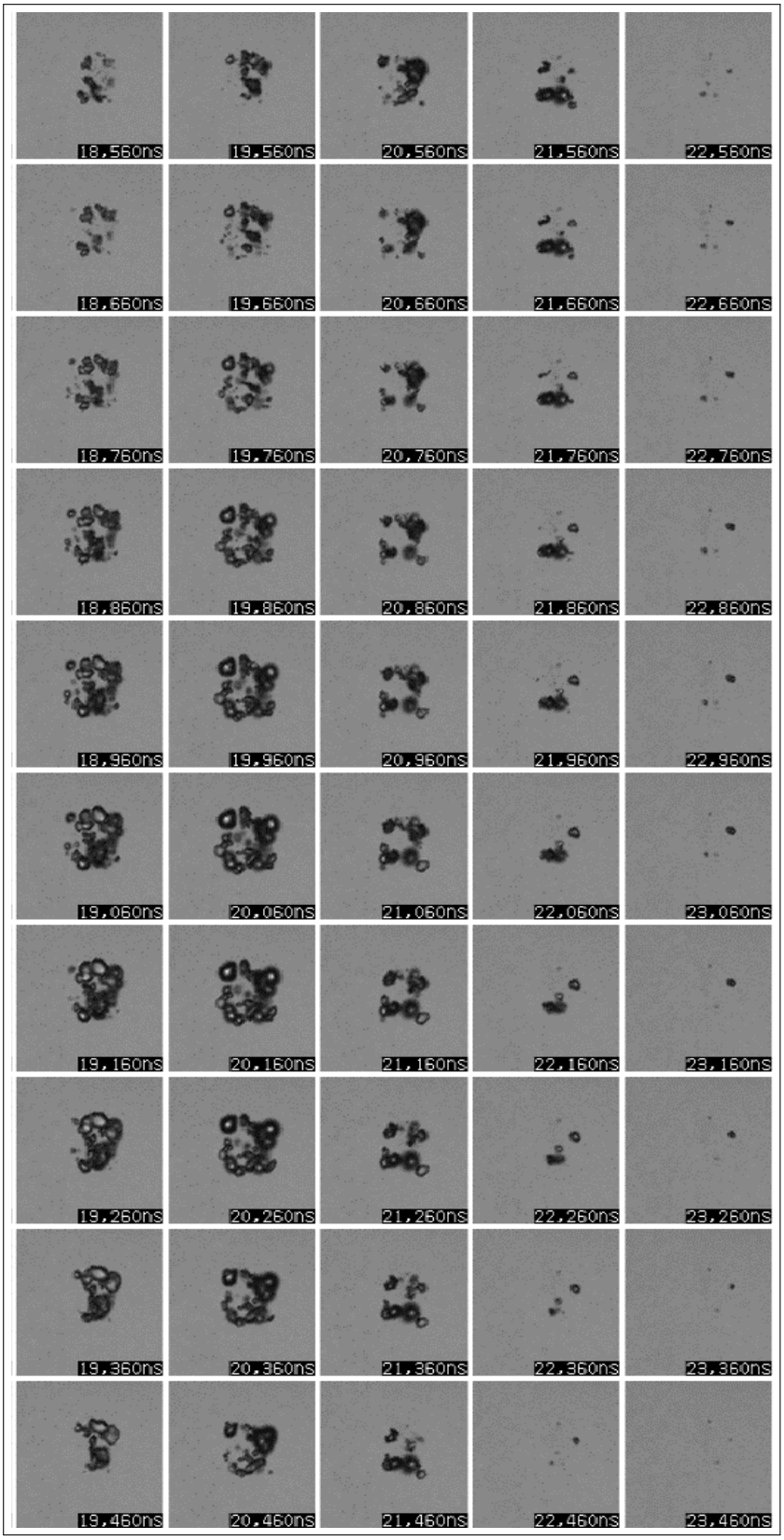


Figure A.4: Zuper Black ink particles during cycles 16 – 20 of sonication (left to right), where each cycle comprises 10 frames (top to bottom). Each frame corresponds to a $36 \times 36\,(\mu\text{m})^2$ area. Time stamps, in nanoseconds, are in the lower right corners.



Figure A.5: Experimental setup of the probe sonicating a tissue-mimicking phantom with a cuboid well filled with distilled water. A St Helena £1 coin has been added for scale and three-dimensional perspective.

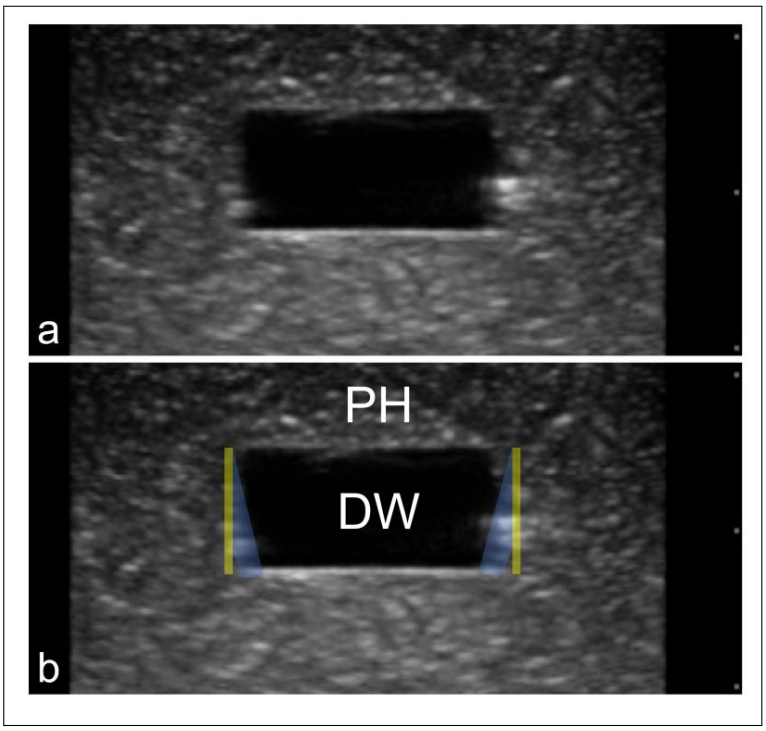


Figure A.6: Unmarked (a) and marked (b) brightness-mode scan of a cuboid well filled with distilled water (DW) surrounded by phantom material (PH). The vertical separations between phantom and distilled water are indicated by yellow lines and zones of increased scattering amplitudes by opaque blue lines.



Figure A.7: Additional experimental setup of the probe sonicating a tissue-mimicking phantom with a cylindrical well filled with distilled water. A St Helena £1 coin has been added for scale and three-dimensional perspective.

About the Author



Craig S. Carlson was born in Johannesburg, South Africa in 1987. He received the B.Sc. degree in Electrical Engineering from the University of the Witwatersrand, Johannesburg, South Africa, in 2009, the M.Sc. degree in Engineering from the University of the Witwatersrand, Johannesburg, in 2012, and the M.B.A. degree from the University of Pretoria, South Africa, in 2018. He is an Associate Lecturer in Biomedical Engineering at the University of the Witwatersrand, Johannesburg. His research interests include other-than-diagnostic uses of medical ultrasound; sharp sonic cutting; tattoo modification; and tattoo removal.

List of publications

Dissertations and theses

C. S. Carlson, *The relationship between executive pay and company financial performance in South African state-owned entities.* Dissertation. Gordon Institute of Business Science, University of Pretoria. 2017.

C. S. Carlson, *Fuzzy logic load forecasting with genetic algorithm parameter adjustment.* Dissertation. University of the Witwatersrand, Johannesburg. 2012.

Conferences

C. S. Carlson, R. Matsumoto, K. Fushino, M. Shinzato, N. Kudo, and M. Postema, "Transient ink nucleation: the proof is in the pudding," in *Proceedings of the 41st Symposium on Ultrasonic Electronics*, no. 2E5–1, 2020.

N. Kudo, R. Uzbekov, R. Matsumoto, R.-i. Shimizu, C. S. Carlson, N. Anderton, A. Deroubaix, C. Penny, A. T. Poortinga, D. M. Rubin, A. Bouakaz, and M. Postema, "Oscillating endoskeletal antibubbles," in *Proceedings of the 40th Symposium on Ultrasonic Electronics*, no. 2E3–1, 2019.

C. S. Carlson, W. A. Cronjé, and M. A. van Wyk, "A short-term load forecasting tool for energy management in smart grids," in *Proceedings of the 2011 CIGRÉ International Symposium: The Electric Power System of the Future*, 2011.

C. S. Carlson, W. A. Cronjé, and M. A. van Wyk, "Utilising load forecasting for energy management in a high voltage system," in *Proceedings of the 17th International Symposium on High Voltage Engineering*, 2011.

Journal articles

C. S. Carlson, and M. Postema, "Deep impact of superficial skin inking: acoustic analysis of underlying tissue," *BIO Integration*, vol. 2, 2021.

C. S. Carlson, R. Matsumoto, K. Fushino, M. Shinzato, N. Kudo, and M. Postema, "Nucleation threshold of carbon black ultrasound contrast agent," *Japanese Journal of Applied Physics*, vol. 60, no. SDDA06, 2021.

D. M. Rubin, S. Achari, C. S. Carlson, R. F. R. Letts, A. Pantanowitz, M. Postema, X. L. Richards, and B. Wigdorowitz, "Facilitating understanding, modeling and simulation of infectious disease epidemics in the age of COVID-19," *Frontiers in Public Health*, vol. 9, no. 593417, 2021.

C. S. Carlson, A. Deroubaix, C. Penny, and M. Postema, "On the attenuation of ultrasound by pure black tattoo ink," *SAIEE Africa Research Journal*, vol. 112, no. 1, pp. 24–31, 2021.

N. Kudo, R. Uzbekov, R. Matsumoto, R.-i. Shimizu, C. S. Carlson, N. Anderton, A. Deroubaix, C. Penny, A. T. Poortinga, D. M. Rubin, A. Bouakaz, and M. Postema, "Asymmetric oscillations of endoskeletal antibubbles," *Japanese Journal of Applied Acoustics*, vol. 59, no. SKKE02, 2020.

C. S. Carlson, and M. H. R. Bussin. "Relationship between executive pay and company financial performance in South African state-owned entities," *SA Journal of Human Resource Management*, vol. 18, no. a1211, 2020.

C. S. Carlson, A. Pohl, D. G. Keir, and M. Postema, "Cutting edge technology: Sound sharpens the blade," *Applied Acoustics*, vol. 166, no. 107336, 2020.